

Cohesive and Spectroscopic properties of the Lanthanides within the Hubbard I Approximation

Licentiate Thesis in Physics by:
Inka L.M. Locht

Department of Physics and Astronomy, Uppsala University, Uppsala, Sweden
Institute for Molecules and Materials, Radboud University, Nijmegen, The
Netherlands

List of publications

This licentiate thesis is based on the following paper

I. The standard model of the rare-earths, analyzed from the Hubbard-I approximation

I. L. M. Locht, Y. O. Kvashnin, D. C. M. Rodrigues, I. Di Marco, M. Pereiro, A. Bergman, L. Bergqvist, M. I. Katsnelson, A. Delin, O. Eriksson, et. al.

In manuscript

Publications not included in this licentiate thesis

II. Ultrafast magnetization dynamics: Microscopic electronic configurations and ultrafast spectroscopy

I. L. M. Locht, I. Di Marco, S. Garnerone, A. Delin, and M. Battiato

Phys. Rev. B 92, 064403 – Published 3 August 2015

III. Analytic Continuation by Averaging Padé Approximants

J. Schött, I. L. M. Locht, E. Lundin, O. Eriksson, and I. Di Marco

In manuscript

IV. Stacking fault energetics of α - and γ -cerium investigated with ab initio calculations

A. Östlin, I. Di Marco, I. L. M. Locht, J. C. Lashley, and L. Vitos

Submitted to PRB

V. The Kohn-Sham equation of state for elemental solids: a solved problem

K. Lejaeghere, et. al.

Submitted to science

Contents

1	Introduction	7
2	Lanthanides	9
2.1	Outer electronic configuration	9
2.2	Bonding properties	10
2.3	Magnetism	12
2.3.1	Russell-Saunders coupling	12
2.3.2	Moments arising from the spin, orbital and total angular momenta	12
2.3.3	Hund's rules ground-state	13
2.3.4	Energy shift due to a magnetic field	15
2.3.5	Moments	15
2.4	Spectral properties	17
2.4.1	Spectroscopy	17
2.4.2	Experiment and theory	19
2.4.3	Multiplet structure	20
3	Methods	23
3.1	Density Functional Theory	24
3.1.1	Hohenberg-Kohn theorems	24
3.1.2	Kohn-Sham <i>ansatz</i>	25
3.1.3	Approximations to the energy functional	27
3.2	Hubbard I approximation	28
3.2.1	Effective Hubbard model	30
3.2.2	Effective Single impurity Anderson model	31
3.2.3	Computational scheme	33
3.2.4	Hubbard U and Hund's J	35
3.2.5	Double counting	37
4	RSPT-code and LMTOs	41
4.1	Symbols	42
4.2	LMTO Basis	42
4.2.1	Basis in the interstitial	43
4.2.2	Basis inside the muffin-tin sphere	43
4.3	Multiple linearization energies	44
4.4	Parameters	45

5	Computational details	47
5.1	Choice of basis for the rare earths	47
5.1.1	Notation	48
5.1.2	Basis with $4f$ in the core	48
5.1.3	Basis with $4f$ in the valence	50
5.2	Charge self-consistent versus single shot	55
6	Results	59
6.1	Cohesive properties	59
6.2	Magnetic Moments	64
6.3	Spectra	66
7	Outlook	69
A	Finding the multiplets in Nd	71
B	Direct Coulomb and Coulomb exchange	75
C	Basis notation look-up	77

Chapter 1

Introduction

In the introduction it is expected to write how important, technologically interesting and applicable your topic is. I have to confess, that I study the lanthanides (or rare earths) because it is fun! It is fun to learn new things about a group of materials. It is fun to relearn concepts I had forgotten. It is fun to establish the perfect basis. It is fun to try to get “*this-stupid-code*” converged and to investigate the results. It is fun to come up with creative solutions to simulations that are not willing to converge and to learn from it.

But why would you want to read this licentiate thesis? If you do not know much about the rare earths, I think it is super interesting to learn about them. When I started this project, I barely knew where in the Periodic Table I could find the lanthanides¹. But now I know that they are very interesting from a fundamental point. Their outermost incomplete shell (4*f*) consists of very localized electrons, that behave very close to atomic-like. This gives very interesting physical behavior. Both from technological point of view, such as strong localized magnetic moments, as well as from theoretical point of view. How to describe such localized states in a material that consists otherwise of very itinerant electrons? This is exactly the topic of this licentiate thesis.

The properties of rare earth metals or rare earth compounds are highly influenced by the characteristic behavior of the localized 4*f* shell. Many attempts have been made to describe these materials accurately. A practical and good theory to build the description upon is the standard model of the lanthanides. This model assumes a chemically inert 4*f* shell that is very much atomic-like. It has been able to successfully describe the properties of the rare earth elements and compounds.

Various attempts have been made to combine the standard model with *ab initio* based electronic structure theory. The usual density functional theory is quite inadequate for describing the lanthanides. For this reason more sophisticated theories have been tried, such as LDA+U, self-interaction correction (SIC), orbital polarization, and a treatment of the 4*f* shell as core-like. All these methods can describe certain properties very well, but not all. In this licentiate thesis we attempt to describe as many properties as we can within a single method: density functional theory plus dynamical mean-field theory within the Hubbard I approximation (HIA). This licentiate thesis is mainly focused on the cohesive properties (such as equilibrium volume and bulk modulus), the ground-state magnetic properties (spin and orbital moments) and the photoemission spectra (photoemission and inverse photoemission of the valence band). In the article

¹The upper of these two rows that are displayed below the main table.

on which this licentiate thesis is based (Paper I), we also report the Heisenberg exchange parameters, the magnon spectra and the ordering temperatures. The latter are discussed only in Paper I, as they are mainly contributed by other authors.

This licentiate thesis contains an introduction to the lanthanides in Ch. 2, discussing the electronic configuration, the bonding properties, magnetism and the spectral properties. Thereafter follows an introduction of methods to solve solid state problems in Ch. 3. This chapter contains a short description of density functional theory and the problems it has in describing the localized $4f$ electrons of the lanthanides. We also briefly explain the HIA, which is the method we propose to connect the standard model with *ab initio* electronic structure methods and that we use to describe the rare earth metals. In Ch. 4 we introduce the code that we used for our calculations, the way the basis is formed and the parameters that come along with it. In Ch. 5 we present the computational details, in particular in Ch. 5.1 we elaborate on how we found the optimal, light but sufficiently flexible, basis to describe the lanthanides. In Ch 6 we compare the results presented in Paper I to results obtained by other scientists using other methods.

Chapter 2

Lanthanides

This licentiate thesis focuses on the lanthanides, also called the rare earth (RE) elements¹. The properties of materials consisting of these elements are to a great extent determined by the behavior of the $4f$ shell. To describe these materials, the standard model of the lanthanides has turned out to be very successful. It assumes that the $4f$ shell behaves as atomic-like, with vanishingly small overlap between the $4f$ wave functions on neighboring sites. In the next sections we will summarize some properties of the rare earths. Why this standard model has been so successful can be understood in the light of these properties. The more or less constant volume across the series, for example, points to almost chemically inert $4f$ electrons, which is perfectly compatible with the standard model. The magnetic moments turn out to be very close to what is expected from Hund's rules, which are devised for atoms. Also the $4f$ photoemission spectra are very close to atomic-like spectra. This chapter is organized as follows, in Sec. 2.1 we will describe the outer electronic configuration of the rare earths in the atomic and in the solid phase. In Sec. 2.2 we will summarize the bonding properties of the rare earths, including the characteristic lanthanide contraction. In Sec. 2.3 we will shortly elaborate on the magnetism in the rare earths, the expected moments from Hund's rules ground-state and the Russell-Saunders coupling scheme. Finally in Sec. 2.4 we will arrive at the direct and inverse photoemission spectra of the rare earths. Photoemission spectroscopy and inverse photoemission spectroscopy will be explained briefly as well as how to interpret the spectra in terms of multiplet features.

2.1 Outer electronic configuration

The lanthanides denote the elements from lanthanum (atomic number $Z = 57$) till lutetium ($Z = 71$). Sometimes Ba ($Z = 56$) is included for reasons that will become clear later. Across the series, the $4f$ shell is filled. The electronic configuration of an isolated rare earth atom usually is $[\text{Xe}]6s^2d^04f^n$, where n depends on the atomic number. There are a few exceptions to this, namely Lanthanum, Gadolinium and Lutetium, who have one $5d$ electron and therefore one $4f$ electron less than expected [2]. For isolated atoms, the energy levels are truly discrete and filling the $4f$ shell is straight forward. However, when the atoms form a crystal, the orbitals start to hybridize with other orbitals, and the energy levels broaden into bands. For the crystalline phase of the lanthanides,

¹Actually, the rare earths also include Sc and Y, which are not part of the lanthanides, but I will use the term rare earths synonymously to lanthanides.

one cannot any longer speak of the $6s$ energy level, instead the $6s$, $6p$ and $5d$ orbitals hybridize and the energy levels broaden to form the $[6s6p5d]$ -band. The $4f$ energy levels and this $[spd]$ -band overlap and the consequence is that, for most lanthanides, one of the $4f$ electrons of the isolated atom, gets promoted to the $[spd]$ -band in the crystalline phase. The reason for this is that the Coulomb energy to pay for adding an f electron is much higher than the kinetic energy to pay for adding a delocalized $[spd]$ electron. The outer electronic configuration of the lanthanides in the crystalline phase is therefore approximately $[6s6p5d]^3 f^{n-1}$, where $n - 1$ denotes that there is one $4f$ electron less than in the bare atom. Also to these electronic configurations there are a few exceptions. Barium, Europium and Ytterbium have only 2 instead of 3 electrons in the $[spd]$ -band, since in that way they have an f -shell which is empty, half-filled or full. The reason for this is that the Coulomb energy to pay when adding an f electron to obtain a half-filled or full shell is very small. These exceptions are called divalent elements, since they only have 2 electrons in the $[spd]$ band. The other elements are called, as expected, trivalent. In the following table the outer electronic configuration of the rare earths is given for the atomic and the crystalline phases.

	La	Ce	Pr	Nd	Pm
Atomic	$5d^1 6s^2$	$4f^2 5d^0 6s^2$	$4f^3 5d^0 6s^2$	$4f^4 5d^0 6s^2$	$4f^5 5d^0 6s^2$
Solid	$[spd]^3$	$4f^1 [spd]^3$	$4f^2 [spd]^3$	$4f^3 [spd]^3$	$4f^4 [spd]^3$
	Sm	Eu	Gd	Tb	Dy
Atomic	$4f^6 5d^0 6s^2$	$4f^7 5d^0 6s^2$	$4f^7 5d^1 6s^2$	$4f^9 5d^0 6s^2$	$4f^{10} 5d^0 6s^2$
Solid	$4f^5 [spd]^3$	$4f^7 [spd]^2$	$4f^7 [spd]^3$	$4f^8 [spd]^3$	$4f^9 [spd]^3$
	Ho	Er	Tm	Yb	Lu
Atomic	$4f^{11} 5d^0 6s^2$	$4f^{12} 5d^0 6s^2$	$4f^{13} 5d^0 6s^2$	$4f^{14} 5d^0 6s^2$	$4f^{14} 5d^1 6s^2$
Solid	$4f^{10} [spd]^3$	$4f^{11} [spd]^3$	$4f^{12} [spd]^3$	$4f^{14} [spd]^2$	$4f^{14} [spd]^3$

2.2 Bonding properties

In Fig. 2.1 the experimental average atomic volume of a crystal consisting of one element from the lanthanide series is plotted. We included Ba as being divalent like Eu and Yb. These elements have an empty, half filled and filled $4f$ shell respectively. If one compares the volumes for the different elements, there are three important things to notice:

- The three exceptions, i.e. the divalent materials Ba, Eu and Yb, have a significant larger volume than the ordinary trivalent materials.
- For the trivalent materials, the volume is approximately constant, and is not parabolic-like as in the transition metal series.
- The volume decreases slightly across the series, both for divalent and trivalent materials.

These three observations can intuitively be related to the behavior and the properties of the $4f$ and $[spd]$ electrons. If we focus for now on the trivalent materials, the $4f$ shell is filled across the series, but the volume stays approximately constant. This implies that the $4f$ electrons do not, or barely, contribute to the bonding between neighboring atoms. It does not really matter whether there is one $4f$ electron more or less. But what

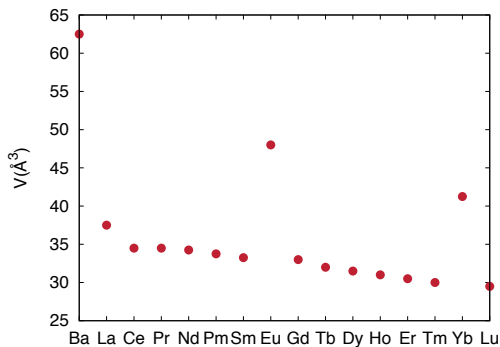


Figure 2.1: Average atomic volume for the elemental crystals consisting of elements on x -axis. The data are taken from Ref. [15]. The lanthanide contraction can clearly be seen.

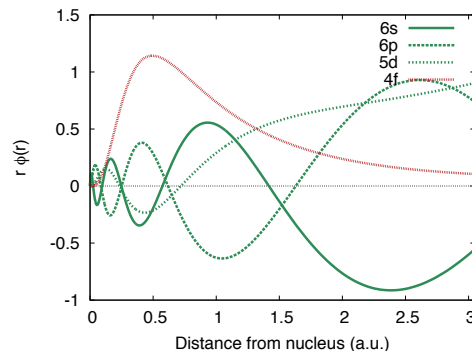


Figure 2.2: Radial part of the wave function inside the muffin tin sphere. Typical difference in localization of the $4f$ (red) and the $[spd]$ orbitals (green) in the REs.

matters, is how many $[spd]$ electrons there are. The divalent materials, which only have $[spd]^2$, have a much larger volume, which indicates that the bonding between atoms is much weaker than for the trivalent materials, where one more $[spd]$ electron is present. In summary, in the lanthanides, the $[spd]$ electrons constitute the bonds. This is also reflected in the localized nature of the $4f$ orbitals, which are close to the core, while the delocalized $[spd]$ hybridized orbitals extend far from the core. This difference in localization is illustrated in Fig. 2.2, where we plot the radial part of the wave function inside the muffin tin sphere. The localization of the $4f$'s is especially strong in the heavy rare earths and becomes a bit less pronounced for the light rare earths. Therefore some $4f$ -hybridization might be expected for the very early rare earths.

If one compares a rare earth element to its neighbor to the left in the Periodic Table, one proton and one $4f$ electron are added. The $[spd]$ electrons experience the increasing core charge only partially, since the latter is very well screened by the $4f$ electrons. However, this screening is not complete. Progressing through the series the $[spd]$ electrons experience slightly more attraction from the increasing core charge, the orbitals contract and therefore the volume decreases. This incomplete screening explains the slight decrease in volume across the series. This volume decrease is called lanthanide contraction.

As illustrated by the behavior of the volume across the series, the f electrons do barely contribute to the bonding. This, and also the behavior of the magnetic properties of the rare earths, lead to the assumption of a chemical inert f shell. This assumption made calculations involving lanthanides much easier than a proper solution of the many-body problem. Assuming a chemically inert $4f$ -shell is often denoted as the standard model of the lanthanides.

2.3 Magnetism

In this section we will briefly describe magnetism in rare earths. For the present we keep it simple and leave crystal field effects out of the picture. Although, in this section, we will present a basic picture without crystal field effects, for some of the rare earths, like Pr, they are extremely important. We will then explain about the Russell-Saunders coupling scheme, and how the magnetic moments originate from spin, orbital and total angular momentum. We will present the Hund's rule ground-state for all rare earths. This ground-state is $(2J + 1)$ -fold degenerate without external magnetic fields. How a field lifts this degeneracy and what moments are expected for small and big fields will be explained at the end of this section. To study the magnetic properties of the rare earths, *Solid State Physics* by Ashcroft and Mermin [2], *Rare earth Magnetism* by Jensen and Mackintosh [23] and the Master's Thesis of N.E. Koch [24] were very useful. The following sections on the magnetic properties of the rare earths are based on these three works.

2.3.1 Russell-Saunders coupling

The moments of the rare earths are well described in the Russell-Saunders (*LS*-) coupling scheme. This scheme is based on the assumption that spin-spin coupling is stronger than orbit-orbit coupling which is stronger than spin-orbit coupling. These couplings are described by Hund's rules, which are explained later on in the text. The exchange interaction couples the spins \mathbf{s}^i of the individual electrons to a total spin angular momentum \mathbf{S} . The total spin quantum number is $S = \sum_i m_s^i$ where m_s^i is the spin projection quantum number of the electron i and specifies the projection of \mathbf{s}^i along a specific axis. The Coulomb interaction similarly couples the orbital angular momenta \mathbf{l}^i of the individual electrons to a total orbital angular momentum \mathbf{L} . The total orbital angular momentum quantum number is $L = \sum_i m_l^i$, where the magnetic quantum number m_l^i specifies the projection of the orbital angular momentum of the electron i along a specific axis. For the REs the electrons order according to Hund's rules, which will be explained later in this section.

Finally, the total angular momentum quantum number is given by $J = |L \pm S|$. Whether S is added to or subtracted from L depends on whether the shell more or less than half filled respectively. This is because for shells that are less than half filled, the energy is smallest for the state where $S_z = S$ and $L_z = -L$ have opposite sign. For shells that are more than half filled instead, the energy is smallest when $S_z = S$ and $L_z = L$ have the same sign. Here S_z and L_z are the projections of the total spin and orbital angular momentum on the specified axis. From now on we will indicate this axis as the $\hat{\mathbf{z}}$ -axis for sake of simplicity.

2.3.2 Moments arising from the spin, orbital and total angular momenta

This section describes the moments associated to the spin, orbital and total angular momentum vectors \mathbf{S} , \mathbf{L} and \mathbf{J} for the entire atom, e.g. the contribution of all electrons. The moment originating from the total spin angular momentum \mathbf{S} is given by:

$$\boldsymbol{\mu}_S = -\frac{g_s \mu_B}{\hbar} \mathbf{S} \quad (2.1)$$

where the g_s -factor is the gyromagnetic factor of the electronic spin, which is close to 2, and μ_B is the Bohr magneton. The magnitude of this moment is $\mu_S = g_s \mu_B \sqrt{S(S+1)} \approx 2\mu_B \sqrt{S(S+1)}$, where we used that the eigenvalues of \mathbf{S}^2 are $\hbar^2 S(S+1)$. The magnitude of the total moment originating from the orbital angular momentum is:

$$\mu_L = \mu_B \sqrt{L(L+1)} \quad (2.2)$$

which is also directed opposite to \mathbf{L} . Note that the gyromagnetic factor for the orbital moment is $g_l = 1$, which is why it does not appear in Eq. 2.2.

The moment due to the total angular momentum \mathbf{J} has a similar form

$$\mu_J = g \mu_B \sqrt{J(J+1)} \quad (2.3)$$

However, in this case g is the Landé factor and has a quite complicated form. This arises from the fact that the spin moment is 2 times $\mu_B \sqrt{S(S+1)}$, whereas the orbital moment does not have this factor 2. To take this into account, the Landé g factor is:

$$g = 1 + \frac{J(J+1) + S(S+1) - L(L+1)}{2J(J+1)} \quad (2.4)$$

In Fig. 2.3 an illustration is sketched for the vector addition of \mathbf{S} , \mathbf{L} to \mathbf{J} and for the vector addition of $\boldsymbol{\mu}_S$ and $\boldsymbol{\mu}_L$. Due to the Wigner-Eckart theorem, the average $\langle \boldsymbol{\mu}_L + \boldsymbol{\mu}_S \rangle$ should lie along $\hat{\mathbf{J}}$, which is the unit vector in the \mathbf{J} -direction. The projection of $\boldsymbol{\mu}_L + \boldsymbol{\mu}_S$ on the $\hat{\mathbf{J}}$ -axis has length

$$\mu_J = \frac{\mu_B}{\hbar} (\mathbf{L} \cdot \hat{\mathbf{J}} + 2\mathbf{S} \cdot \hat{\mathbf{J}}) \quad (2.5)$$

Using $\mathbf{L}^2 = (\mathbf{J} - \mathbf{S})^2$ to obtain an expression for $\mathbf{S} \cdot \hat{\mathbf{J}}$ and $\mathbf{S}^2 = (\mathbf{J} - \mathbf{L})^2$ to obtain an expression for $\mathbf{L} \cdot \hat{\mathbf{J}}$ leads to the g -factor in Eq. 2.4. The total angular momentum \mathbf{J} precesses around $\hat{\mathbf{z}}$.

Note that we assumed that the field is not too strong so that \mathbf{S} and \mathbf{L} are coupled to \mathbf{J} . For strong fields, \mathbf{S} and \mathbf{L} would precess independently around the direction of the external field.

2.3.3 Hund's rules ground-state

The magnetic ground-state for the lanthanides can be found by means of the Hund's rules. The Hund's rules state:

1. Maximize S , taking into account the Pauli principle.
2. Maximize L , while satisfying the first rule.
3. Minimize J for less than half filled shells ($J = |L - S|$) or maximize J for more than half filled shells ($J = |L + S|$), while satisfying the first two rules.

The Hund's rules ground-state and the corresponding magnetic moments are listed in Tab. 2.1 for all rare earths. After the elements name and their $4f$ configuration (in the solid state), the occupied m_l are indicated by \uparrow and \downarrow , depending on m_s . The resulting total S , L and J are listed as well as the total moment μ_J calculated from Eq. 2.3 and 2.4. The Hund's rule ground-state is, in zero field, $(2J + 1)$ fold degenerate. All states for $J_z = -J, -J + 1, \dots, J - 1, J$ have the same energy.

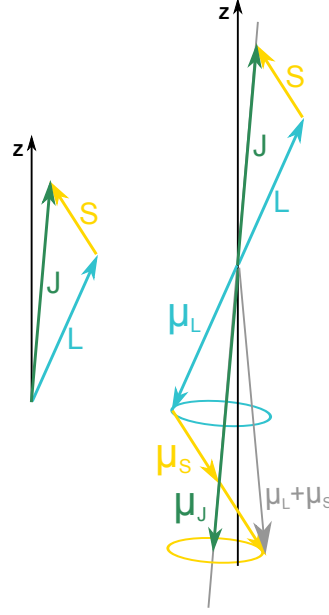


Figure 2.3: Vector representation of \mathbf{S} , \mathbf{L} and \mathbf{J} , and corresponding moments. The vector representation is however a bit misleading, since we can not simultaneously know all components of the vector. For that reason the ellipses are added, to denote that the vector is somewhere along this ellipse.

Table 2.1: Hund's rules ground-states and magnetic moments using Eq. 2.3 and 2.4.

		m_l										Moments
Element		-3	-2	-1	0	1	2	3	S	L	J	μ_J (μ_B)
Ba	f^0								0	0	0	0
La	f^0								0	0	0	0
Ce	f^1	\uparrow							$\frac{1}{2}$	3	$\frac{5}{2}$	2.535
Pr	f^2	\uparrow	\uparrow						1	5	4	3.578
Nd	f^3	\uparrow	\uparrow	\uparrow					$\frac{3}{2}$	6	$\frac{9}{2}$	3.618
Pm	f^4	\uparrow	\uparrow	\uparrow	\uparrow				2	6	4	2.683
Sm	f^5	\uparrow	\uparrow	\uparrow	\uparrow	\uparrow			$\frac{5}{2}$	5	$\frac{5}{2}$	0.845
Eu	f^7	\uparrow	\uparrow	\uparrow	\uparrow	\uparrow	\uparrow	\uparrow	$\frac{7}{2}$	0	$\frac{7}{2}$	7.937
Gd	f^7	\uparrow	\uparrow	\uparrow	\uparrow	\uparrow	\uparrow	\uparrow	$\frac{7}{2}$	0	$\frac{7}{2}$	7.937
Tb	f^8	$\uparrow\downarrow$	\uparrow	\uparrow	\uparrow	\uparrow	\uparrow	\uparrow	3	3	6	9.721
Dy	f^9	$\uparrow\downarrow$	$\uparrow\downarrow$	\uparrow	\uparrow	\uparrow	\uparrow	\uparrow	$\frac{5}{2}$	5	$\frac{15}{2}$	10.646
Ho	f^{10}	$\uparrow\downarrow$	$\uparrow\downarrow$	$\uparrow\downarrow$	\uparrow	\uparrow	\uparrow	\uparrow	2	6	8	10.607
Er	f^{11}	$\uparrow\downarrow$	$\uparrow\downarrow$	$\uparrow\downarrow$	$\uparrow\downarrow$	\uparrow	\uparrow	\uparrow	$\frac{3}{2}$	6	$\frac{15}{2}$	9.581
Tm	f^{12}	$\uparrow\downarrow$	$\uparrow\downarrow$	$\uparrow\downarrow$	$\uparrow\downarrow$	$\uparrow\downarrow$	\uparrow	\uparrow	1	5	6	7.561
Yb	f^{14}	$\uparrow\downarrow$	$\uparrow\downarrow$	$\uparrow\downarrow$	$\uparrow\downarrow$	$\uparrow\downarrow$	$\uparrow\downarrow$	$\uparrow\downarrow$	0	0	0	0
Lu	f^{14}	$\uparrow\downarrow$	$\uparrow\downarrow$	$\uparrow\downarrow$	$\uparrow\downarrow$	$\uparrow\downarrow$	$\uparrow\downarrow$	$\uparrow\downarrow$	0	0	0	0

2.3.4 Energy shift due to a magnetic field

In case a magnetic field is present, the Hamiltonian gets modified by two extra contributions. First the momentum operator gets replaced by $\mathbf{p}_i \rightarrow \mathbf{p}_i + \frac{e}{c}\mathbf{A}(\mathbf{r}_i)$, where \mathbf{A} is the vector potential, $-e$ the charge of an electron and c the speed of light. Second, a term accounting for the interaction between the spin and the field is added to the Hamiltonian. This term has the form of $g_s\mu_B\mathbf{H} \cdot \mathbf{S}$, where \mathbf{H} is the magnetic field in the $\hat{\mathbf{z}}$ -direction that the individual moments experience. These two contributions give field dependent terms in the Hamiltonian

$$\Delta\hat{H} = \mu_B(\mathbf{L} + g_s\mathbf{S}) \cdot \mathbf{H} + \frac{e^2}{8m_e c^2} H^2 \sum_i (x_i^2 + y_i^2) \quad (2.6)$$

The energy shifts that these terms produce are generally quite small and normal perturbation theory is adequate to calculate the splitting of the levels. The difference in energy induced by the field is given by

$$\begin{aligned} \Delta E_n = \mu_B \mathbf{H} \cdot \langle n | \mathbf{L} + g_s \mathbf{S} | n \rangle + \sum_{n' \neq n} \frac{|\langle n | \mu_B \mathbf{H} \cdot (\mathbf{L} + g_s \mathbf{S}) | n' \rangle|^2}{E_n - E_{n'}} \\ + \frac{e^2}{8m_e c^2} H^2 \langle n | \sum_i x_i^2 + y_i^2 | n \rangle + \dots \end{aligned} \quad (2.7)$$

where $|n\rangle$ is a state defined by quantum numbers J , L and S . In the case where $J = 0$, the first term vanishes. For filled shells, the first and second term vanish and the third term gives rise to Larmor diamagnetism. For not completely filled shells with $J = 0$ the second term (giving rise to Van Vleck paramagnetism) and the third term are in competition. However, for not completely filled shells, J is usually not equal to zero. We will now study the case where $\mathbf{J} \neq 0$ in a small field.

The ground-state, without field, is given by the Hund's rules and is $(2J + 1)$ fold degenerate ($J_z = -J, -J + 1, \dots, J - 1, +J$). A field lifts this degeneracy by energy differences calculated with Eq. 2.7. For small fields and $\mathbf{J} \neq 0$, the first term is usually dominant over the other two and therefore the last two terms are usually neglected. We consider a small field in the \hat{z} -direction to simplify the dot product. The problem at hand is now reduced to the $(2J + 1)$ -dimensional matrix $\langle JLSJ_z | \mathbf{L}_z + g_s \mathbf{S}_z | JLSJ'_z \rangle$, that can be simplified using the Wigner-Eckhart theorem

$$\langle JLSJ_z | \mathbf{L}_z + g_s \mathbf{S}_z | JLSJ'_z \rangle = g(JLS) J_z \delta_{J_z J'_z} \quad (2.8)$$

where $g(JLS) = g$ the same Landé g -factor as in Eq. 2.4. For clarity we will skip the arguments (JLS) of the g -factor.

2.3.5 Moments

In this section we continue assuming $\mathbf{J} \neq 0$ and calculate the total moment at a temperature T . We assume now that the separation between the zero field ground-state multiplet, given by the Hund's rules, and the first excited multiplet is much bigger than $k_B T$. In this case, only the $(2J + 1)$ states within this ground-state multiplet will contribute to the moment. The first term in Eq. 2.7 can now be interpreted as $-\boldsymbol{\mu} \cdot \mathbf{H}$, where $\boldsymbol{\mu} = -g\mu_B \mathbf{J}$. To obtain the magnetization of a collection of ions, the Helmholtz

free energy $F = -\frac{1}{\beta} \ln(\mathcal{Z})$, where \mathcal{Z} is the partition function, has to be calculated. Taking into account that the separation between the different J_z is not very big compared to $k_B T = 1/\beta$, one obtains that the partition function is

$$\mathcal{Z} = e^{-\beta F} = \sum_n e^{-\beta E_n(H)} = \sum_{J_z=-J}^J e^{-\beta g \mu_B H J_z} \quad (2.9)$$

$$= \frac{e^{\beta g \mu_B H(J+1/2)} - e^{-\beta g \mu_B H(J+1/2)}}{e^{\beta g \mu_B H/2} - e^{-\beta g \mu_B H/2}} \quad (2.10)$$

In the last line the geometric series was summed to simplify the expression. The magnetization M per volume V for N ions is given by

$$M = -\frac{N}{V} \frac{\delta F}{\delta H} = \frac{N}{V} g \mu_B J B_J(\beta g \mu_B J H) \quad (2.11)$$

where we have introduced the Brillouin function $B_J(x)$. This function saturates to 1 for large $x = \beta g \mu_B J H$, which implies that at large fields all moments align and contribute to the magnetization. We will first consider this limit and thereafter the limit for $x \rightarrow 0$, where $k_B T \gg g \mu_B H$.

Saturation moment $k_B T \ll g \mu_B H$

In case $k_B T \ll g \mu_B H$, only the lowest J_z of the zero field ground-state multiplet contributes. Each ion has its maximum value $J_z = J$ and the moment reaches its saturation value of

$$M = \frac{N}{V} g \mu_B J \quad (2.12)$$

A schematic representation of the saturated moment is given in Fig. 2.4 (left). Since we can not know all three components of $\boldsymbol{\mu}_J$ simultaneously, the saturation moment is the projection (black arrow) of $\boldsymbol{\mu}_J$ (green arrow) on the $\hat{\mathbf{z}}$ -axis.

Curie's law $k_B T \gg g \mu_B H$

When the splitting between the different energy levels in the zero-field ground-state multiplet is smaller than $k_B T$, many levels contribute to the magnetization. The Brillouin function can be expanded around small x , which leads to the magnetic susceptibility

$$\chi = \frac{\delta M}{\delta H} = \frac{N}{V} \frac{(g \mu_B)^2}{3} \beta J(J+1) \quad (2.13)$$

This is often rewritten in the form

$$\chi = \frac{\delta M}{\delta H} = \frac{1}{3} \frac{N}{V} \beta \mu_B^2 p^2 \quad (2.14)$$

where p is the effective Bohr magneton number $p = g \sqrt{J(J+1)}$. This relation between the susceptibility and the temperature is called Curie's law. A schematic representation of the paramagnetic moment ($p \mu_B$ in Eq. 2.14 or μ_J in Eq. 2.3) that is deduced from Curie's law is given in Fig. 2.4(right).

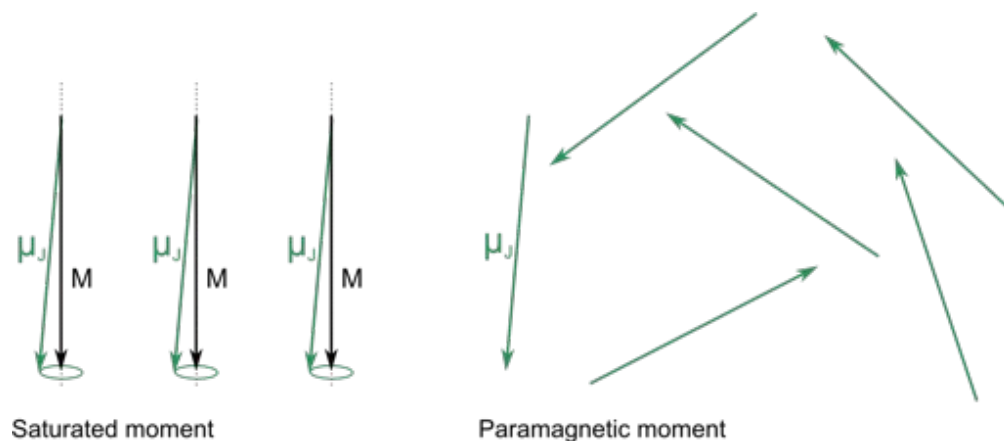


Figure 2.4: Schematic representation of the saturated moment and the paramagnetic moment. For the saturated moment the direction of the moment is fixed along an axis, therefore the maximum value it can take is the maximal projection of the vector μ_J , which is fluctuating around the \hat{z} -axis, on that axis as in Eq. 2.12 (black arrow in left plot). For the paramagnetic moment the direction of the individual moments is not specified, therefore it can take the full moment μ_J associated to the vector \mathbf{J} as in Eq. 2.3 (green arrow in right plot). However in particular in this case the vector representation is misleading, since we can not simultaneously know all components of the vector.

2.4 Spectral properties

The spectral function is a quantity that can be obtained from Dynamical Mean-Field Theory (DMFT) and can be compared to experiment. In this licentiate thesis, we are interested in the $4f$ multiplet structure of the lanthanides. This multiplet structure is probed in two different ways. X-ray Photoelectron Spectroscopy (XPS) is used to probe the occupied states and Bremsstrahlung Isochromat Spectroscopy (BIS) is used to probe the unoccupied states. The theory of high-energy spectroscopy, focussed on the lanthanides, is nicely introduced in chapter 62 of *Handbook on the physics and chemistry of the rare earths* by Gschneidner and Eyring [16]. The following sections will be based on this book.

2.4.1 Spectroscopy

The methods used in electron spectroscopy can be divided into two main categories: core level spectroscopy and outer level spectroscopy. In this section we will focus on the outer level spectroscopy, which can again be divided into two different techniques: photoemission (PE) and inverse photoemission (IPE) techniques.

In a photoemission experiment, the sample is irradiated with a monochromatic photon beam of known energy. This causes an emission of electrons from the sample, see Fig. 2.5(a). The energy and intensity distribution of these emitted electrons is measured. From this and the energy of the photon beam, the energy difference between the initial and final states of the system is measured. The final state has one electron less than the initial state. The probability of the transitions is mainly determined by the available electrons just below the Fermi level. Therefore one probes the occupied part of the spectrum with this technique. Traditionally, different photoemission experiments

are characterized by the energy of the photon beam used, for example ultraviolet photoemission spectroscopy (UPS), where the photon energy is $h\nu < 100\text{eV}$ or X-ray photoemission spectroscopy (XPS), where the photon energy is about $1200\text{ eV} \lesssim h\nu \lesssim 1500\text{ eV}$ [16]. Nowadays much higher photon energies can be used.

In an inverse photoemission experiment, the sample is irradiated with a monoenergetic *electron* beam. The electrons impinging the sample couple to high lying unoccupied states and decay to lower unoccupied states by emitting photons, see Fig. 2.5(b). The energy and intensity of these photons are measured. The difference of the photon energy and the energy of the electron beam gives insight in the difference between the energy of the ground-state and the energy of the excited state which has one electron more. The probability of the transitions is mainly determined by the low lying empty states. Therefore one probes the unoccupied part of the spectrum with this technique. An example of inverse photoemission spectroscopy is the bremsstrahlung isochromat spectroscopy (BIS).

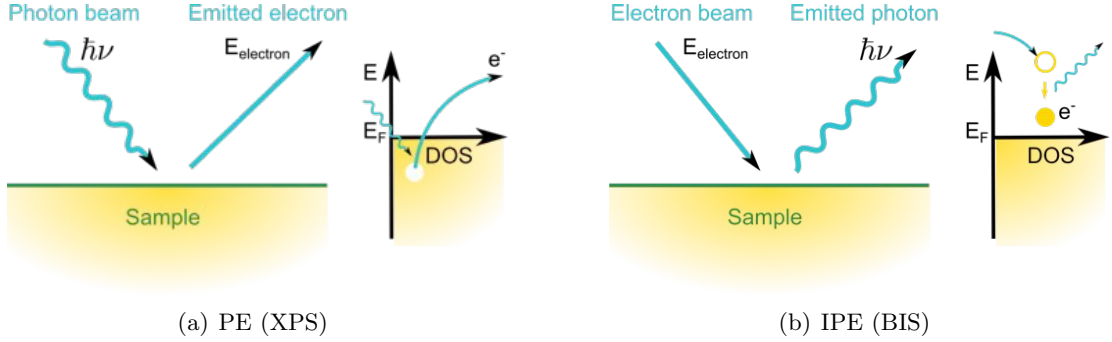


Figure 2.5: Schematic view of a photoemission experiment (left) and of an inverse photoemission experiment (right).

For XPS and BIS, the energy of the electron beam or the emitted electron is very high. In classical terms one could say that the speed of the electrons is very high. This means that the time interval of the interaction with the sample is very short. In comparison to this time interval, the lifetimes of the final excited states are much longer and can be approximated as infinite in the experiment. This means that one can describe the final states as a sudden (dis)appearance of an electron (from) to the original state. In XPS this state with $n - 1$ (passive) electrons can be described by the initial orbitals, only with a different occupation. Also for BIS, the state of the final $n + 1$ electrons can be described by occupying the initial orbitals of the ground-state.

In summary, we will use XPS for $f^n \rightarrow f^{n-1}$ transitions and BIS for $f^n \rightarrow f^{n+1}$ transitions to probe the $4f$ multiplet structure of the lanthanides. The spectra can actually be interpreted as a superposition of the density of states for the different angular momenta l weighted by their cross sections. For the energy range of our interest, the $f^n \rightarrow f^{n-1}$ and $f^n \rightarrow f^{n+1}$ transitions will turn out to be most important.

The cross sections give the probability for transitions from states with a certain angular momentum and depend on the photon energy of the impinging beam. The cross

sections can enhance or suppress states of a given angular momentum compared to states of a different angular momentum. This might, for different photon energies, change the relative heights in the XPS spectrum. This is especially important if one would like to compare the relative peak intensities of states belonging to states with different angular momentum character.

2.4.2 Experiment and theory

To compare experimentally measured spectra to theoretically calculated spectra, one has to take into account their differences. In the experimentally measured spectra, the peaks belonging to the different multiplets are not atomic sharp lines, but broad peaks. This has several different reasons. The first reason for the broadening is the lifetime of the excited state. To model the lifetime effects in a theoretical spectrum, one should broaden the spectrum with a Lorentzian. The second reason is the resolution of the measurement apparatus used in the experiment. To simulate this finite resolution in a theoretical spectrum, one should broaden the spectrum with a Gaussian, where the full width at half maximum (FWHM) is given by the resolution of the measuring equipment in the experiment which one would like to compare to. Other effects that might cause experimental broadening are the possible presence of hybridization or in metals the formation of electron-hole pairs over the Fermi surface. From the theoretical side there are also sources of broadening. A technical source of broadening arises from the fact that we evaluate the imaginary part of the Green's function just above the real axis, as will be explained in Eq. 3.20. An other reason that we do not see sharp multiplets defined by S , L and J is that these multiplets are split by crystal field into different J_z components or linear combinations thereof. For the lanthanides this splitting is usually small compared to the exchange splitting. The theory used in this licentiate thesis (HIA) can in principle capture the crystal field effects. However, in practice for technical reasons (no proper formulation of the double counting for crystal field), no one has yet managed to include it properly.

Another observation one can make about the experimental spectra is that there seems to be an overall increment in intensity as one goes away from the Fermi energy. This is due to the fact that some of the emitted electrons (XPS) or photons (BIS) scatter around before they are captured by the detector. By scattering they lose some energy. At the moment the electron (or photon) finally reaches the detector, a lower energy is measured. This means that the energy difference between the incoming photon beam (electron beam) and the outgoing electron (photon) becomes bigger. This results in an apparently higher difference between the ground-state energy and the excited state energy. These scattering processes contribute to a background which increases with each multiplet state, as illustrated in Fig. 2.6. In Fig. 2.6(a) the XPS process is shown schematically. One electron is excited and goes straight towards the detector. The other electron scatters before it reaches the detector. So, although both electrons originated from the same state, the second electron is detected with a lower energy. In Fig. 2.6(b) the theoretical (yellow) and experimental (orange) XPS intensities are shown schematically. In between the first and second peaks from the Fermi level the theoretical intensity (yellow line) goes, as expected, back to zero. However, the experimental intensity (orange line) does not go back to zero. The finite intensity is due to electrons from the first multiplet that have scattered around in the sample before reaching the detector. The even more increased intensities observed in-between the other multiplets arise from

electrons originating from any multiplet up to the Fermi level, with various scatterings before reaching the detector.

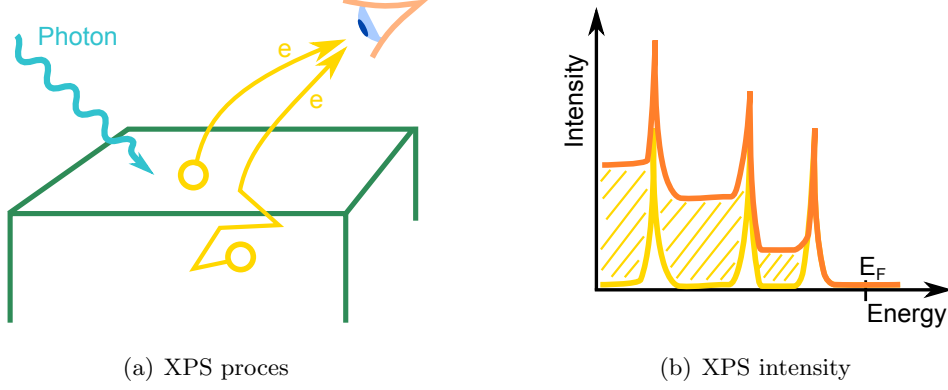


Figure 2.6: (a) Schematic view of an electron going directly to the detector and an other one scattering before reaching the detector. (b) Schematic view of how the experiment (orange line) measures the true peaks (yellow). The shaded areas are due to electrons undergoing extra scatterings before the electron leaves the sample.

2.4.3 Multiplet structure

The spectra of the lanthanides consist of several peaks. These peaks correspond to the transitions from the Hund's rule ground-state with f^n electrons and L , S and J quantum numbers, to different final states with f^{n-1} electrons (XPS) and f^{n+1} electrons (BIS) and quantum numbers L' , S' and J' , that are accessible from the Hund's rules ground-state. The crystal field is well screened by the valence electrons and the separation of the multiplet states is dominant [26].

Which of all possible f^{n-1} or f^{n+1} multiplets are accessible from the Hund's rules ground-state, can be determined using certain selection rules [1]. For XPS, where one electron is removed, $S - S' = \frac{1}{2}$. The maximal amount of angular momentum which can leave the system is $\pm l$, where l is the angular momentum quantum number of the shell where the electron is removed from. Therefore $|L - L'| \leq l$.

Let us consider, as an illustrative example, the multiplets in the XPS spectrum of Neodymium (Nd). In the solid phase, Nd has an f^3 configuration and XPS probes therefore $f^3 \rightarrow f^2$ transitions. The Hund's rule ground-state of Nd is $^4I_{9/2}$, where we used the term symbol notation $^{2S+1}L_J$. The total angular momentum J is calculated in the Russel-Saunders (LS) coupling scheme (Sec. 2.3.1), which is a good approximation for the lanthanide series [23]. All possible ways to arrange 2 electrons over the $-3 \leq m_l \leq 3$ and $m_s = \pm \frac{1}{2}$ orbitals, result in the following multiplets: 1I_6 , $^3H_{4,5,6}$, 1G_4 , 1S_0 , $^3F_{2,3,4}$, 1D_2 and $^3P_{0,1,2}$, see App. A for a recipe to obtain these multiplets. The multiplets with $2S + 1 = 1$ cannot be reached from the Hund's rule ground-state (f^3 configuration) where $2S + 1 = 4$, since S can at most change by $\frac{1}{2}$, corresponding to the spin that one electron can carry away. Hence 1I_6 , 1G_4 , 1S_0 and 1D_2 are not accessible. The state $^3P_{0,1,2}$ is also not accessible, since the angular momentum changes by more than 3, the maximal orbital momentum that one electron from the f -shell can carry away. We are

left with ${}^3H_{4,5,6}$ and ${}^3F_{2,3,4}$. Transitions to these states will appear in the XPS spectrum.

A similar approach can be done for the BIS spectra, considering that adding one electron is the same as removing one hole. The relative intensity of these different multiplets can be calculated from the coefficients of fractional parentage, which is explained in Ref. [1] for XPS and Ref. [7] for BIS. The coefficients of fractional parentage are tabulated in Ref. [1] for XPS and Chapter 62, Table I of Ref. [16] for BIS.

Chapter 3

Methods

In solid state physics the Hamiltonian describing a system of nuclei and electrons consists typically of 5 terms. Two kinetic terms, one for the electrons and one for the nuclei, and three Coulomb terms. The latter describe the Coulomb repulsion between the nuclei, the Coulomb attraction between the nuclei and the electrons, and the Coulomb repulsion between the electrons. For simplicity we will ignore the relativistic effects, but in principle using the Dirac equation instead of the Schrödinger equation is straight forward. Despite these simplifications, this Hamiltonian involves an enormous amount of particles and since everything is interacting with everything, the computational effort for a few atoms runs already out of control. In, amongst other fields, solid state physics, one usually uses the Born-Oppenheimer approximation [6]. The mass of the nuclei is much larger than the mass of the electrons. Given that the kinetic term is inversely proportional to the mass, the kinetic term of the nuclei is much smaller than the kinetic term of the electrons. Therefore, in order to describe the electronic degrees of freedom, one can decouple them from the ionic degrees of freedom. One approximates the nuclei as fixed at given positions. The Coulomb attraction that the ions exert on the electrons can now be described as a static external potential experienced by the electrons. The Hamiltonian for the electronic degrees of freedom becomes

$$\hat{H} = \frac{-\hbar^2}{2m_e} \sum_i \nabla_i^2 + \sum_i V_{\text{ext}}(\vec{r}_i) + \frac{1}{2} \sum_{i \neq j} \frac{e^2}{|\vec{r}_i - \vec{r}_j|} \quad (3.1)$$

where the indices i and j run over the different electrons. The first term is the kinetic term of the electrons, where \hbar is the Planck constant, m_e the electron mass and $-i\hbar\nabla$ the momentum operator. The second term is the external potential that the electrons experience due to the nuclei (at their fixed positions). The last term is the Coulomb repulsion between the electrons. It is precisely this last term which makes this problem still incredibly difficult to solve: all electrons interact with all electrons. Although this is still manageable for systems with a small amount of electrons, diagonalizing the Hamiltonian becomes quickly a problem when approaching macroscopic solids. However, that is precisely what one would like to do, since the eigenvalues of this Hamiltonian give the energy of the system and the eigenfunctions give the electron many-body wave functions.

In case one considers a crystal, the translational invariance of the crystal provides another simplification to the problem. In that case one can make use of the Bloch theorem [5]. It states that the wave function can be written as a periodic function, with

the same periodicity as the crystal lattice under consideration, times a plane wave, that is

$$\psi_{\vec{k}}(\vec{r}) = u_{\vec{k}}(\vec{r})e^{i\vec{k}\cdot\vec{r}} \quad (3.2)$$

where ψ is the one electron wave function and \vec{r} the position in space. The periodic function $u(\vec{r})$ has the same periodicity as the lattice and \vec{k} is the wave vector.

Although the Born-Oppenheimer approximation and the use of the Bloch theorem greatly simplify the task of solving the Hamiltonian in Eq. 3.1, it is still impossible for more than a few atoms and electrons. However, thanks to Pierre C. Hohenberg, Walter Kohn, Lu Jeu Sham and many others, we nowadays have a very successful way to tackle this problem in most cases: Density Functional Theory (DFT).

3.1 Density Functional Theory

Pierre C. Hohenberg and Walter Kohn came with a brilliant idea [19]. Roughly speaking, they stated that if you have the ground-state density of the particles in space and the interaction between the particles, you have, in principle access to any property of the system. They formulated and proved this in two theorems, known as the Hohenberg-Kohn theorems. These theorems, together with the Kohn-Sham *ansatz* [25] form the basic ideas behind Density Functional Theory (DFT). For me, *Electronic Structure* by Martin [29] proved to be a good reference for learning the fundamentals of DFT and electronic structure calculations, and therefore Sec. 3.1.1 and 3.1.2 will be mainly based on chapter 6 and 7 of this book.

3.1.1 Hohenberg-Kohn theorems

The Hohenberg-Kohn theorems shift the attention from the wave function, depending on the position vectors of all electrons simultaneously, to the density, which depends only on one position vector. Precisely formulated, the Hohenberg-Kohn theorems read:

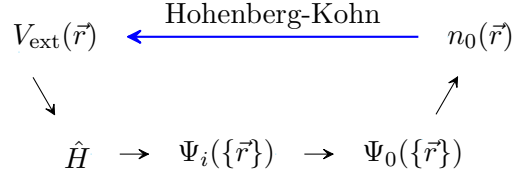
Theorem 1 *For any system of interacting particles in an external potential $V_{\text{ext}}(\vec{r})$, the potential $V_{\text{ext}}(\vec{r})$ is determined uniquely, except for a constant, by the ground-state particle density $n_0(\vec{r})$.*

Corollary 1 *Since the Hamiltonian is thus fully determined, except for a constant shift of the energy, it follows that the many-body wave functions for all states (ground and excited) are determined. Therefore all properties of the system are completely determined given only the ground-state density $n_0(\vec{r})$.*

Theorem 2 *A universal functional of the energy $E[n]$ in terms of the density $n(\vec{r})$ can be defined, valid for any external potential $V_{\text{ext}}(\vec{r})$. For any particular $V_{\text{ext}}(\vec{r})$, the exact ground-state energy of the system is the global minimum value of this functional, and the density $n(\vec{r})$ that minimizes the functional is the exact ground-state density $n_0(\vec{r})$.*

Corollary 2 *The functional $E[n]$ alone is sufficient to determine the exact ground-state energy and density. In general, excited states of the electrons must be determined by other means.*

The proofs of these theorems are surprisingly simple and are nicely explained in, for example, chapter 6 of *Electronic Structure* by Martin [29]. The basic idea of the first theorem can be summarized in the scheme below:



where Ψ is the many-body wave function, the subscript zero denotes the ground-state and all other Ψ_i are excited states. Starting from the external potential $V_{\text{ext}}(\vec{r})$ the route to obtain the density is known from quantum mechanics: constructing the Hamiltonian \hat{H} , solving the Schrödinger equation and obtaining the wave functions $\Psi_i(\vec{r})$, including the ground-state $\Psi_0(\vec{r})$, which gives the ground-state density $n_0(\vec{r})$. The first Hohenberg-Kohn theorem closes the circle: from the ground-state density the external potential is uniquely defined (except for a constant shift).

While the first Hohenberg-Kohn theorem claims that it is possible to find $V_{\text{ext}}(\vec{r})$ from $n_0(\vec{r})$, the second gives a clue how to find it. The second Hohenberg-Kohn theorem affirms the existence of a universal energy functional $E[n]$. One could split this functional into different terms belonging to the different terms in the Hamiltonian:

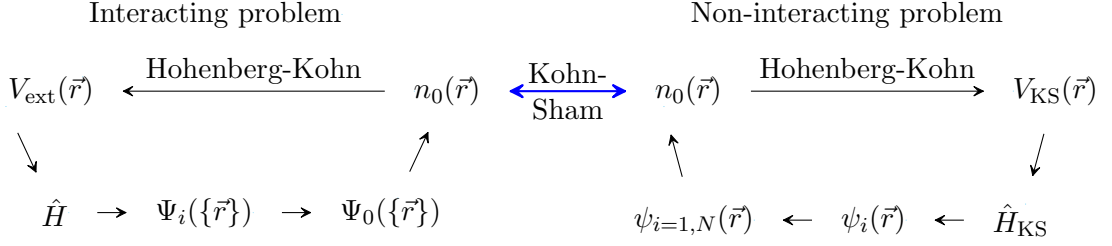
$$E_{\text{HK}}[n] = T[n] + E_{\text{int}}[n] + \int d^3r V_{\text{ext}}(\vec{r})n(\vec{r}) + E_{II} \quad (3.3)$$

The first term represents the kinetic energy of the electrons, while the second term represents the Coulomb interaction between the electrons. The third term is the energy associated to the external potential that the electrons experience due to the position of the nuclei. The last term is the energy of the nuclei.

3.1.2 Kohn-Sham *ansatz*

DFT would not be so important nowadays, if Walter Kohn and Lu Jeu Sham had not come up with a very useful *ansatz* [25]. Their idea was to replace the original (interacting) many-body problem with an auxiliary independent particle problem, where the auxiliary system is chosen such that the ground-state density is the same as the ground-state density of the interacting problem. The Kohn-Sham *ansatz* makes it possible to use independent particle methods to calculate, in principle exactly, the properties of a fully interacting many-body system. Combining the Hohenberg-Kohn theorems and the Kohn-Sham *ansatz* has proven to be remarkably successful. In fact, shifting the attention from the wave functions to the ground-state density makes it easier to find useful approximations.

In the scheme below we present the combination of the Hohenberg-Kohn theorems and the Kohn-Sham *ansatz*



where ψ_i is the i -th wave function in the non-interacting problem. By occupying the first N wave functions ψ_i one can form the ground-state. From the interacting problem one constructs an auxiliary non-interacting system with the same ground-state density. From this ground-state density, the auxiliary potential $V_{\text{KS}}(\vec{r})$ can, in principle, be constructed with the Hohenberg-Kohn theorems for a non-interacting system. Solving the Schrödinger equation for the non-interacting Hamiltonian \hat{H}_{KS} gives the wave functions $\psi_i(\vec{r})$. Occupying of the first N wave functions $\psi_{i=1,N}(\vec{r})$ gives the ground-state and the ground-state density. So, instead of solving the left (interacting) circle in the above scheme, we can solve the right (non-interacting) circle.

In the Hohenberg-Kohn theorems, the *universal functional* $E[n]$ plays an important role, but the theorems reveal nothing about the *exact* form of this functional. And that is precisely the problem: nobody knows the exact form of this functional. However, to connect the two circles, we have not only to know that V_{KS} exists, but also to find it. Given an appropriate form of V_{KS} , the Kohn-Sham *ansatz* leads to the Kohn-Sham equations (in Hartree units):

$$(\hat{H}_{\text{KS}} - \epsilon_i)\psi_i(\vec{r}) = 0 \quad (3.4a)$$

$$\hat{H}_{\text{KS}}(\vec{r}) = -\frac{1}{2}\nabla^2 + V_{\text{KS}}(\vec{r}) \quad (3.4b)$$

$$V_{\text{KS}}(\vec{r}) = V_{\text{ext}}(\vec{r}) + V_{\text{Hartree}}(\vec{r}) + V_{\text{XC}}(\vec{r}) \quad (3.4c)$$

$$E_{\text{KS}}[n] = T_s[n] + \int d^3r V_{\text{ext}}(\vec{r})n(\vec{r}) + E_{\text{Hartree}}[n] + E_{\text{II}} + E_{\text{XC}} \quad (3.4d)$$

$$n(\vec{r}) = \sum_{i=1}^N |\psi_i(\vec{r})|^2 \quad (3.4e)$$

The Kohn-Sham Hamiltonian \hat{H}_{KS} (Eq. 3.4b) is non-interacting, therefore Eq. 3.4a is numerically solvable in a finite Hilbert space. The many-body effects are hidden in the potential V_{KS} , more precisely in the exchange correlation part V_{XC} . In the Kohn-Sham potential, the complicated electron-electron interaction term is split into two parts. The main part is captured by the Hartree potential

$$V_{\text{Hartree}}(\vec{r}) = \frac{\delta E_{\text{Hartree}}[n]}{\delta n(\vec{r})} \quad (3.5)$$

where the Hartree energy is

$$E_{\text{Hartree}}[n] = \frac{1}{2} \int d^3r d^3r' \frac{n(\vec{r})n(\vec{r}')}{|\vec{r} - \vec{r}'|} \quad (3.6)$$

which is the electron density interacting with itself. The remaining part is included in the exchange correlation potential, which is the last term in Eq. 3.4c. Apart from this, the exchange correlation potential includes the differences between the real (interacting) kinetic energy and the Kohn-Sham approximation of it; i.e. the non-interacting kinetic energy $T_s[n]$. The exchange correlation energy (E_{XC} in Eq. 3.4d) is given by comparing the Kohn-Sham energy (Eq. 3.4d) with the Hohenberg-Kohn energy (Eq. 3.3). This is however a formal definition that is not super useful since we do not know the Hohenberg-Kohn energy.

The Kohn-Sham equations built an effective potential from a density and an external potential. This effective potential results into a new density and so on. Therefore the Kohn-Sham equations must be solved self-consistently in the effective potential and the density. This is schematically shown in Fig. 3.1. As a self consistent method, the Kohn-Sham approach uses independent particle techniques, but describes interacting densities.

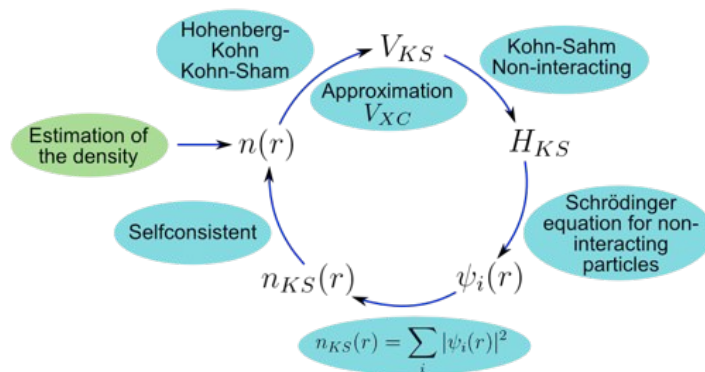


Figure 3.1: Schematic view of the DFT cycle: solving the Kohn-Sham equations self-consistently.

The Kohn-Sham *ansatz* makes it possible to do very good approximations to the energy functional. The Hohenberg-Kohn energy functional was unknown. Kohn and Sham separated out the kinetic energy of non-interacting particles and the Hartree part of the Coulomb interaction. This means that the unknown part (the exchange correlation energy) consists now of two (hopefully) small terms. 1. The difference between the interacting and non-interacting kinetic energies. 2. The difference between the Hartree energy and the full electron-electron interaction energy. The Hartree term includes the long-range Coulomb interaction. Therefore the exchange-correlation energy can reasonably well be approximated by a local, or nearly local, quantity. This short range character of V_{XC} is the main cause of the huge success of DFT. Without this main progress in approximating the unknown exact universal energy functional, density functional theory would not be so successful.

3.1.3 Approximations to the energy functional

The exact functional to go from the density $n(\vec{r})$, in the scheme in Fig. 3.1, to the Kohn-Sham potential $V_{KS}[n]$ is unfortunately not known. Despite that, DFT became very

successful and that is mainly because of two reasons. On one hand, the Kohn-Sham approach allows one to use independent particle theories to solve a fully interacting many-body problem. On the other hand, the fact that the long range Coulomb interactions (Hartree term) and the independent particle kinetic energy are separated out, allows one to approximate the exchange correlation functional by a quantity that is approximately local. This has resulted in very good approximations, such as the Local (Spin) Density Approximation (L(S)DA) and the Generalised Gradient Approximation (GGA). This paragraph will shortly describe these two functionals. A more elaborate overview of these and other functionals can be found in, for example, chapter 8 of *Electronic Structure* by Martin [29].

Electrons in solids resemble very often nearly-free electrons. Therefore the uniform electrons gas was chosen as a starting point to construct the first approximation of the exchange correlation functional. In the uniform electron gas, the exchange correlation energy is local. In the Local Density Approximation (LDA), the exchange correlation functional is directly derived from the uniform electron gas and thus local. The exchange energy is calculated analytically from the uniform electron gas and the correlation energy is approximated very well by Monte Carlo calculations on the uniform electron gas. The proposed LDA functional has the same functional dependence on the density as found in the uniform electron gas. The only difference is that the uniform density $n = N/V$ is replaced by the density at a given point $n(\vec{r})$. The Local Spin Density Approximation is a straightforward spin dependent generalization of LDA. Usually the L(S)DA functional works very well, since the range of the effects of exchange and correlation is generally small. However, the approximations made, are not based on a formal expansion around some small parameter. Therefore, it can not be formally proven whether the local approximation will work for a general case or not. The validity of the local approximation should be tested for each case by comparing theory and experiment or calculated and exact solutions, if available. Nonetheless, the DFT community has developed some intuition on the applicability of different functionals. One expects the LDA functionals to perform well for systems where the electrons behave as nearly-free, and one expects them to work very bad for systems where the electron density is distributed very inhomogeneously in space.

An intuitive first step to improve the LDA functionals is to include, the dependency on not only the density in a specific point, but also on the gradient of the density in that point. The first attempts to include the gradients did not work very well, and especially for large gradients the expansions performed poorly. But later on more elaborate ways of taking the gradient of the density into account were developed and named Generalised Gradient Approximation (GGA). The GGA functionals perform generally better than the LDA functionals. For example, where the LDA functional usually overestimates the bonding and gives a too small volume, the GGA functionals predict equilibrium volumes that are closer to experimental values.

3.2 Hubbard I approximation

In the lanthanides, the $4f$ electrons are very localized. The LDA or GGA functionals, which are based on the uniform electron gas, are, as one can imagine, bad approxi-

mations to describe such localized electrons. On the other hand, the $[spd]$ bonding electrons are very delocalized and DFT-LDA (or GGA) can describe them very well. There are different methods to include the effects of (strong) localization in different types of situations. The two standard computational methods nowadays are LDA+U (Hartree-Fock) or LDA+Dynamical Mean-Field Theory (LDA+DMFT). The latter is much more sophisticated than the former. Historically both approaches originated from the following observations. It had been found that the usual LDA (GGA) approach can not describe the localized nature of, for example, the $4f$ electrons or other correlated materials. Surprisingly, the Hubbard model [20, 21, 22], with parameters obtained from LDA, had been shown to describe various correlated materials very well [8, 33, 18, 17, 30]. The observations of this procedure lead to the idea of embedding the model Hamiltonian into DFT. The advantage is that the properties arising from the Hubbard model merged with DFT become now material-dependent quantities. The main idea is that an explicit Hubbard term can be added to the LDA-Hamiltonian for the strongly localized electrons. This corrected Hamiltonian can now be solved with different methods like LDA+U or LDA+DMFT. In both LDA+U and LDA+DMFT this Hamiltonian is mapped onto a Single Impurity Anderson Model (SIAM). In LDA+U this is then solved in the Hartree Fock approximation. In LDA+DMFT the SIAM is solved with one of the possible “solvers”. In this licentiate thesis the Hubbard I Approximation (HIA) is used as an approximated solver of the SIAM. The HIA provides a good method to describe the lanthanides, since the $4f$ electrons are very localized and the hybridization of the f electrons is very small.

Roughly speaking the main idea of the Hubbard I approximation is to combine the many-body structure of the $4f$ states, given by the atomic multiplets, with the broad bands of the delocalized valence electrons, see Fig. 3.2. In Sec. 3.2.1, 3.2.2 and 3.2.3 these intuitive ideas will be substantiated with some formulas. The following sections will aim at illustrating the main idea of DMFT. To include correlation effects, an on-site Coulomb repulsion tensor U is added to the Kohn-Sham Hamiltonian. The new Hamiltonian obtained in this way is rewritten in the form of a Hubbard Hamiltonian. The latter is solved through a mapping onto a SIAM. This SIAM has to be solved to recover the solution of the initial problem. The Hubbard I approximation can be seen simply as a particular approach to solve the SIAM. In summary, we will go step by step through the following scheme:

$$\hat{H}_{LDA} + \hat{U} = \dots = \hat{H}^{\text{Hubbard Model}} \longrightarrow \hat{H}^{\text{Anderson Model}} \xrightarrow{\text{approximations}} \text{Solution}$$

In Sec. 3.2.1 we explain how to merge DFT with the Hubbard model. In Sec. 3.2.2 the mapping procedure to the SIAM is explained. Finally we explain how the Hubbard I approximation is implemented in RSPt [38] in Sec. 3.2.3. RSPt is a full-potential electronic structure code based on linear muffin tin orbitals. The acronym stands for Relativistic Spin-Polarized test. More details about the code and the linear muffin tin orbitals can be found in Ch. 4. The following sections are based on introductory lectures of Antoine Georges [13] and the PhD thesis of Igor Di Marco [10].

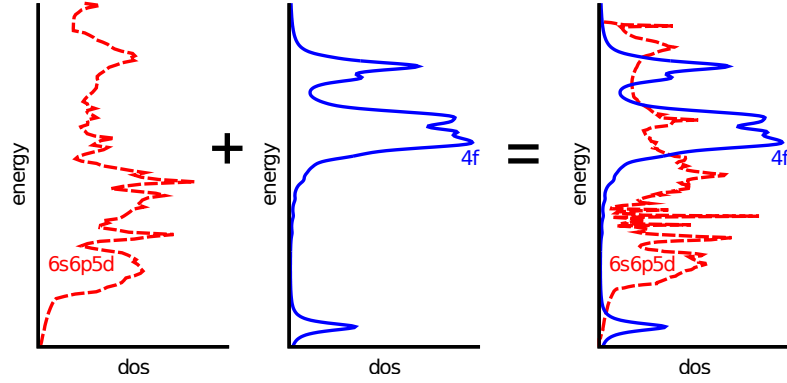


Figure 3.2: The idea of the Hubbard I approximation is to combine the LDA (GGA) description of the delocalized conduction electrons (red dashed density of states) with the atomic multiplets of the localized 4f electrons (blue solid multiplets).

3.2.1 Effective Hubbard model

This section is about merging the Hubbard model with DFT, the blue part (left) of the illustrating scheme introduced in the previous section

$$\hat{H}_{LDA} + \hat{U} = \dots = \hat{H}^{\text{Hubbard Model}} \longrightarrow \hat{H}^{\text{Anderson Model}} \xrightarrow{\text{approximations}} \text{Solution}$$

The LDA+DMFT approach is based on the idea of merging LDA and the Hubbard model. In a heuristic way, one adds a Hubbard interaction term to the DFT-LDA Hamiltonian for those orbitals where the description in LDA is not good enough due to strong on-site Coulomb repulsion. The adjusted Hamiltonian reads

$$\hat{H} = \hat{H}_{LDA} - \hat{H}_{DC} + \frac{1}{2} \sum_{\mathbf{R}} \sum_{\xi_1, \xi_2, \xi_3, \xi_4} U_{\xi_1, \xi_2, \xi_3, \xi_4} \hat{c}_{\mathbf{R}, \xi_1}^\dagger \hat{c}_{\mathbf{R}, \xi_2}^\dagger \hat{c}_{\mathbf{R}, \xi_4} \hat{c}_{\mathbf{R}, \xi_3} \quad (3.7)$$

The orbitals (on site \mathbf{R}) for which the local correction tensor U is added, are usually called the “correlated orbitals”. This set of orbitals is labeled by the Bravais lattice site vector \mathbf{R} and a general orbital index ξ . Later on we will split ξ in the well-known quantum numbers. In an atomic-like basis this would correspond to the spin-orbitals $\{l, m, \sigma\}$. The operators $\hat{c}_{\mathbf{R}, \xi}^\dagger$ and $\hat{c}_{\mathbf{R}, \xi}$ are the creation and annihilation operators for electrons in the correlated orbitals. The second term \hat{H}_{DC} is the double counting term, which subtracts from \hat{H} those terms that are due to added U but are already included in the LDA Hamiltonian. The latter should in principle contain all terms of the original Hamiltonian (Eq. 3.1) and we do not want to count some contributions twice. This term has the form $\hat{H}_{DC} \sim A \sum_{\xi_1} \hat{c}_{\mathbf{R}, \xi_1}^\dagger \hat{c}_{\mathbf{R}, \xi_1}$ and is sometimes merged with the chemical potential. We will elaborate more on this term in Fig. 3.4 and Sec. 3.2.5, but for now let us ignore it.

The LDA Hamiltonian \hat{H}_{LDA} can be expressed as the sum over the Kohn-Sham Hamiltonians $\hat{H}_{KS}^{\sigma_i}(\mathbf{r}_i)$ for all $i = 1, N$ electrons, with spin σ_i on position \mathbf{r}_i . If we choose a basis of one particle wave functions, which are centered at site \mathbf{R} and labeled by a set of quantum numbers χ , we can express the first term in Eq. 3.7

$$\hat{H}_{LDA} = \sum_{i=1}^N \hat{H}_{KS}^{\sigma_i}(\mathbf{r}_i) = \sum_{\mathbf{R}_1 \chi_1} \sum_{\mathbf{R}_2 \chi_2} t_{\mathbf{R}_1 \chi_1, \mathbf{R}_2 \chi_2} \hat{c}_{\mathbf{R}_1 \chi_1}^\dagger \hat{c}_{\mathbf{R}_2 \chi_2} \quad (3.8)$$

where the hopping matrix t is defined by the elements

$$t_{\mathbf{R}_1\chi_1, \mathbf{R}_2\chi_2} = \int d\mathbf{r} \langle \mathbf{R}_1\chi_1 | \mathbf{r} \rangle \hat{H}_{KS}^{\sigma\chi_2}(\mathbf{r}) \langle \mathbf{r} | \mathbf{R}_2\chi_2 \rangle \quad (3.9)$$

With this rewriting it can be seen that the Hamiltonian as defined in Eq. 3.7 looks very similar to the Hamiltonian of the Hubbard model. The hopping t comes from the DFT-LDA problem and the Coulomb repulsion tensor U is added on top of that. Note however that U is not the bare Coulomb repulsion, but an effective interaction. This effective interaction is based on the Coulomb repulsion, but is screened by the other electrons. We will discuss the heuristically added U -tensor later, in Sec. 3.2.4.

3.2.2 Effective Single impurity Anderson model

An efficient way to solve the Hubbard model is the dynamical mean-field theory. In DMFT the effective Hubbard model, introduced in Sec. 3.2.1, is mapped onto an effective model, the single impurity Anderson model (SIAM). This is the second half of the scheme below

$$\hat{H}_{LDA} + \hat{U} = \dots = \hat{H}^{\text{Hubbard Model}} \xrightarrow{\hspace{1cm}} \hat{H}^{\text{Anderson Model}} \xrightarrow{\text{approximations}} \text{Solution}$$

The SIAM consists of a single impurity embedded in an effective field. This corresponds to solving the problem in a mean-field approach for the space degrees of freedom. However, the quantum degrees of freedom at a single site are still accounted exactly. The effective Hamiltonian, which is the Hamiltonian of the single impurity Anderson model, describes the impurity, the effective bath and the coupling between them:

$$\hat{H}_{eff} = \hat{H}_{atom} + \hat{H}_{bath} + \hat{H}_{coupling} \quad (3.10)$$

For simplicity we will assume for now a one orbital case. Assuming the single orbital level to be located at the Fermi level, the atomic Hamiltonian reads

$$\hat{H}_{atom} = U \hat{c}_{\uparrow}^{\dagger} \hat{c}_{\uparrow} \hat{c}_{\downarrow}^{\dagger} \hat{c}_{\downarrow} \quad (3.11)$$

where the \hat{c} -operators denote the creation (\hat{c}^{\dagger}) and annihilation (\hat{c}) of electrons in the impurity orbital. The second term of Eq. 3.10 represents the bath, which may consist of real conduction electrons, as in the original SIAM, or also of fictitious electrons, as in DMFT. For spin σ , wave vector \mathbf{k} and energy $\epsilon_{\mathbf{k},\sigma}$, the bath term is

$$\hat{H}_{bath} = \sum_{\mathbf{k},\sigma} \epsilon_{\mathbf{k},\sigma} \hat{a}_{\mathbf{k},\sigma}^{\dagger} \hat{a}_{\mathbf{k},\sigma} \quad (3.12)$$

where the \hat{a} -operators denote the creation (\hat{a}^{\dagger}) and annihilation (\hat{a}) of electrons in the bath. Finally the last term of Eq. 3.10 represents the coupling between the impurity (\hat{c} -operators) and the bath (\hat{a} -operators)

$$\hat{H}_{coupling} = \sum_{\mathbf{k},\sigma} V_{\mathbf{k},\sigma} (\hat{a}_{\mathbf{k},\sigma}^{\dagger} \hat{c}_{\sigma} + \hat{c}_{\sigma}^{\dagger} \hat{a}_{\mathbf{k},\sigma}) \quad (3.13)$$

To complete the mapping procedure, one has to find the mapping parameters $\epsilon_{\mathbf{k},\sigma}$ and $V_{\mathbf{k},\sigma}$. In the mapping procedure, the local Green's function at a single site should be

conserved from the original system (Hubbard model) to the effective system (SIAM). The local Green's function at a single site (in the real system) is defined as

$$G_{\mathbf{R},\mathbf{R}}^{\sigma}(\tau - \tau') \equiv -\langle \mathcal{T} \hat{c}_{\mathbf{R},\sigma}(\tau) \hat{c}_{\mathbf{R},\sigma}^{\dagger}(\tau') \rangle \quad (3.14)$$

where \mathcal{T} denotes the time ordering operator and τ the imaginary time in the Matsubara formalism. To impose the conservation of the local Green's function, the local Green's function that follows from our effective Hamiltonian Eq. 3.10 (the impurity Green's function) is needed too. To calculate this Green's function, we separate the only term that has two particles involved from the rest. The latter is \hat{H}_{bath} plus $\hat{H}_{coupling}$ plus the unperturbed level position. They determine the bare Green's function, which coincides in the SIAM with the bath Green's function. The bare Green's function as a function of the Matsubara frequencies ω_n is

$$\mathcal{G}_0^{\sigma}(i\omega_n) = \frac{1}{i\omega_n + \mu - \Delta^{\sigma}(i\omega_n)} \quad (3.15)$$

where Δ^{σ} is called the hybridization function and contains the parameters $\epsilon_{\mathbf{k},\sigma}$ and $V_{\mathbf{k},\sigma}$ of the effective system

$$\Delta^{\sigma}(i\omega_n) = \sum_{\mathbf{k}} \frac{|V_{\mathbf{k},\sigma}|^2}{i\omega_n - \epsilon_{\mathbf{k},\sigma}} \quad (3.16)$$

We can now formally rewrite the effect of the two-particle term contained in \hat{H}_{atom} in the form of a self-energy function $\Sigma_{imp}^{\sigma}(i\omega_n)$. This function can be determined by several techniques, named “solvers”. Once we have Σ , the Dyson equation gives the impurity Green's function

$$G_{imp}^{\sigma}(i\omega_n) = \frac{1}{\mathcal{G}_0^{\sigma}(i\omega_n)^{-1} - \Sigma_{imp}^{\sigma}(i\omega_n)} \quad (3.17)$$

To complete the mapping procedure, one has to find $\epsilon_{\mathbf{k},\sigma}$ and $V_{\mathbf{k},\sigma}$ and the consequent hybridization function Δ and self-energy Σ that reproduce the correct G_{imp}^{σ} , such that $G_{imp}^{\sigma}(i\omega_n) = G_{\mathbf{R},\mathbf{R}}^{\sigma}(i\omega_n)$. This is the core ingredient of the mapping procedure. There are several ways to find these parameters. In Dynamical Mean-Field Theory (DMFT), the approximation is made that the self-energy is local or in other words k -independent. Therefore it can be related to the impurity self-energy as

$$\Sigma_{\mathbf{R}\mathbf{R}'}^{\sigma}(i\omega_m) = \delta_{\mathbf{R}\mathbf{R}'} \Sigma_{imp}^{\sigma}(i\omega_m) \quad (3.18)$$

This DMFT approximation becomes exact in three limiting cases. The first case is the limit of infinite nearest neighbors or infinite dimensions, as was proven by Metzner and Vollhardt in Ref. [31]. The second limit is the non-interacting limit where the U in Eq. 3.7 is zero. This implies that the self-energy is zero and thus trivially local. The third limit is the atomic limit, where the hopping between nearest neighbors in Eq. 3.8 becomes zero $t_{R_1,R_2} = \delta_{R_1,R_2}$. With zero hopping the hybridization in Eq. 3.16 is zero which implies that the self-energy has only on-site components and is thus local. The Hubbard I approximation, which is an approximate solver to the SIAM in DMFT, is build upon this limit. It requires an additional approximation on top of the DMFT approximation. The last term in the Hamiltonian of the effective system (Eq. 3.10), the coupling between the bath and the impurity, is neglected. This boils down to approximating the self-energy in the impurity problem by the atomic self-energy. Hence the approximation becomes

$$\Sigma_{\mathbf{R}\mathbf{R}'}^{\sigma}(i\omega_m) = \delta_{\mathbf{R}\mathbf{R}'} \Sigma_{at}^{\sigma}(i\omega_m) \quad (3.19)$$

The above described procedure, where the Hubbard model (Eq. 3.7) is mapped onto the single impurity Anderson model (Eq. 3.10) and then approximated by an atomic problem is schematically depicted in Fig. 3.3. The mapping procedure is now, of course,

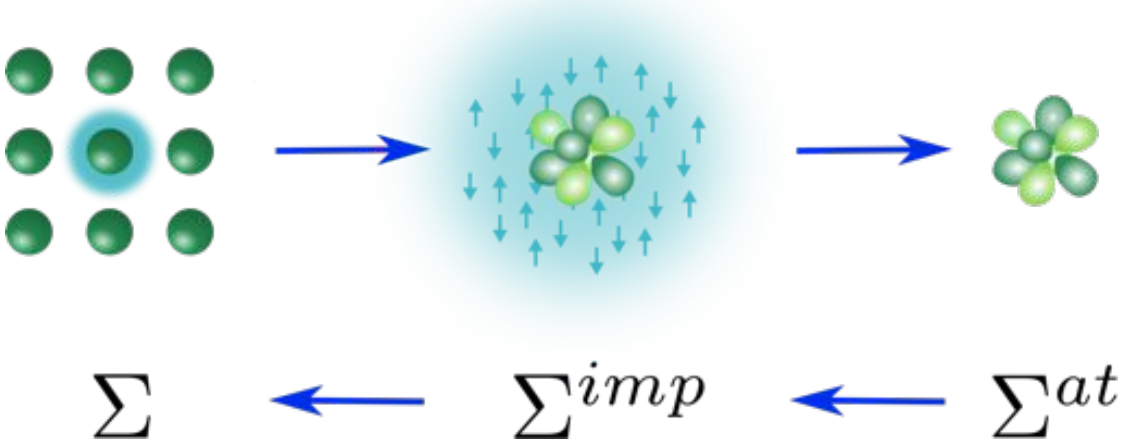


Figure 3.3: In the Hubbard I approximation the lattice problem is mapped to an impurity problem which is simplified into an atomic problem. The self-energy is calculated in the simplified case and the real self-energy is approximated by the atomic self-energy.

far from exact. A crucial approximation ($V_{\mathbf{k},\sigma} = 0$) is made and this method can only give sensible results if the correlated orbitals are close to atomic-like. Or, in other words, if the hybridization between the correlated orbitals and the rest (correlated orbitals on different atoms, and not-correlated orbitals on same or different atoms) is very small.

3.2.3 Computational scheme

For our calculations on the rare earths, we used the Hubbard I approximation as implemented in the Full Potential Linear Muffin Tin Orbital (FP-LMTO) code RSPt [38]. In this paragraph we will explain schematically how the computational scheme of the Hubbard I approximation works.

In Fig. 3.4 the computational scheme for the Hubbard I approximation is sketched. The Kohn Sham Hamiltonian H_{KS} , coming from the DFT-LDA part in a global basis χ (see also Sec. 3.2.1), is projected onto the correlated states denoted with a generic set of quantum numbers ξ on site \mathbf{R} . In case of the lanthanides, H_{KS} is projected onto the atomic-like $4f$ states. The resulting Hamiltonian $\hat{H}_{0\mathbf{R}}^{at}$, is written on a many-body basis of Fock states and the on-site Coulomb repulsion tensor U is added. The term containing the on-site Coulomb repulsion U (Eq. 3 in Fig. 3.4) takes into account the repulsion between two electrons on the same site \mathbf{R} . The terms $(\mu + \Delta\mu_{at} + \mu_{DC})$ take into account the chemical potential of the Green's function coming in the first iteration from the LDA calculation, the correction due to the fact that the hybridization is ignored in the Hubbard I approximation and the double counting correction. In Sec. 3.2.5 we will elaborate a bit more on these terms and will explain why $\hat{H}_{DC} \rightarrow \mu_{DC}$ with respect to Eq. 3.7. Diagonalisation of the matrix (Eq. 3 in Fig. 3.4) gives the eigenvalues E_μ and the eigenstates $|\mu\rangle$. Using the Lehman representation, the full atomic Green's function

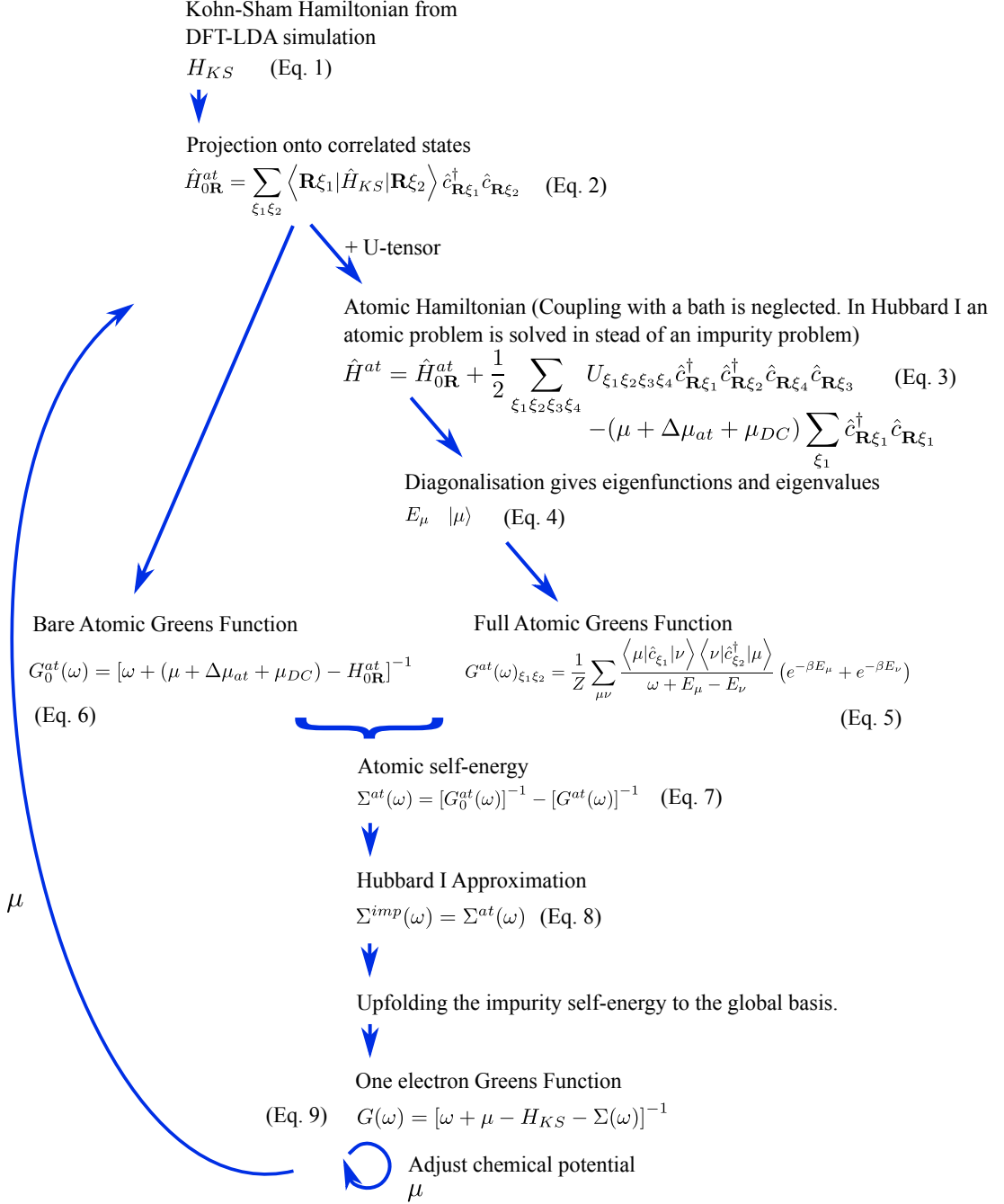


Figure 3.4: Schematic view of the HIA cycle. The creation and annihilation operators of the correlated orbitals are denoted with respectively $c_{\mathbf{R}\xi_i}^\dagger$ and $c_{\mathbf{R}\xi_i}$. The other symbols are explained in the text.

G^{at} (Eq. 5 in Fig. 3.4) is constructed. The full atomic Green's function (G^{at}) and the bare atomic Green's function G_0^{at} (Eq. 6 in Fig. 3.4) can be used in the Dyson equation to construct the self-energy Σ_{at} . The self-energy includes, as usual, the interactions of the system. The Hubbard I approximation (Eq. 8 in Fig. 3.4) consists in stating that the self-energy of the impurity Σ_{imp} is equal to the atomic self-energy, as is schematically shown in Fig. 3.3. After upfolding the self-energy to the global basis, the one electron Green's function G (Eq. 9 in Fig. 3.4) is constructed. For self-consistency, the chemical potential μ is fed back into the calculations, after it was adjusted to get the right amount of particles. In Eq. 9 in Fig. 3.4 the atomic features and the delocalized electrons are combined. For a charge self-consistent calculations, the density of the delocalized electrons has to be recalculated taking the new density of the localized electrons into account. This results in a slightly different H_{KS} in Eq. 1 in Fig. 3.4. The loop has to be repeated until Σ does not change significantly anymore between consecutive iterations.

To relate to physical observables, the spectral function can be calculated. It is given by

$$\rho(\omega) = -\frac{1}{\pi} \text{Im} [G(\omega + i\delta)] \quad \delta \rightarrow 0 \quad (3.20)$$

where δ approaches 0 from the positive site. In computations it will never be exactly zero and causes therefore a broadening in the spectrum.

3.2.4 Hubbard U and Hund's J

In the discussion on our calculations for the rare earths, we frequently refer to the Hubbard U and Hund's J . In this section we will give an intuitive picture of their physical meaning and relate them to the Coulomb U -tensor, which is added to the LDA Hamiltonian in Eq. 3.7.

To understand the physical meaning of the parameters U and J more precisely, Eq. 3.7 can be rewritten. When considering only intra-site and intra-shell interactions, one can omit the site index and shell index. Moreover the U -tensor does not affect the spin. We take a d band in a cubic environment as an example. Here the degeneracy is lifted, and the three-fold degenerate T_{2g} state is normally lower than the two-fold degenerate E_g state. For real valued wave functions, only four terms in the U -tensor are not equal to zero. When taking these considerations into account, the Coulomb interaction term can be rewritten in a more intuitive form. In App. B we assumed that the orbitals are atomic like, we omitted the sum over \mathbf{R} and replaced the generic set of quantum numbers ξ with the quantum numbers for the real spherical harmonics m . The final result is

$$\hat{H}_{Coulomb} = \frac{1}{2} \sum_{m,m',\sigma} U_{mm'} \hat{n}_{m\sigma} \hat{n}_{m'\bar{\sigma}} \quad (3.21a)$$

$$+ \frac{1}{2} \sum_{m,m',\sigma} (U_{mm'} - J_{mm'}) \hat{n}_{m\sigma} \hat{n}_{m'\sigma} \quad (3.21b)$$

$$- \frac{1}{2} \sum_{m,m',\sigma} J_{mm'} \left(\hat{c}_{m\sigma}^\dagger \hat{c}_{m\bar{\sigma}}^\dagger \hat{c}_{m'\sigma} \hat{c}_{m'\bar{\sigma}} + \hat{c}_{m\sigma}^\dagger \hat{c}_{m\bar{\sigma}} \hat{c}_{m'\bar{\sigma}}^\dagger \hat{c}_{m'\sigma} \right) \quad (3.21c)$$

The different parts of the U -tensor are replaced by $U_{mm'}$ for the direct Coulomb repulsion and $J_{mm'}$ for the Coulomb exchange, which is done in App. B. Now only two indices are sufficient instead of the original four. For spins opposite to σ , we introduced $\bar{\sigma}$. The term 3.21a gives the repulsion between two electrons with opposite spin, while the term 3.21b

gives the repulsion between two electrons with the same spin, which should, according to Pauli, be in different orbitals. The first term in 3.21c describes the transition of a pair of electrons with opposite spins from one orbital to the other. The second term in 3.21c describes a spin flip in the orbital m , accompanied by the opposite spin flip in the orbital m' .

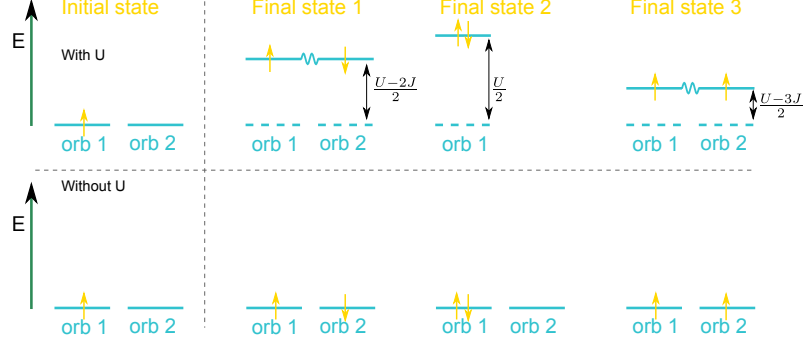


Figure 3.5: Schematic view of how the Hubbard U and Hund's J shift the “energy levels”. Energy levels are an intuitive way of understanding these numbers, but are a bit difficult to grasp in case of a many-body state. In the initial case we have one electrons and two orbitals. In the final case, we have two electrons and a many-body state, which might be a sort of combination between the original two orbitals. This combination is denoted with a wiggly line between the orbitals. The position of the many-body orbital is such that, in order to obtain the energy of the system, you have to take the energy of the energy level times the occupancy of the level. The most left plots correspond to the initial situation with one electron in orbital 1. In the second column an electron with opposite spin is added to the second orbital. In the third column an electron with opposite spin is added to the same orbital and in the last column an electron with same spin is added to (of course) the other orbital. The top panels show the shift of the energy levels in the situation where the Coulomb repulsion is taken into account. The bottom panels show the situation where it is not taken into account, so the one electron theory.

If we neglect the terms in Eq. 3.21c, the parameters $U_{mm'}$ and $J_{mm'}$ can be related¹ to the Hubbard U and Hund's J [12]

$$\begin{aligned} m = m' &\Rightarrow U_{mm} = U \\ m \neq m' &\Rightarrow U_{mm'} = U - 2J \\ &\quad J_{mm'} = J \end{aligned} \tag{3.22}$$

To understand the meaning of U and J , we can look at the picture in Fig. 3.5. This figure is a schematic view of a system consisting of two degenerate orbitals and initially one electron in orbital 1. The question is, what is the energy cost to add 1 electron to this system? We could add this second electron in three ways and the energy cost ΔE can be found by applying the Hamiltonian in Eq. 3.21 to the initial state, which gives 0, and to the final state. The three possible energy costs for adding an electron are

1. With opposite spin in the second orbital: $\Delta E = \frac{U_{12}}{2} + \frac{U_{21}}{2} = U - 2J$
2. With opposite spin in the same orbital: $\Delta E = \frac{U_{11}}{2} + \frac{U_{11}}{2} = U$

¹Actually there is also a constraint on the Slater integrals which will be defined later in this text, in (Eq. 3.24), namely the $F^4 \ll F^6$.

3. With the same spin in the second orbital: $\Delta E = \frac{U_{12}-J_{12}}{2} + \frac{U_{21}-J_{21}}{2} = U - 3J$

This offers a schematic view of different contributions to the U -matrix, but several approximations have been performed. Therefore, in our method, we follow a different strategy and work directly with the full U -tensor, which we parametrize with help of its expansion in spherical harmonics. This is possible because of the atomic-like orbitals. The expansion is given by

$$U_{m_1\sigma_1,m_2\sigma_2,m_3\sigma_3,m_4\sigma_4} = \delta_{\sigma_1,\sigma_3}\delta_{\sigma_2,\sigma_4} \sum_{n=0}^{2l} a_n(m_1, m_3, m_2, m_4) F^n \quad (3.23)$$

where the δ s ensure that the interaction does not change the spin of the electrons. The parameters a_n are integrals over products of three spherical harmonics. Their form is such that they are only non-zero if n is even and $n \leq 2l$. The Slater integrals F^n are given by

$$F^n = \int_0^\infty \int_0^\infty dr dr' r^2 r'^2 |\phi(r)|^2 |\phi(r')|^2 \frac{r_{<}^n}{r_{>}^{n+1}} \quad (3.24)$$

where ϕ are the atomic radial wave functions and $r_{<}$ and $r_{>}$ denote the lesser and the greater between r and r' . The parameters U and J from Eq. 3.22 are related to the Slater integrals F^0 , F^2 , F^4 and F^6 (these are the only Slater integrals that contribute for f systems). The Hubbard U corresponds to the zeroth Slater integral $F^0 = U$ and is usually heavily screened. Therefore calculating F^0 directly from Eq. 3.24 would not be very sensible. However F^2 , F^4 and F^6 do not suffer as much from this problem and therefore calculating them is preferable above introducing a parameter. The Hund's J for f systems is given by $J = \frac{1}{6435}(286F^2 + 195F^4 + 250F^6)$ [10].

3.2.5 Double counting

Finally we elaborate a bit more on \hat{H}_{DC} in Eq. 3.7. This term results in the last terms in Eq. 3 of Fig. 3.4, i.e. $(\mu + \Delta\mu_{at} + \mu_{DC})$. The first term μ is the chemical potential obtained from the DFT-LDA calculation in the first iteration and thereafter modified to account for the self-energy. When adding the U -tensor, we add a strong Coulomb repulsion among $4f$ orbitals. However, this repulsion is already taken into account in the DFT-LDA Hamiltonian, although it is not described correctly. Therefore one needs to correct for this double counting with a rigid shift, μ_{DC} . Moreover, in HIA, we neglect the coupling between impurity and bath, when mapping the electronic structure problem onto SIAM. The term $\Delta\mu_{at}$ should in principle enforce the conservation of the particle number between the SIAM and the atomic model obtained in HIA, but in practice is not needed. These two terms $\Delta\mu_{at}$ and μ_{DC} , are rigid shifts, and are unknown, so they can sometimes be grouped together into one term. Correcting for the double counting is a somewhat arbitrary procedure and different schemes for it have been proposed. Some double counting schemes used in this licentiate thesis are summarized in Tab. 3.1 and some examples are shown in Sec. 6.3.

Position of the first (un)occupied peak When comparing calculated spectra to experimental data, it might be useful to choose a double counting correction such that the position of one of the peaks in the calculation is exactly the same as in the experiment. This introduces an extra parameter, namely the position of the first occupied or the first

Table 3.1: Double counting corrections

Double counting scheme	Input	Determines
Position of the first (un)occupied peak	N_{at}, E_{peak}	$(\Delta\mu_{at} + \mu_{DC})$ μ is determined self-consistently
Fully Localized Limit (N)		$\mu_{DC} + \Delta\mu_{at} = H_{DC}(N)$ μ is determined self-consistently
Fully Localized Limit (N_{at})		$\mu_{DC} + \Delta\mu_{at} = H_{DC}(N_{at})$ μ is determined self-consistently

unoccupied peak, but it makes comparison much easier. This double counting correction is implemented such that once μ has been determined to obtain the correct number of electrons in the global system, $\Delta\mu_{at} + \mu_{DC}$ is adjusted to get the correct number of f electrons. Since the multiplets are well separated by a certain range, $\Delta\mu_{at} + \mu_{DC}$ is still undetermined within this range. Fixing the position of the first (un)occupied peak determines $\Delta\mu_{at} + \mu_{DC}$ univocally.

Fully localized limit Additional parameters, as are needed for the fixed peak double counting, are not really appreciated if one wants to predict quantities *ab initio* as possible. In that case one could use the fully localized limit (FLL) to approximate the double counting. In the fully localized limit, the double counting energy is given by

$$E_{DC} = \frac{1}{2}UN(N-1) - J\frac{N}{2}\left(\frac{N}{2} - 1\right) \quad (3.25)$$

where N is the number of correlated electrons as calculated from the local Green's function or the closest integer number to N , which we label N_{at} [34]. The first choice leads however to a conceptual problem when one investigates the self-energy, but also the second choice is not without problems. Let us start with N as the number of f electrons as calculated from the local Green's function. The self-energy in the Hubbard I approximation is the atomic self-energy, and therefore depends on N_{at} , the *integer* amount of electrons that is closest to N . Besides that, it depends on the double counting, which is a function of N in the standard fully localized limit

$$\Sigma^{at}[N_{at}, H_{DC}(N)] \quad (3.26)$$

This integer number N_{at} might differ from N which is generally non-integer (albeit, normally close to the integer N_{at}). In order to make the self-energy internally consistent, one could use the fully localized limit double counting with atomic occupations [34]. For a true Hubbard I system, we must stress that $N \approx N_{at}$, so we are discussing small changes in H_{DC} . However, these small changes may be very important for us. The FLL with N_{at} also leads to some inconsistencies, this time in the Galitskii-Migdal energy. To obtain the energy correction, we compare the eigenvalue energy obtained from DFT

$$\langle \hat{H}_0 \rangle \sim \text{Tr}[\hat{H}_0 \hat{G}_0] \quad (3.27)$$

with the total energy obtained in DMFT

$$\langle \hat{H}_0 + \hat{U} - \hat{H}_{DC} \rangle \sim \text{Tr}[\hat{H}_0 \hat{G}] + \frac{1}{2} \text{Tr}[\hat{\Sigma} \hat{G}] - E_{DC} \quad (3.28)$$

The energy correction added to the DFT energy by the DMFT cycle is:

$$E_{\text{correction}} \sim \text{Tr}[\hat{H}_0 \hat{G}] - \text{Tr}[\hat{H}_0 \hat{G}_0] + \frac{1}{2} \text{Tr}[\hat{\Sigma} \hat{G}] - E_{DC} \quad (3.29)$$

If we now look how the Galitskii-Migdal energy $E_{GM} = \frac{1}{2} \text{Tr}[\hat{\Sigma} \hat{G}]$ changes with N , we see some inconsistencies when comparing how each term scales. These inconsistencies arise from the fact that in HIA, the local Green's function and the impurity Green's function do not coincide. The mapping between the Hubbard Model and the SIAM is hence not exact, which in the DMFT equations would be needed. Although the self-energy in the lattice problem and the impurity problem match by construction, the Green's functions do not match. This results in the following scaling (the leading order Hartree term) of the different terms and in particular in the inconsistency in the scaling of the term $E_{GM} - E_{DC}$:

FLL	$\hat{\Sigma}$	\hat{G}	E_{GM}	E_{DC}	$E_{GM} - E_{DC}$
N	$\hat{\Sigma}_{at}[N_{at}, H_{DC}[N]]$ $\sim U N_{at}$	$\hat{G}[N]$ $\sim N$	$\frac{1}{2} \text{Tr}[\hat{\Sigma} \hat{G}]$ $\sim U N_{at} N$	$E_{DC}[N]$ $\sim U N^2$	$\frac{1}{2} \text{Tr}[\hat{\Sigma} \hat{G}] - E_{DC}[N]$ $\sim U(N_{at} N - N^2)$
N_{at}	$\hat{\Sigma}_{at}[N_{at}, H_{DC}[N_{at}]]$ $\sim U N_{at}$	$\hat{G}[N]$ $\sim N$	$\frac{1}{2} \text{Tr}[\hat{\Sigma} \hat{G}]$ $\sim U N_{at} N$	$E_{DC}[N_{at}]$ $\sim U N_{at}^2$	$\frac{1}{2} \text{Tr}[\hat{\Sigma} \hat{G}] - E_{DC}[N_{at}]$ $\sim U(N_{at} N - N_{at}^2)$

In both cases, $\text{Tr}[\hat{\Sigma} \hat{G}] \sim U N_{at} N$, whereas the double counting energy that is subtracted scales with $E_{DC} \sim U N^2$ or $E_{DC} \sim U N_{at}^2$. If the hybridization is small $\Delta \approx 0$, then $N \approx N_{at}$ and the error induced by the difference between N and N_{at} is small. Usually it is also small compared to the energy difference induced by the change in electron density. However for the lanthanides, with only a few bonding electrons, the strength of the bonding is small and the energy difference induced by the change in electron density is very small. Therefore the error in the energy correction becomes important. To reduce the error we propose to use the following double counting energy:

$$E_{DC} = \frac{1}{2} U N (N_{at} - 1) - J \frac{N}{2} \left(\frac{N_{at}}{2} - 1 \right) \quad (3.30)$$

This double counting correction we used to calculate the cohesive properties as presented in Paper I and in Sec. 6.1. Another solution to the scaling problem would be to evaluate $\text{Tr}[\hat{\Sigma}_{at} \hat{G}_{at}]$ instead of $\text{Tr}[\hat{\Sigma}_{at} \hat{G}]$. In the former trace both quantities scale with N_{at} . In that case the fully localized limit with atomic occupations would be a very good double counting. We are planning to implement this in our method in the future. However at the moment, for a generic Σ , we usually evaluate $\text{Tr}[\hat{\Sigma}_{imp} \hat{G}_{imp}] = \text{Tr}[\hat{\Sigma} \hat{G}]$, which means $\text{Tr}[\hat{\Sigma}_{at} \hat{G}]$ for the HIA solver. This is an inheritance of the code which was written to be able to use various solvers.

Magnetic cases For the magnetic properties, the double counting issue is complicated for another reason. There are two different options for the Hubbard I approximation in the spin-polarized case: 1. Spin-polarized DFT (LSDA) + U , 2. Non spin-polarized DFT (LDA) + U . If one combines spin-polarized DFT with the Hubbard I approximation, it is less clear how to find a good double counting correction. The double counting term should correct for the f - f exchange that is taken into account in the DFT part and again in the U -tensor. However it should not correct for the f - d exchange, since this is not taken into account for by the U -tensor. The problem is that one can not disentangle the two. To keep the method as clear as possible, we decided to combine non-spin-polarized DFT with the Hubbard I approximation. We start from a non spin-polarized density calculated with DFT and add a small field to break the symmetry in the same time as we add the U -tensor. This results in an (almost) non spin-polarized bare Green's function $G_0^{at\uparrow} \simeq G_0^{at\downarrow}$ (Eq. 6 in Fig. 3.4), but in a spin-polarized self-energy $\Sigma_{\text{imp}}^{\uparrow} \neq \Sigma_{\text{imp}}^{\downarrow}$ (Eq. 7,8 in Fig. 3.4). This produces a spin-polarized double counting potential, which would have to be subtracted from the non spin-polarized Hamiltonian in the LDA part (Eq. 3 in Fig. 3.4). Since one wants to subtract those correlation effects that are included in both the LDA Hamiltonian (non spin-polarized) and in U (spin-polarized), one wants to subtract a spin independent double counting. Therefore the double counting potential is set to the average over the two spin channels:

$$V_{DC}^{\sigma} = \frac{V_{DC}^{\uparrow} + V_{DC}^{\downarrow}}{2} \quad (3.31)$$

in which V_{DC}^{σ} can be calculated in for example the fully localized limit, where the occupation number is now spin dependent.

Chapter 4

RSPt-code and LMTOs

The code that has been used in this licentiate thesis is called *Relativistic Spin-Polarized test* (RSPt) and is based on a Full-Potential Linear Muffin-Tin Orbital (FP-LMTO) method [38]. This method provides a compact, but very accurate basis set, where the orbitals are constructed to adapt to the crystal structure under consideration. In the following sections we will explain the basic concepts of LMTOs, and the parameters that are involved. These sections do not have the aim of containing a complete description of the electronic structure code RSPt nor of the basis generation in the LMTO method. They are merely aimed at providing enough background to understand the basis optimization done in Sec. 5.1. In that section we will illustrate how to optimize the basis for describing the rare earths, in order to obtain a set which is light but sufficiently complete. It is going to be particularly important to reach a sufficient accuracy while limiting the computational effort. A more elaborate explanation of different basis sets in electronic structure codes can be found in Ref. [29]. More details on the FP-LMTO basis of RSPt specifically can be found in Refs. [38, 37, 10, 4]. In this chapter I mainly follow the approach of Torbjörn Björkman in Ref [4].

The LMTO method is based on two main concepts, i.e. the construction of the Muffin-Tin Orbitals (MTOs) and the idea of linearization. The strong point of the MTOs is that they are constructed to optimally describe the region close to the nucleus, while keeping a reasonable description far away from them. This is done by using free electron solutions in radial coordinates that are augmented with solutions to the Schrödinger equation with a spherical potential close to the nuclei. The advantage of introducing the linearization with respect to the energy is that the computational effort is reduced significantly, while keeping a sufficient completeness of the basis.



Figure 4.1: muffin-tin mold. The division of the space in LMTO resembles a muffin-tin mold, i.e. a spherical potential around the atoms (the cake mold) and a constant potential in between the atoms (in between the cakes the mold is flat). In LMTO-ASA this is actually the form of the potential. In FP-LMTO it is merely a geometrical separation that is used to construct the basis functions. Thanks to my friend Laura there is even something tasty inside the mold.

4.1 Symbols

In the construction of the basis functions, a lot of symbols and functions are needed. Some modified versions of the spherical harmonics $Y_{lm}(\hat{\mathbf{r}})$ will be used:

$$\mathcal{Y}_{lm}(\hat{\mathbf{r}}) = i^l Y_{lm}(\hat{\mathbf{r}}) \quad (4.1)$$

$$C_{lm}(\hat{\mathbf{r}}) = \sqrt{\frac{4\pi}{2l+1}} Y_{lm}(\hat{\mathbf{r}}) \quad (4.2)$$

$$\mathcal{C}_{lm}(\hat{\mathbf{r}}) = i^l \sqrt{\frac{4\pi}{2l+1}} Y_{lm}(\hat{\mathbf{r}}) \quad (4.3)$$

where $\hat{\mathbf{r}}$ denotes the angular variable usually denoted by θ and ϕ . For symmetry reasons, not explained here, it is useful to introduce the operator $\mathcal{D}_{\boldsymbol{\tau}}(\hat{\mathbf{r}})$ that brings $\hat{\mathbf{r}}$ to the local coordinate system centered at site $\boldsymbol{\tau}$.

4.2 LMTO Basis

In the construction of the LMTOs, the geometry of the problems at hand, that is a certain arrangement of atoms, is taken into account. The space is divided into two qualitatively different regions. In a sphere around the atom, the potential is dominated by the spherically symmetric Coulomb potential of the nucleus. In the region between these atomic spheres, the Coulomb potential is screened and the remaining potential is nearly constant. The space is therefore divided into spheres around the atom (muffin-tin spheres), and an interstitial region between the spheres. The name Muffin-Tin Orbitals arises from how a spherical potential inside the atomic spheres and the constant potential in between the atomic spheres would look like. This reminds us of the, although only two dimensional, muffin-tin mold (Fig. 4.1), which is used to bake muffins or cupcakes.

To construct the basis functions, the solutions $\phi_l(r, \epsilon_\nu)$ of the radial Schrödinger equation with the spherical average of the Kohn-Sham potential at a certain energy ϵ_ν are used inside the spheres. Here l denotes the orbital angular quantum number. In the interstitial the potential is almost constant and therefore free electron solutions

are a natural choice. The solutions of the radial Schrödinger equation with a constant potential at quantum number κ^2 , are

$$N_{lm}(\kappa, \mathbf{r}) = n_l(\kappa \mathbf{r}) \mathcal{Y}_{lm}(\hat{\mathbf{r}}) \quad (4.4)$$

$$J_{lm}(\kappa, \mathbf{r}) = j_l(\kappa \mathbf{r}) \mathcal{Y}_{lm}(\hat{\mathbf{r}}) \quad (4.5)$$

where j_l are the spherical Bessel and n_l the spherical Neumann functions.

Note that in FP-LMTO no geometric approximations to the shape of the potential are made. However the basis functions are very similar to LMTO in the atomic sphere approximation (ASA) and a similar partitioning of space into spheres and an interstitial region is made.

4.2.1 Basis in the interstitial

The basis in the interstitial is based on the free electron solutions in radial coordinates

$$\mathcal{K}_{lm}(\kappa, \mathbf{r}) = -\kappa^{l+1} \begin{cases} N_{lm}(\kappa, \mathbf{r}) & \text{if } \kappa^2 > 0 \\ N_{lm}(\kappa, \mathbf{r}) - iJ_{lm}(\kappa \mathbf{r}) & \text{if } \kappa^2 < 0 \end{cases} \quad (4.6)$$

This choice is suggested by the KKR and MTO methods and gives a bounded function. By considering a solid with different atoms in the unit cell, the basis function for $i = \{l, m, \boldsymbol{\tau}, \kappa\}$ can be written as a Bloch sum over the above mentioned \mathcal{K}

$$\psi_i(\mathbf{k}, \mathbf{r}) = \sum_{\mathbf{R}} e^{i\mathbf{k} \cdot \mathbf{R}} \mathcal{K}_{l_i m_i}(\kappa_i, \mathcal{D}_{\boldsymbol{\tau}_i}(\mathbf{r} - \boldsymbol{\tau}_i - \mathbf{R})) \quad (4.7)$$

$$(4.8)$$

where \mathbf{k} is the wave vector and \mathbf{R} are the Bravais lattice vectors. To see how the structure of the solid enters in the basis choice, the equation above is separated into two terms. The first term is centered at reference Bravais lattice vector $\mathbf{R} = 0$. The second term is the summation of all \mathcal{K} centered at other sites. If we now evaluate the basis function originating at $\boldsymbol{\tau}_i$ in the reference frame centered at $\boldsymbol{\tau}$, we get that

$$\psi_i(\mathbf{k}, \mathbf{r})|_{\boldsymbol{\tau}} = \mathcal{K}_{l_i m_i}(\kappa_i, \mathcal{D}_{\boldsymbol{\tau}_i}(\mathbf{r} - \boldsymbol{\tau}_i)) \delta(\boldsymbol{\tau}, \boldsymbol{\tau}_i) \quad (4.9)$$

$$+ \sum_{lm} \mathcal{J}_{lm}(\kappa_i, \mathcal{D}_{\boldsymbol{\tau}}(\mathbf{r} - \boldsymbol{\tau})) B_{lm; l_i m_i}(\kappa_i, \boldsymbol{\tau} - \boldsymbol{\tau}_i, \mathbf{k}) \quad (4.10)$$

where $\mathcal{J}_{lm}(\kappa \mathbf{r}) = \kappa^{-l} J_{lm}(\kappa \mathbf{r})$ and $B_{lm; l_i m_i}(\kappa_i, \boldsymbol{\tau} - \boldsymbol{\tau}_i, \mathbf{k})$ are the structure constants or structure functions. These structure constants contain the information about the structure of the solid.

4.2.2 Basis inside the muffin-tin sphere

The strength of the LMTOs is the augmentation part. If we were to use Bessel and Neumann functions all over the space, we would still need a lot to of them describe the region around the atom reasonably. Instead for the LMTOs the Bessel and Neumann functions inside the muffin-tin sphere are replaced by solutions of the radial Schrödinger equation for a spherical potential at an energy ϵ_ν

$$\left(-\frac{d^2}{dr^2} + \frac{l(l+1)}{r^2} + V_{MT}(r) - \epsilon_\nu \right) r \phi(\epsilon_\nu, r) = 0 \quad (4.11)$$

The basis functions inside the muffin-tin sphere consist of a linear combination of $\phi(\epsilon_\nu, r)$ and its energy derivative $\dot{\phi}(\epsilon_\nu, r) = \left. \frac{\partial \phi(\epsilon, r)}{\partial \epsilon} \right|_{\epsilon=\epsilon_\nu}$ evaluated at ϵ_ν . The coefficients of the linear combination should be chosen such that the basis functions inside and outside the muffin-tin sphere match in value and radial derivative across the sphere boundary. This matching results in a basis function $\psi_i(\mathbf{k}, \mathbf{r})$ consisting of two parts. There is a contribution originating from the parent site $\boldsymbol{\tau}_i$ itself plus a sum of structure functions, that take into account the structure of the solid. In a very short notation, we can write the basis functions as

$$\psi_i(\mathbf{k}, \mathbf{r})|_{\mathbf{r}\boldsymbol{\tau}} = \sum_{lm} U_{t;lm}(\epsilon_i, \mathcal{D}_{\boldsymbol{\tau}} \mathbf{r}_t) \Omega_{tl}(\epsilon_i, \kappa_i) \mathbf{S}_{lm;l_i m_i}(\kappa_i, \boldsymbol{\tau} - \boldsymbol{\tau}_i, \mathbf{k}) \quad (4.12)$$

where t indexes all sites $\boldsymbol{\tau}$ with the same symmetry and

$$U_{lm}(\epsilon_i, \mathbf{r}) = (\phi_{lm}(\epsilon_i, \mathbf{r}), \dot{\phi}_{lm}(\epsilon_i, \mathbf{r})) \quad (4.13)$$

$$\mathbf{S}_{lm;l'm'}(\kappa, \boldsymbol{\tau} - \boldsymbol{\tau}', \mathbf{k}) = \begin{pmatrix} \delta(\boldsymbol{\tau}, \boldsymbol{\tau}') \delta(l, l') \delta(m, m') \\ B_{lm;l'm'}(\kappa, \boldsymbol{\tau} - \boldsymbol{\tau}', \mathbf{k}) \end{pmatrix} \quad (4.14)$$

$$\Omega_{tl}(\epsilon_i, \kappa_i) \text{ is the matrix ensuring the correct matching conditions.} \quad (4.15)$$

Note that the tails depend on the quantum number κ^2 , which is called the tail energy, while the heads of the LMTOs depend on ϵ_ν . This linearization energy ϵ_ν is the energy at which the Schrödinger equation, Eq. 4.11, for a spherical potential is solved. These two values are usually treated as independent parameters and should be chosen wisely to increase the LMTO precision.

4.3 Multiple linearization energies

A problem of the LMTOs in their original formulation, is the description of the interstitial. With a single, energy dependent tail, the interstitial region is not very accurately described. Especially for non-close-packed structures this is a problem. In LMTO-ASA one solves this problem by using large overlapping spheres and thereby eliminating the interstitial region. In the full-potential case, this is not possible. Therefore one should find a way to refine the description of the interstitial. A way to do this is to use multiple tails with different κ extending outside the sphere attached to one $\phi_l, \dot{\phi}_l$ combination. This is exactly the strategy followed by RSpt.

Moreover, for some elements, the basis needs to describe states with the same l , but different n . In the rare earths for example, the $5s$ and $5p$ states are hybridizing (especially under compression) and form bands, as well as the $6s, 6p$ and $5d$ states. For $l = 0$ and $l = 1$ we have both $n = 5$ and $n = 6$. Including basis functions with the same l but different n may be very tricky in LMTO, especially when the corresponding bands start to overlap. To describe this properly, in RSpt all basis functions are included in one fully hybridizing basis set and the linearization energies are depending on l and n . To avoid mixing of the semi-core states (e.g. $5s$ and $5p$) with the valence (e.g. $6s$ and $6p$), the linearization energies should be chosen appropriately. A procedure to do this is to impose for both n (e.g. $5s$ and $6s$) the same logarithmic derivative, but fixing the wave function for $n + 1$ to have one node more than for n . In this way the core states are orthogonal to the valence states and there is no risk of mixing and obtaining an unphysical basis.

4.4 Parameters

In this section we will highlight some parameters in the basis set that are not very obvious to choose. Although these parameters are common in all LMTO codes, the following analysis will focus on the RSPt implementation.

Muffin-tin radius: The muffin-tin radii are variational parameters. To obtain the best value, they should be varied such as to minimize the energy. However, for a good basis set, the size of the muffin-tin radius should not matter too much. In fact, we will analyze this issue in our optimization of the basis set, in Sec. 5.1.3.

Angular momentum parameters: The angular momentum parameters, i.e. the set of l needed for a calculation, are chosen to include the atomic l from which the crystal orbitals are arising. In the case of different n this includes also the choice of n . Which n and up to which l we should include among the basis functions, has to be decided case by case. We always include basis functions for those (n, l) corresponding to the parent atomic states, which form hybridizing bands in the crystal phase. In LMTO methods it is not as trivial as in plane wave methods to converge the electron density with respect to the size of the basis. We discuss this convergence issue for the lanthanides in Sec. 5.1.2 and Sec. 5.1.3.

Tail energy: The tail energy (or energies) κ^2 is an other variational parameter of the basis set. The simplest choice would be to set κ to zero and this is already remarkably successful, especially for close packed solids. A finite κ is only needed to represent variations of the wave function in the interstitial region. To successfully describe the interstitial region, several tails with different κ can be attached to the function inside the sphere. The choice of the tail energies κ^2 is not straight forward at all and different schemes have been proposed. The default setup of RSPt is a set of three κ^2 . The highest value represents approximately the average kinetic energy in the interstitial. The lowest value is chosen such that it can represent the energy of the semi-core states (the states that are deep in energy, but still hybridizing). The third value is intermediate to these two extremes, and ensures enough flexibility of the basis set. In Sec. 5.1.3 we will discuss how the default choice of tail energies performs with respect to other possible choices.

Linearization energy: The linearization energies ϵ_ν are chosen for each n and l . They can be chosen in several ways. The most natural choice, e.g. setting the linearization energy to the center of the band, gives a good approximation of $\phi_l(\epsilon, r)$. Other options are for example to set ϵ_ν to the bottom of the band, to the average kinetic energy of the interstitial or to zero. A commonly used option for (n, l) in the case that $(n - 1, l)$ is also included, is to chose the linearization energy such that the function for n is orthogonalized to the function with the same angular momentum quantum number but $n - 1$. This increases the flexibility of the basis and helps avoiding the problem of linear dependencies in the eigenvalue problem, as mentioned above.

Chapter 5

Computational details

In this chapter we take a closer look at the computational setup for our calculations on the RE series. We investigate different aspects of the basis in Sec. 5.1. The effects and the importance of charge self-consistent calculations versus single shot calculations are presented in Sec. 5.2.

5.1 Choice of basis for the rare earths

In this section we investigate the different aspects of the basis, e.g. the number of basis functions, the tail energies, and the linearization energies, for the lanthanides. We investigate the basis when treating the $4f$ electrons as core electrons or as valence electrons. With $4f$ as core electrons, we mainly focus on increasing the basis until the properties under investigation do not change anymore (Sec. 5.1.2). Unlike for plane wave methods, for LMTO methods there is no straight forward way to increase the basis until this convergence is reached. The difficulties arise mainly due to the vast amount of possibilities when choosing the amount of tails and their tail energies. From the results we try to develop a physical intuition for finding the right basis when simulating the rare earths with the $4f$ as valence electrons. These simulations are important, since they are the starting point for the Hubbard I calculations.

In the lanthanide series, the spin-orbit coupling is important and has to be included in the calculations. Since in our code spin-orbit coupling is taken into account only inside the muffin-tin spheres, one has to choose their size wisely. Without spin-orbit coupling, the muffin-tin radius could be treated as a variational parameter, where the optimal choice minimizes the energy. When including spin-orbit coupling, however, the Hamiltonian depends on the muffin-tin radius. Therefore it is not a variational parameter any longer. Instead we have to choose the muffin-tin radius as big as possible in order to have the most complete and realistic Hamiltonian. We also have to choose it constant across different volumes [38], since we do not want to vary the amount of spin-orbit coupling that we include in our calculations. However, the choice of a constant muffin-tin radius also means that the size of the interstitial region varies. Hence, it is important to describe the interstitial region well, in order not to pile up errors. Therefore we need a basis that is flexible enough to adjust inside big and small interstitial regions and there should be a minimal dependence on the choice of the muffin-tin radius. Finding such a basis will be the main focus of Sec. 5.1.3. But first, we will start with developing a good notation to specify the basis set one intends to use in a given RSPt calculation.

The following sections will be rather technical and mainly interesting for people who use RSPt or similar codes on similar systems.

5.1.1 Notation

The following sections will contain comparisons between different basis sets. To make reading as easy as possible, we will denote the basis as follows. We start with the highest principle quantum number n and the lowest angular momentum quantum number l and move first towards higher l and after that towards lower n . For RSPt this a logical order since basis functions with the same l but different n can not be in the same energy set, e.g. they have a different linearization energy. By default the energy sets are ordered from high n towards lower n from top to bottom and from low l to high l from left to right. For each energy set, each n and each l we denote:

$$\text{number-of-tails}^{\text{set-of-tails: list-of-used-tails}}(nl^{\text{linearization-energy-flag}})$$

where one has to provide a separate list of the tail energies κ^2 and the associated parameters contained in “set-of-tails”. As an example we explain our first basis:

$$3^{\alpha:1,2,3}(6s^{20}6p^{21})2^{\alpha:1,2}(5d^04f^{-1}) \quad 2^{\alpha:1,2}(5s^{-1}5p^{-1})0(5d^04f^{-1})$$

The $6s$ and $6p$ electrons in energy set 1 are described by three tails (namely tails 1,2 and 3) coming from the tail set α (the exact form will be given below). Their linearization energy flags are 20 and 21 respectively, which means that they are orthogonalized to the $5s$ and $5p$ states of the second energy set. The $5d$ and $4f$ basis functions are described with tails 1 and 2 from, of course, the same tail energy set α . Their linearization energy flags are set to 0 (linearization energy determined by an internal algorithm) and -1 (linearization energy set to the center of the band) respectively. Higher l are not included in the basis for this energy set, and the linearization flags of all higher l are set to 0. Due to the multiple tails in RSPt, it is hardly needed to include basis functions with higher l than the parent atomic functions. After the $4f$ basis functions we move to the second tail energy set and start again with the lowest l . The $5s$ and $5p$ semi-core electrons are described with two tails (1 and 2) and their linearization energy is set to the center of the band (flag -1). The $5d$'s and $4f$'s are not explicitly described as basis functions in the second energy set, but their linearization flags matter. This is because the linearization energy enters through the expansion in Eq. 4.10. To denote that the $5d$'s and $4f$'s are not explicitly included in the basis, they are denoted as described by 0 tails, but their linearization energy flags are specified. The tail set α has defined 3 tails, with tail energies $\kappa_{\text{tail } 1}^2 = 0.3$ Ry, $\kappa_{\text{tail } 2}^2 = -2.3$ Ry and $\kappa_{\text{tail } 3}^2 = -1.5$ Ry. Other possible choices are discussed below. In Fig. 5.1 the density of states for one of the REs is plotted, together with the value of the tail energies of set α . The position of the semi-core states and the valence band give an indication on how to choose the tail energies. In App. C a quick look-up table for all the numbers and symbols in the basis notation is given.

5.1.2 Basis with $4f$ in the core

In the standard model of the lanthanides, the $4f$ electrons are assumed not to hybridize with the valence electrons. One possible implementation of this standard model is to treat the $4f$ electrons as core electrons, effectively forbidding all hybridization. This

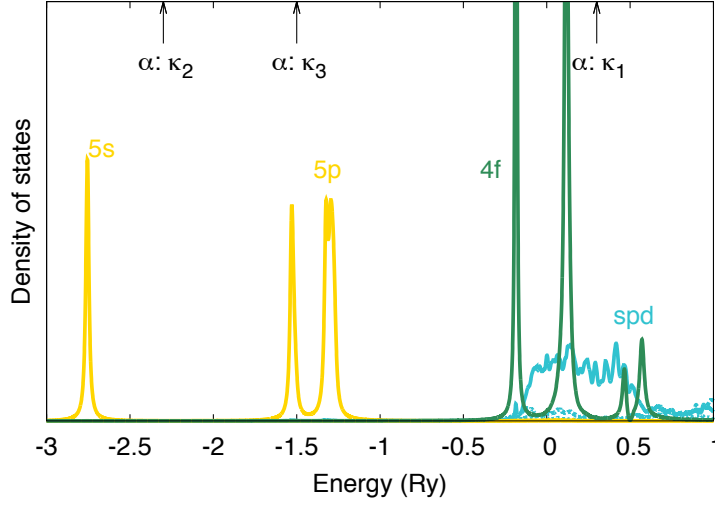


Figure 5.1: Density of states of one of the REs. The position of the semi-core and valence states can give a guideline on how to choose the tail energies. The $4f$ multiplets, as obtained in HIA, are displayed on top of the $[spd]$ band.

also implies that the $4f$ states are *not* included in the construction of the basis for the valence electrons.

Using the $4f$ in the core approach, we constructed some different bases, trying to increase the flexibility and to converge it with respect to the amount of basis functions. All tested bases have a so called semi-core to describe the $5s$ and $5p$ states. These states are almost fully occupied and lay at relatively deep energies, but also form bands, to a certain extent, see Fig 5.1 for a typical density of states of a RE. Describing these states is very important as they participate in binding under compression. As mentioned above, in RSPt one can describe these semi-core states by means of an additional linearization energy set. The valence $[6s6p5d]$ states are described with other linearization energies and for some bases a third linearization energy set is added to increase the flexibility. We tried to converge the energy versus volume curve with respect to the basis in a systematic way. We started from one of the default setups of RSPt and included a third linearization energy set, containing the $7s$ and $7p$ basis functions. On top of that we added $6d$, $6f$, $5g$ and/or $6h$ to this set. These tests were performed with tail energies different from those specified above. This tail energy set, which we denote as γ , contains $\kappa_{\text{tail } 1}^2 = 0.3$ Ry, $\kappa_{\text{tail } 2}^2 = -2.3$ Ry and $\kappa_{\text{tail } 3}^2 = -0.6$ Ry.

We report on the convergence of an illustrative example, i.e. the energy versus volume curves for hcp Pr, as calculated by means of 5 different choices of the RSPt basis set, in Fig. 5.2. The calculated points were fitted with the Birch-Murnaghan [3] equation of state to obtain the equilibrium volume and bulk modulus. For a large enough basis (the bottom three lines in the figure), the equilibrium volumes do not change more than 0.01

\AA^3 and the total energies differ only by less than a mRy. These and other tests clearly show that a good description of the electron density requires two groups of states with f character. If $4f$ electrons are included in the core, this means that the valence will contain both $5f$ and $6f$ states.

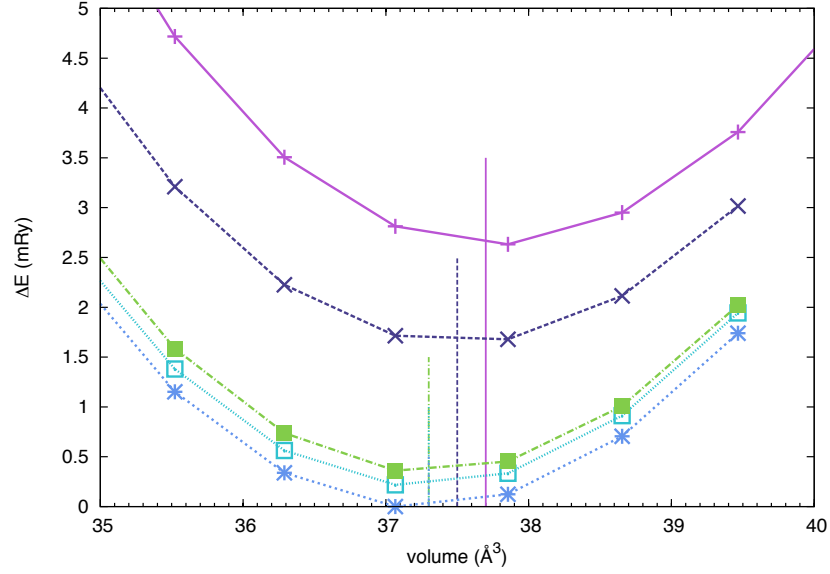


Figure 5.2: Energy versus volume curve for Pr calculated with a GGA functional treating the $4f$ electrons as core electrons. The different bases used are

purple	$= 3\gamma^{1,2,3}(6s^{20}6p^{21})2\gamma^{1,2}(5d^{-1}5f^{-1})$	$2\gamma^{1,2}(5s^{-1}5p^{-1})0(5d^05f^{-1})$
dark blue	$= 2\gamma^{1,2}(7s^{20}7p^{21}6d^{22})0(6f^{23})2\gamma^{1,2}(5g^{-1})$	
	$3\gamma^{1,2,3}(6s^{20}6p^{21})2\gamma^{1,2}(5d^{-1}5f^{-1})$	$2\gamma^{1,2}(5s^{-1}5p^{-1})0(5d^05f^{-1})$
cornflower	$= 2\gamma^{1,2}(7s^{20}7p^{21}6d^{22}6f^{23}5g^06h^0)$	
	$3\gamma^{1,2,3}(6s^{20}6p^{21})2\gamma^{1,2}(5d^05f^{-1})$	$2\gamma^{1,2}(5s^{-1}5p^{-1})0(5d^05f^{-1})$
light blue	$= 2\gamma^{1,2}(7s^{20}7p^{21}6d^{22}6f^{23}5g^0)$	
	$3\gamma^{1,2,3}(6s^{20}6p^{21})2\gamma^{1,2}(5d^05f^{-1})$	$2\gamma^{1,2}(5s^{-1}5p^{-1})0(5d^05f^{-1})$
bright green	$= 2\gamma^{1,2}(7s^{20}7p^{21})0(6d^{22})2\gamma^{1,2}(6f^{23}5g^{-1})$	
	$3\gamma^{1,2,3}(6s^{20}6p^{21})2\gamma^{1,2}(5d^{-1}5f^{-1})$	$2\gamma^{1,2}(5s^{-1}5p^{-1})0(5d^05f^{-1})$

The vertical lines denote the equilibrium volume for the curve with the same color. The differences in energy are taken with respect to the lowest calculated point of all curves.

5.1.3 Basis with $4f$ in the valence

As stated before, the naive LDA calculations, with the $4f$ states described as hybridizing valence electrons, give poor results when compared to experiment. However it is impor-

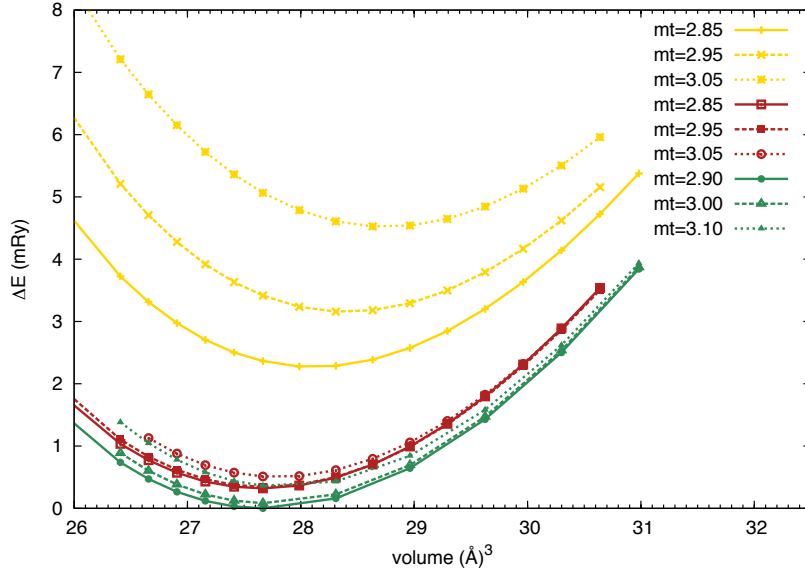


Figure 5.3: Energy versus volume curve for Tm calculated with an LDA functional with the $4f$ electrons treated as valence electrons and *without* spin-orbit coupling. The three colors denote three different bases:

$$\begin{aligned}
 \text{yellow} &= 3^{\alpha:1,2,3}(6s^{20}6p^{21}) \ 2^{\alpha:1,2}(5d^04f^{-1}) \quad 2^{\alpha:1,2}(5s^{-1}5p^{-1}) \ 0(5d^05f^{-1}) \\
 \text{red} &= 3^{\alpha:1,2,3}(6s^{20}6p^{21}) \ 2^{\alpha:1,2}(5d^04f^{-1}) \quad 2^{\alpha:1,2}(5s^{-1}5p^{-1}) \ 0(5d^0) \ 2^{\alpha:1,2}(5f^{-1}) \\
 \text{green} &= 3^{\beta:1,2,3}(6s^{20}6p^{21}5d^0) \ 3^{\beta:1,2,4}(4f^{-1}) \quad 2^{\beta:1,2}(5s^{-1}5p^{-1}) \ 0(5d^0) \ 3^{\beta:1,2,4}(5f^{-1})
 \end{aligned}$$

The tail energy set α has $\kappa_{\text{tail } 1}^2 = 0.3$ Ry, $\kappa_{\text{tail } 2}^2 = -2.3$ Ry and $\kappa_{\text{tail } 3}^2 = -1.5$ Ry and tail energy set β has $\kappa_{\text{tail } 1}^2 = 0.25$ Ry, $\kappa_{\text{tail } 2}^2 = -2.3$ Ry, $\kappa_{\text{tail } 3}^2 = -1.0$ Ry and $\kappa_{\text{tail } 4}^2 = -0.2$ Ry. The different line types (solid, dashed, dotted) belong to different muffin-tin radii, as denoted in the legend in a.u. The differences in energy are taken with respect to the lowest calculated point of all curves.

tant to investigate when the basis is converged, since this basis enters in the Hubbard I calculations. For the Hubbard I calculation it is important to keep our basis as compact as possible, but flexible enough to describe the energy versus volume curve properly. For reasons explained above, including spin-orbit coupling requires a muffin-tin radius which is as big as possible. Moreover this sphere should be kept constant over different lattice parameters, which requires a flexible basis, especially in the interstitial region.

Extending the basis: In Fig. 5.3 we reported the energy versus volume curve for three different bases for Tm. We deliberately *excluded* spin-orbit coupling, so that we are sure that changes in the curves are not due to spin-orbit coupling. This is of course wrong to get the correct physics of this system, but is the best possible test to analyze the flexibility of the basis. We started from the default basis setup of RSPt, describing the s and p valence states with 3 tails, the other valence states as well as the semi-core states with only two tails. By using the set of tails α , as specified in Sec. 5.1.1, this basis

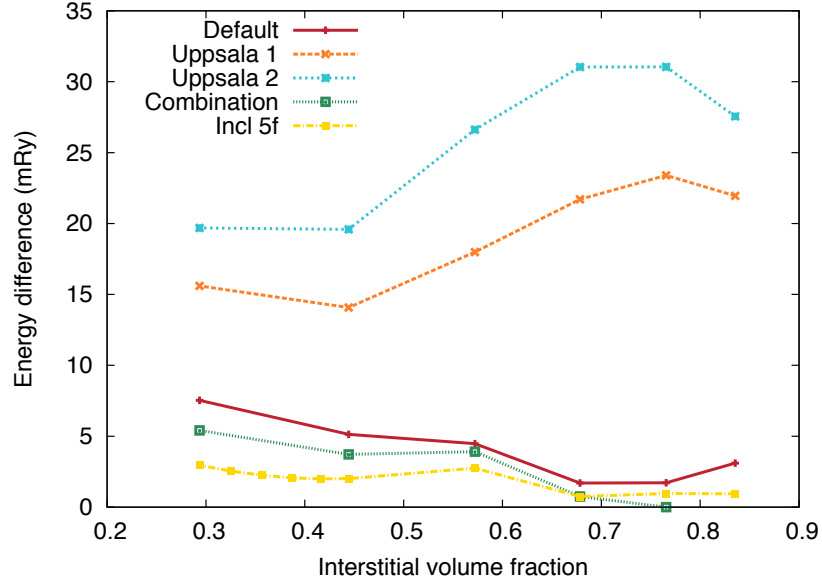


Figure 5.4: Energy depending on the interstitial volume fraction for Tm. The different bases are described in the text and are analogous to the bases tested in Ref. [4] for Pb. The differences in energy are taken with respect to the lowest calculated point of all curves.

can be described as

$$3^{\alpha:1,2,3}(6s^{20}6p^{21})2^{\alpha:1,2}(5d^04f^{-1}) \quad 2^{\alpha:1,2}(5s^{-1}5p^{-1})0(5d^05f^{-1}),$$

One can notice from the yellow lines in Fig. 5.3 that this simple basis leads to an energy curve that highly depends on the muffin-tin radius. We infer that the basis is not sufficiently flexible to describe the interstitial region well enough. Therefore we included some $5f$ basis functions in the second energy set. This is analogous to including a $6f$ basis function when we treated the $4f$'s as core, as was done in the previous section. Adding a $6f$ basis function made the curve much less dependent on the muffin-tin radius, as shown by the red curves in Fig. 5.3. Further expansion of the basis, by adding more tails for the $4f$ and $5f$ or changing the tail energies, does not improve on the dependence of the curves on the muffin-tin size, but lowers the total energy a bit. This is illustrated by the green curves in Fig. 5.3.

Both Figs. 5.2 and 5.3 emphasize how important it is to include extra f 's in the basis. If the $4f$'s are treated as core electrons, $5f$ functions are by default included in the basis. The results in Fig. 5.2 and other calculations show that it is important to also include $6f$ functions in the basis. If the $4f$'s are treated in the valence it is needed to include also one higher principle quantum number for f . Hence the $5f$ functions need to be included in the basis, as can be seen from Fig. 5.3.

Tail energies: The choice of the tail energies κ^2 is not straight forward and different schemes have been developed and tested. In Ref. [4] different schemes for choosing the tail energies have been tested for fcc Pb. We tested similar choices for Tm by still focusing on the model with $4f$ in the valence. If the basis is sufficiently complete inside as well as outside the muffin-tin sphere, the size of the muffin-tin radius should not influence the total energy significantly. We therefore plotted the energy for different muffin-tin radii or different fractions of the interstitial volume $V_{\text{interstitial}}/V_{\text{total}}$. The tail energy schemes tested in Ref. [4] where the following:

Default: the default setup of RSPT. This setup attaches three tails to the valence s and p states and 2 tails to the semi-core ($5s$ and $5p$) states and to the other valence states ($5d$ and $4f$). The precise form of all basis setups will be explained below.

Uppsala setup: The highest tail energy is set to $\kappa^2 = -0.1$ Ry and the lowest is set to the difference between the lowest semi-core eigenvalue and the Fermi level. Two other tails are distributed evenly between these two tails. The two lowest tails are used for the semi-core states and the two highest tails are used for the other valence orbitals. Having only negative tails make the simulations more stable (no oscillatory functions are included), but variationally less powerful.

Combination: This setup combines the good points of the Uppsala setup and the default setup.

A more detailed description of these setups, including their motivation, is given by Torbjörn Björkman in Ref. [4]. It is interesting to compare these choices with the result of our previous tests, i.e. the red basis in Fig. 5.3. The latter is denoted with the label “Incl 5f” in Fig. 5.4, since it includes a $5f$ basis function. The precise form of the bases tested in Fig. 5.4 will be described below. The default setup used the tail energy set γ described in Sec. 5.1.2 and basis functions

$$3^{\gamma:1,2,3}(6s^{20}6p^{21})2^{\gamma:1,2}(5d^04f^{-1}) \quad 2^{\gamma:1,2}(5s^{-1}5p^{-1})0(5d^05f^{-1}) \quad (5.1)$$

For the two Uppsala setups, the tail energies where constructed with the scheme described above. For Uppsala 1, a standard value was taken for the difference of the lowest semi-core eigenvalue and the Fermi level, whereas for Uppsala 2 this value was calculated. This resulted in the following tail energies.

Uppsala 1: $\delta = \{\kappa^2 = -0.1, -0.5, -1.2, -2.3\}$ Ry

Uppsala 2: $\epsilon = \{\kappa^2 = -0.1, -0.96 - 1.82 - 2.68\}$ Ry.

Apart from the tail energies, the basis functions were the same. Uppsala 1:

$$2^{\delta:1,2}(6s^{20}6p^{21}5d^04f^{-1}) \quad 2^{\delta:3,4}(5s^{-1}5p^{-1})0(5d^05f^{-1}) \quad (5.2)$$

Uppsala 2:

$$2^{\epsilon:1,2}(6s^{20}6p^{21}5d^04f^{-1}) \quad 2^{\epsilon:3,4}(5s^{-1}5p^{-1})0(5d^05f^{-1}) \quad (5.3)$$

For the combination of the default and the Uppsala setup, the following tail energy set was used $\zeta = \{\kappa^2 = -0.1, -0.5, -1.2, -2.3, 0.1\}$ Ry, where the last tail (0.1 Ry) was varied such that the tail energy κ^2 was set to the value of the average kinetic energy in the interstitial. The following basis functions were used

$$3^{\zeta:1,2,5}(6s^{20}6p^{21}5d^04f^{-1}) \quad 3^{\zeta:3,4,5}(5s^{-1}5p^{-1})0(5d^05f^{-1}) \quad (5.4)$$

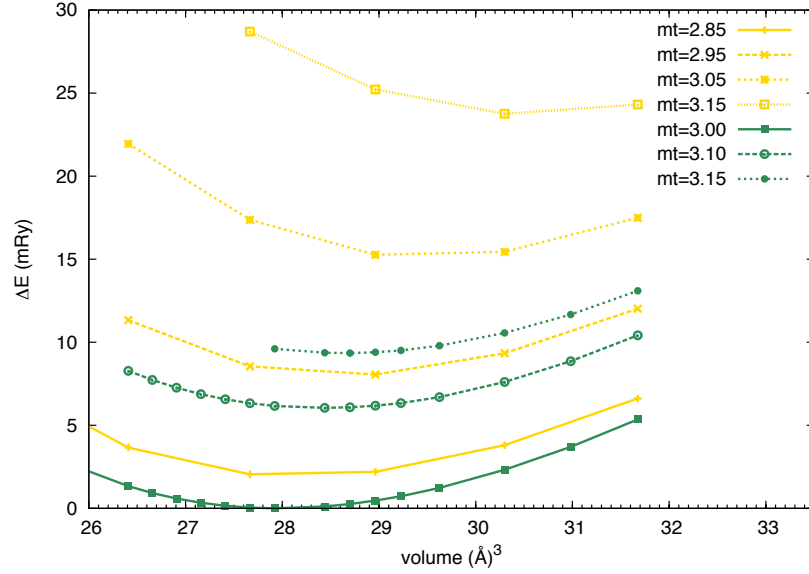


Figure 5.5: Energy versus volume curve for Tm calculated with an LDA functional with the $4f$ electrons treated as valence electrons and *with* spin-orbit coupling. The two colors denote two different bases:

$$\begin{aligned}
 \text{yellow} &= 3^{\alpha:1,2,3}(6s^{20}6p^{21})2^{\alpha:1,2}(5d^04f^{-1}) & 2^{\alpha:1,2}(5s^{-1}5p^{-1})0(5d^05f^{-1}) \\
 \text{dark green} &= 3^{\beta:1,2,3}(6s^{20}6p^{21}5d^0)3^{\beta:1,2,4}(4f^{-1}) & 2^{\beta:1,2}(5s^{-1}5p^{-1})0(5d^0)3^{\beta:1,2,4}(5f^{-1})
 \end{aligned}$$

where tail energy set α has $\kappa_{\text{tail } 1}^2 = 0.3$ Ry, $\kappa_{\text{tail } 2}^2 = -2.3$ Ry and $\kappa_{\text{tail } 3}^2 = -1.5$ Ry and tail energy set β has $\kappa_{\text{tail } 1}^2 = 0.25$ Ry, $\kappa_{\text{tail } 2}^2 = -2.3$ Ry, $\kappa_{\text{tail } 3}^2 = -1.0$ Ry and $\kappa_{\text{tail } 4}^2 = -0.2$ Ry. The different line types (solid, dashed, dotted, ...) belong to different muffin-tin radii, as denoted in the legend in a.u.

The “Incl 5f” basis used the α tail energy set described in Sec. 5.1.1 and basis functions

$$3^{\alpha:1,2,3}(6s^{20}6p^{21})2^{\alpha:1,2}(5d^04f^{-1}) \quad 2^{\alpha:1,2}(5s^{-1}5p^{-1})0(5d^0)2^{\alpha:1,2}(5f^{-1}) \quad (5.5)$$

As can be seen in Fig. 5.4 the default setup, the combination and the setup that includes the $5f$ basis functions perform better than the Uppsala setups for Tm. For small interstitial volume fractions, which we are finally interested in, the basis that includes the $5f$ functions performs best.

We can finally analyze the effects due to the inclusion of spin-orbit coupling. In Fig. 5.5 we show when including spin-orbit coupling, the curves change with different muffin-tin size. For the simple basis (yellow) the differences are due to two effects. The first origin is the poor basis, as it was shown in Fig. 5.3. The second cause is the different amount of spin-orbit coupling taken into account depending on the muffin-tin size. For the extended basis (green) we know now that the differences are mainly due to that the spin-orbit coupling is only taken into account inside the muffin-tin region. The curves differ therefore slightly in energy. However the minimal volume is still quite similar for

the different curves. To describe the physics as correctly as possible, one would like the muffin-tin region to be as big as possible and constant over the different volumes under consideration.

In conclusion we propose that the following basis

$$3^{\alpha:1,2,3}(6s^{20}6p^{21})2^{\alpha:1,2}(5d^04f^{-1}) \quad 2^{\alpha:1,2}(5s^{-1}5p^{-1})0(5d^0)2^{\alpha:1,2}(5f^{-1}) \quad (5.6)$$

offers a good compromise between being sufficiently flexible and still quite small. We used this basis for the calculations on the trivalent rare earths. For the divalent elements it was found to be important to fix the linearization energy of the $5d$ orbitals to the center of the band

$$3^{\alpha:1,2,3}(6s^{20}6p^{21})2^{\alpha:1,2}(5d^{-1}4f^{-1}) \quad 2^{\alpha:1,2}(5s^{-1}5p^{-1})0(5d^{-1})2^{\alpha:1,2}(5f^{-1}) \quad (5.7)$$

Finally we would like to stress that the REs are a particularly difficult case. All the above mentioned optimizations are usually not of great importance, but for the RE they are. Due to the very weak bonding in the REs, the energy versus volume curve is very shallow and minor errors can become important.

5.2 Charge self-consistent versus single shot

In Sec. 3.2.3 we have explained how the Hubbard I calculations are done. In Fig. 3.4 a scheme was sketched to illustrate the various steps to follow. Starting from the Kohn-Sham Hamiltonian and using the atomic self-energy, one finally arrives at the one-electron Green's function (Eq. 9 in Fig. 3.4). The results obtained from this calculation are often referred to as "single shot". One can, however, recalculate the Kohn-Sham potential in the DFT part, taking into account the new electron density modified by the self-energy. When repeating this until the density is converged, this procedure is called a charge self-consistent calculation. In this section we investigate the difference between both methods.

In Figs. 5.6 and 5.7 we display for some of the rare earths the energy versus volume curve for a charge self-consistent calculation and for a single shot calculation. In all cases the single shot calculations results in a higher energy than the charge self-consistent calculations. For the light rare earths, La, Pr and Pm, the results for a charge self-consistent simulation and for a single shot calculation are very similar. The divalent Eu has very different results depending on whether the calculation was done charge self-consistently. The single shot calculation largely overestimates the volume and also the bulk modulus. The latter can be concluded from the fact that $\Delta E_{1sh} \gg \Delta E_{csc}$ on a similar volume range. For the heavy rare earths, Gd, Ho and Tm, the single shot simulation largely underestimates the volume and overestimates the bulk modulus. For Lu, which has a full $4f$ shell the difference is again very small.

To explain the difference between the single shot results and the charge self-consistent results, it is important to look at the starting point of these simulations, e.g. the plain DFT simulation with the $4f$ electrons treated as band like electrons. This band-like treatment results in the $4f$ electrons erroneously participating in the bonding and therefore in a large overestimation of the bonding and hence underestimation of the volume. In the early RE this effect can be clearly seen. In the late RE a second error occurs,

which has the opposite effect. In the late RE, when treating the $4f$ electrons band-like, part of the density with $[spd]$ character is transformed to states with an f character. This results in a decrease of $[spd]$ electrons, which are the main contributors to the bonding. Less bonding leads to a larger volume. Because of these two compensating errors in the late RE, the volume calculated with the $4f$ electrons treated as band-like, is quite close to the actual volume. In Tab. 5.1 the amount of $[spd]$ and f character inside the muffin-tin sphere is displayed, together with the relative volumes, for the DFT simulation and the HIA simulations.

The single shot HIA removes most of the f contribution to the bonding. For the early RE, this results in a slight underestimation of the binding and hence a slight overestimation of the volume after the single shot procedure. Adding HIA self-energy to the potential in a charge self-consistent way improves the description of the $[spd]$ valence electrons and slightly decreases the volume.

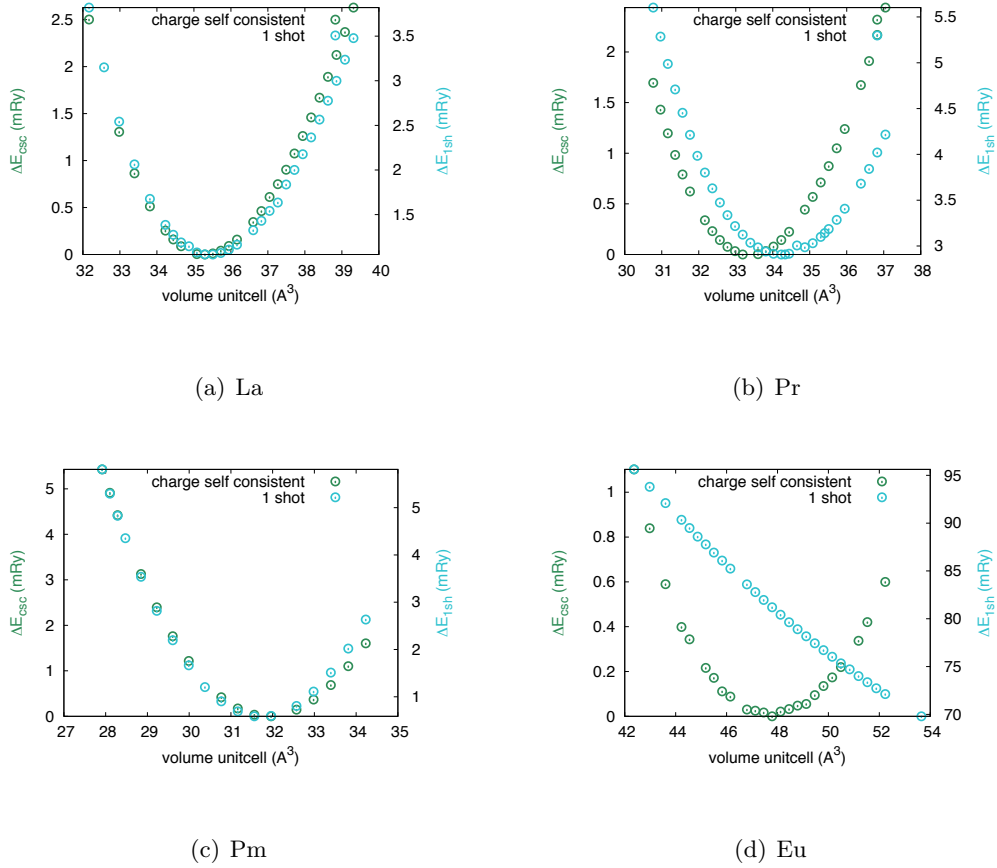


Figure 5.6: The difference in the energy versus volume curve in case of a charge self-consistent calculation (green dots, left axis) and a single shot calculation (blue dots, right axis) for some light rare earths. Note that La has 0 f electrons and the Eu is divalent.

Also note the different axes and their different range especially for Eu.

For the heavy RE, the effect of the removal of the f contribution to the bonding, is counteracted by an other effect. The HIA also seems to restore the correct $4f$ occupation. This gives rise to an increase in $[spd]$ electrons, which results in a drastic increase of the binding. After the single shot HIA, the effect of the increase in $[spd]$ electrons is

much bigger than the effect of the removal of the f electrons. Hence the volume is largely underestimated. Allowing the potential to adjust in a charge self-consistent way improves the description of the $[spd]$ valence electrons. The amount of $[spd]$ character inside the muffin-tin sphere increases, or in other words more of the $[spd]$ density is inside the muffin-tin sphere and less outside. This results in less bonding and hence a larger volume.

Last but not least, we arrive at the middle element Eu, where we find a somewhat unexpected behavior. The plain DFT simulation largely underestimates the volume. This effect arises from the $4f$ contribution to the bonding and the slight overestimation of the $[spd]$ character of the valence electrons. After the single shot HIA procedure, the volume is hugely overestimated. This is due to the removal of the f contribution to the bonding and the erroneous shift of $[spd]$ to f character. The charge self-consistent description improves the description of the $[spd]$ valence electrons. The shift of $[spd]$ to f character is counteracted and the $[spd]$ electrons slightly move from the muffin-tin sphere to the interstitial. Both result in an increase of the bonding, which results in a smaller volume compared to the single shot procedure.

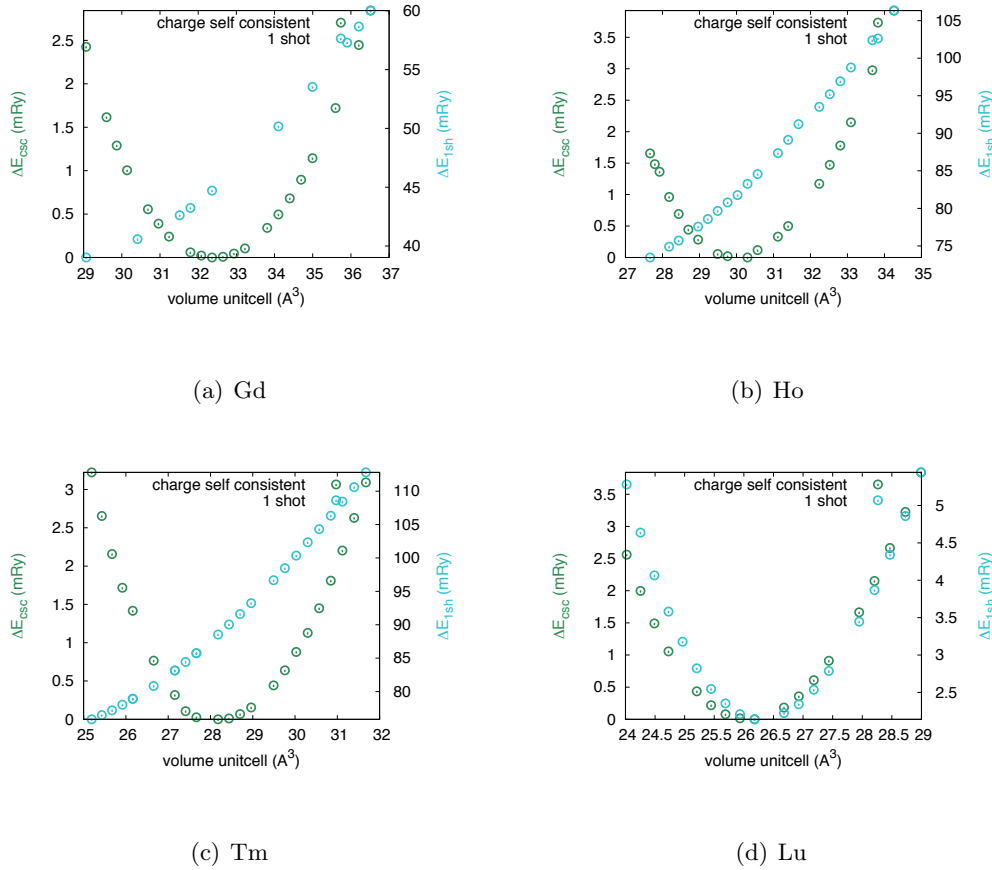


Figure 5.7: The difference in the energy versus volume curve in case of a charge self-consistent calculation (green dots, left axis) and a single shot calculation (blue dots, right axis) for some heavy rare earths. Note that Lu has a completely filled $4f$ -shell. Also note the different axes, with quite different ranges.

Table 5.1: Differences between DFT, HIA single shot (1sh) and HIA charge self-consistent (csc) simulations. The numbers are quite approximate and represent the average of the electrons density projected onto the $[spd]$ or f orbitals inside the muffin-tin sphere. Especially for the $[spd]$ electrons a significant amount will be outside the muffin-tin sphere. The volume is reported to be much ($<<$) or slightly ($<$) smaller, much ($>>$) or slightly ($>$) bigger or equal (\approx) than/to the HIA charge self-consistent volume.

El		$[spd]$ in MT	f	Volume
La	DFT	1.4-1.56	0.1	$<$
	1sh	1.42-1.60	0.1	\approx
	csc	1.43-1.60	0.1	
Pr	DFT	1.34-1.50	2.16	$<<$
	1sh	1.38-1.55	2.13-2.16	$>$
	csc	1.37-1.52	2.14-2.17	
Pm	DFT	1.16-1.39	4.34	$<<$
	1sh	1.31-1.52	4.13-4.16	\approx
	csc	1.32-1.53	4.12-4.16	
Eu	DFT	0.9-1.2	6.55-6.60	$<<$
	1sh	0.8-0.95	7.4	$>>$
	csc	0.7-0.9	7.07	
Gd	DFT	1.01-1.26	7.46-7.47	$<$
	1sh	1.23-1.49	7.07-7.09	$<<$
	csc	1.31-1.63	7.05-7.07	
Ho	DFT	1.00-1.20	10.52-10.56	$>$
	1sh	1.28-1.49	10.03-10.04	$<<$
	csc	1.38-1.65	10.03-10.04	
Tm	DFT	0.9-1.14	12.5-12.55	$>$
	1sh	1.21-1.47	12.0	$<<$
	csc	1.29-1.54	12.01-12.02	
Lu	DFT	1.37-1.58	13.96	$>$
	1sh	1.37-1.57	13.97-13.98	\approx
	csc	1.37-1.57	13.97-13.98	

Chapter 6

Results

This chapter is an extension to the results section presented in Paper I. Instead of repeating the same presentation of our results, we use this chapter to compare our findings to those obtained by other scientists with other methods. It might therefore be useful to first read Paper I and thereafter continue with this chapter. The parameters used in the HIA calculations presented here are the same as those reported in Paper I, unless otherwise specified. In Sec. 6.1 we compare the obtained cohesive properties to the results from A. Delin et al. [9], P. Söderlind et al. [35], P. Strange et al. [36] and S.K. Mohanta et al. [32]. In Sec. 6.2 we compare our results on the magnetic moments to the results from P. Söderlind et al. [35] and S.K. Mohanta et al. [32]. In Sec. 6.3 we compare the photoemission spectra for some different settings and investigate the consequences of the Atomic Sphere Approximation used by S. Lebegue et al. [28, 27].

6.1 Cohesive properties

In Fig. 6.1(e) and 6.2(d) we present our results on the equilibrium volume and bulk modulus for the RE series, calculated within the Hubbard I approximation. We compare these to the calculations by other authors [9, 35, 36, 32] that used different methods than HIA. Here follows a short description of these methods and their results.

A. Delin et al. [9] have calculated the cohesive properties for the RE series, treating the $4f$ electrons as core electrons. In this way the $4f$ electrons can not possibly hybridize, which is compatible with the standard model of the lanthanides. The approximated exchange correlation functionals still describe the $4f$ orbitals not correctly, but since they can not hybridize with the valence electrons, they can not influence the bonding properties. The results of A. Delin et al. from Ref. [9], are reprinted in Figs. 6.1(a) and 6.2(a).

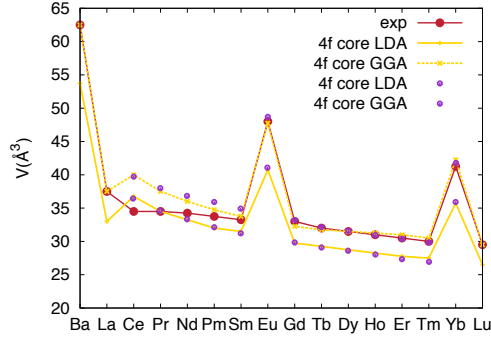
P. Söderlind et al. [35] also calculated the cohesive properties treating the $4f$ electrons as core electrons. The results are reprinted together with the above mentioned calculations of A. Delin in Fig. 6.1(a). However the authors of Ref. [35] mainly considered the $4f$ electrons as band electrons, treating them either as spin-polarized (SP), or spin-polarized including spin-orbit coupling (SO), or even spin-polarized with spin-orbit coupling and orbital polarization (OP). The latter method adds an energy term that is proportional to the square of the orbital moment to the total energy. This takes into account the intra-atomic interactions corresponding to the Hund's rules. The results from Ref. [35] are reprinted in Figs. 6.1(b), 6.1(c) and 6.2(b).

P. Strange et al. [36] calculated the equilibrium volume of the RE series going beyond plain DFT by applying the Self Interaction Correction (SIC). This removes the spurious interaction of an electron with itself, which arises in plain DFT due to that an approximate exchange cannot cancel exactly the unphysical term in $V_{Hartree}$. The volumes calculated by P. Strange et al. [36] are reprinted in Fig. 6.1(d).

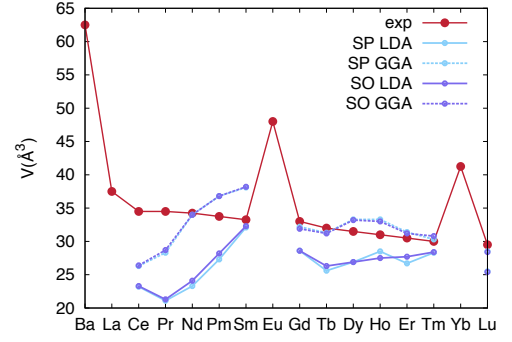
S.K. Mohanta et al. [32] calculated the cohesive properties of the second half of the RE series including correlation effects with the LDA+U scheme. The LDA+U scheme includes a U -term that takes the correlation effects of the localized electrons into account. In the LDA+U scheme only the static Hartree-Fock like interactions are taken into account. The starting Hamiltonian is exactly the same as Eq. 3.7 and the problem is also formally solved via DMFT. However, the SIAM is then solved in the Hartree-Fock approximation, which means that this theory is a mean-field theory for both space and quantum degrees of freedom. The results of S.K. Mohanta et al. [32] are reprinted in Figs. 6.1(d) and 6.2(c).

The results of the above mentioned methods, are displayed for comparison with the Hubbard I approximation. Treating the $4f$ electrons as core electrons (Fig. 6.1(a)) is compatible with the standard model of the lanthanides. The trend in the volume across the series is in agreement with experiment for the heavy REs. However, for the light RE the trend is not so well-captured. This is probably due to some small hybridization of the $4f$'s that is present in the light RE. Also the bulk modulus (Fig. 6.2(a)) is found quite close to experiment. Although this method works very well for the cohesive properties, the spectral properties are not accessible by this method. Treating the $4f$ electrons as band electrons, including either spin-polarization (SP), or spin-polarization and spin-orbit coupling (SO), or even spin-polarization and spin-orbit coupling and orbital polarization (OP) (Figs. 6.1(b) and 6.1(c)) does not quite well capture the trend in the volume across the series. For the light RE the trend is even opposite to the trend in experiment. This is probably because the $4f$ electrons are described band-like, which gives them a very itinerant character and a great contribution to the bonding. Our own tests with the $4f$ as valence electrons (including spin-polarization and spin-orbit coupling) pointed towards two compensating errors for the late REs. On one hand, the treatment of the $4f$ electrons as valence electrons results in a $4f$ contribution to the bonding. On the other hand it results in a decrease in the amount of $5d$ character of the valence band (compensated by an increase in the amount of $4f$ character). This decrease in the strongly binding d electrons results in a decrease of the bonding. These two compensating errors might be the reason why the trend in the volume across the heavy REs is not that bad. The SIC method (Fig. 6.1(d)) seems to reproduce the trend in the volume across the series, although it is strictly speaking not completely compatible with the standard model of the lanthanides. P. Strange et al [36] did not provide values for the bulk modulus. The main advantage of SIC is that it is a parameter free, entirely self-contained method. It reproduces the equilibrium volume very well and also the total energy difference between the divalent and trivalent state is found in very good agreement with experiment [36]. However, spectroscopies are not available directly, as SIC generally pushes correlated states too far below the Fermi level. Moreover it does not capture the multiplet effect since it is a single determinant, static mean field solution. The hybridization of the f states is generally overestimated, wherefore it is not completely compatible with the standard model of the lanthanides. The GGA+U method (Fig. 6.1(d)) seems to reproduce the trend in the volume of the late REs very

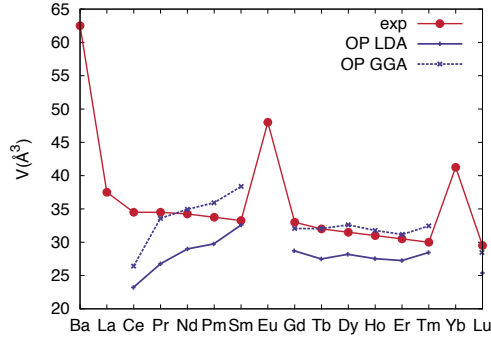
well. Judging on only the Sm volume, GGA+U probably does not capture the trend in the volume across the light RE series. The GGA+U bulk modulus (Fig. 6.2(c)) has the correct order of magnitude for the late RE. However, also this method is not able to correctly reproduce the spectral features as can be seen in the appendix of Paper I. Since GGA+U is essentially a single particle method, this method might give the correct electron density, but is not able to capture the many-body transitions that constitute the spectra.



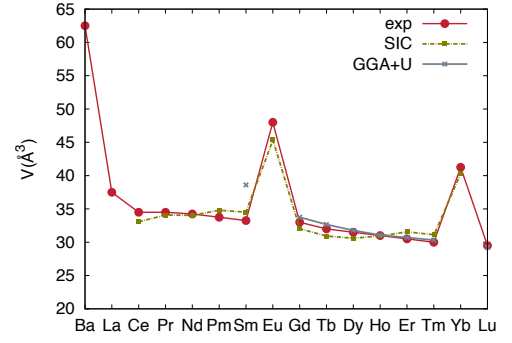
(a) Yellow: A. Delin [9] and purple: P. Söderlind [35]



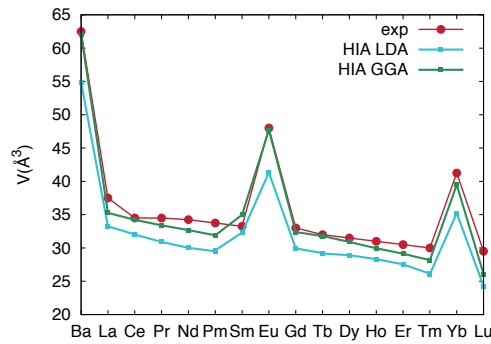
(b) P. Söderlind [35]



(c) P. Söderlind [35]

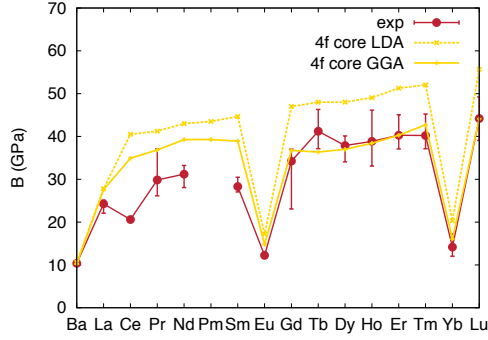


(d) Olive green: SIC P. Strange [36] and grey: GGA+U S.K. Mohanta [32]

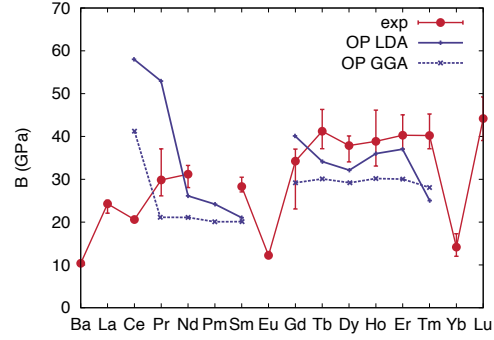


(e) Present results

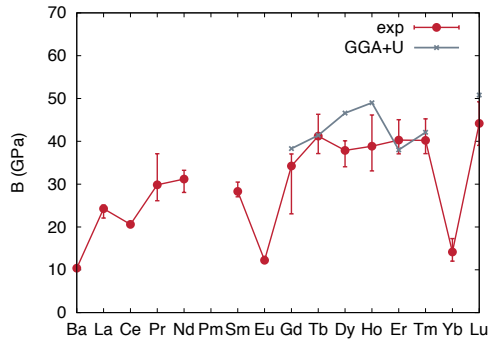
Figure 6.1: Equilibrium volume per atom: The red solid dots are experimental data from Ref. [15] for the volumes and from Ref. [14] for the bulk moduli. All other dots are calculations with various methods, as explained in the legend and captions to the different figures. The different methods are described in the main text.



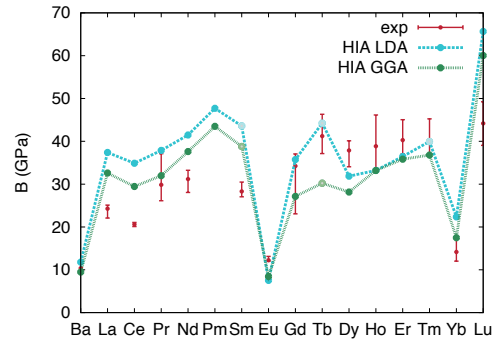
(a) A. Delin [9]



(b) P. Söderlind [35]



(c) S.K. Mohanta [32]



(d) Present results

Figure 6.2: Bulk modulus: The red solid dots are experimental data from Ref. [15]. All other dots are calculations with various methods explained in the legend and captions to the different figures. The different methods are described in the main text. The slightly lighter dots in the HIA calculation belong to points that are currently not yet completely converged with respect to the number of k points.

6.2 Magnetic Moments

In Paper I, the saturation moments are presented and they are here repeated in Fig. 6.3(a). The theoretical values belong to the $4f$ moment in a field that is high enough and for a temperature that is low enough to select only the lowest multiplet. Under the influence of a field, the degenerate J multiplet splits into $|J, J_z\rangle$ states, which are separated by an energy proportional to the strength of the magnetic field. The temperature in the simulations is chosen such that $k_B T$ is smaller than this separation and therefore only the lowest multiplet is selected. In Fig. 6.3(c) and 6.3(d) the contribution of the f spin moment and f orbital moment are presented separately. Results from P. Söderlind et al. [35] for the trivalent RE's, obtained with a $4f$ band model including spin-polarization, spin-orbit coupling and orbital polarization, and from S.K. Mohanta et al. [32] for the heavy RE's, obtained with GGA+U, are added for comparison. The $4f$ band model used by P. Söderlind et al. [35] shows the strongest discrepancy with the moments expected from Hund's rules and those obtained by the HIA. The HIA clearly overestimates the saturated moments for the early RE's and underestimates them for the late REs. For the light REs, in particular for Ce, the largest error comes from neglecting a still finite hybridization. Across the entire series, instead, an other error is due to the contribution of the $[spd]$ electrons to the total moment, since the experiments are carried out at moderately high fields, which polarizes the valence electrons. Therefore an estimation of the $[spd]$ moment is plotted in Fig. 6.3(b). We subtract the experimental moment from our HIA results for the f moment. We added the $[spd]$ contribution to the total moment calculated with the $4f$ in the core model.

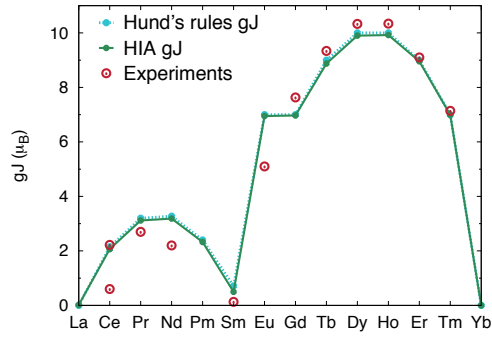
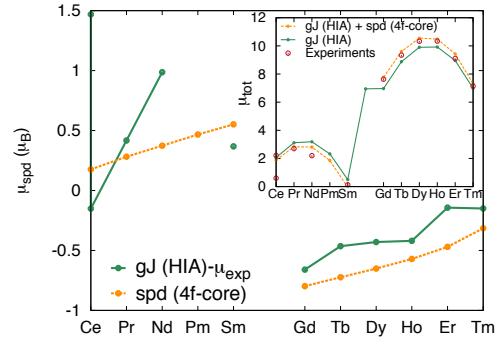
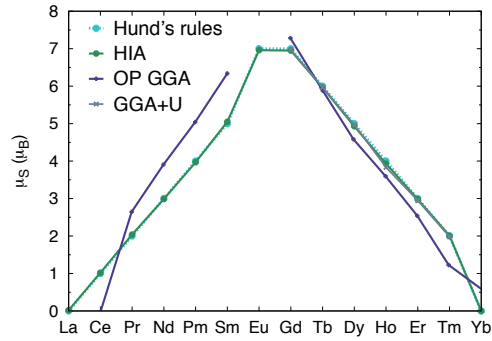
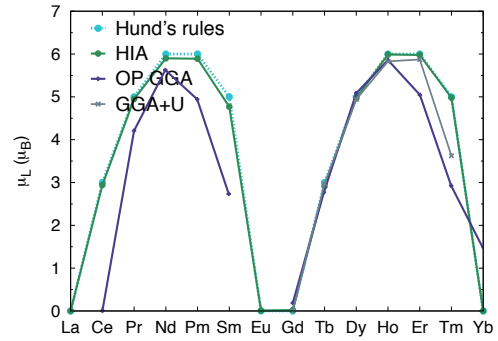
(a) Saturated f moment(b) spd moment(c) f spin moment(d) f orbital moment

Figure 6.3: Magnetic moments: Different methods are compared, including the Hund's rules, the present method (HIA), the $4f$ band including orbital polarization (OP) by P. Söderlind [35] and the GGA+U by S.K. Mohanta [32]. The red dots are experimentally measured saturated moments taken from Ref. [23] (Table 1.6). The highest experimental value for Ce is taken from Ref. [11].

6.3 Spectra

In Paper I, the photoemission and inverse photoemission spectra of all REs have been reported. In this section we discuss only a few REs in order to compare the spectra for different double counting schemes and different exchange correlation functionals. Moreover we will compare our results to the results obtained by S. Lebègue et al. [28, 27], who used the atomic sphere approximation (ASA).

In Fig. 6.4 in the first and second row, we compare two double counting schemes. The first double counting scheme is the fixed peak (FP) double counting, where the double counting energy is chosen such that the first occupied (or unoccupied) peak is fixed to its experimental value. The second double counting scheme is the fully localized limit (FLL), which is explained in Sec. 3.2.5. Changing from FP to FLL results mainly in a rigid shift (towards lower energies) of the f spectrum compared to the $[spd]$ spectrum.

In Fig. 6.4 in the second and third row, we compare the LDA and GGA exchange correlation functionals for the FLL double counting. Tiny differences can be observed, such as the fact that GGA seems to shift the peaks to slightly higher energies, which results in a slightly better agreement with experiment.

In Fig. 6.5 we compare our FP-LMTO method to the LMTO-ASA method used by S. Lebègue et al. [28, 27], also employing the HIA. There seem to be three main differences between the present calculations and the calculations done by S. Lebègue et al. We used a FP-LMTO code, whereas S. Lebègue et al. performed the calculations within the atomic sphere approximation. Moreover S. Lebègue et al neglected all crystal field effects. And last, S. Lebègue et al. write in Ref. [28] that they use a temperature close to zero in order to populate only the lowest multiplet. We, however, use a bigger temperature, which might give rise to a bit different initial occupations of the multiplets.

The most striking differences were found in the BIS spectra of Pr, Nd and Sm, as well as in the XPS spectra of Tb and Dy. In Fig. 6.5 we therefore present the BIS spectra for Pr and Nd and the XPS spectra for Tb and Dy. We compare the experimental spectra to the spectra calculated with LMTO-ASA [28, 27] and with FP-LMTO (present study). In the present study, as well as in the study of S. Lebègue et al. [28, 27], $U = 7$ eV was used. The calculated J 's are similar up to tens of meV. Two main differences are found between the FP and ASA results. Firstly the relative heights of the peaks differ, which is displayed in the plots. The FP-LMTO methods finds better agreement with experiment regarding the relative heights of the peaks. The second difference can be found in Paper I and regards the little hump in the XPS spectrum between -1.5 and 0 eV. For the light elements this hump was not captured by the LMTO-ASA method [28], whereas the FP method captures it quite well. It appears to be mainly due to the $[spd]$ contribution to the spectral function. Note that in Fig. 6.5 all FP-LMTO results and the LMTO-ASA results for the *light* RE are total spectral functions, whereas the LMTO-ASA results for the *heavy* RE contain only the f contribution to the spectral function, since these results are the only once reported in Ref. [27]. One can therefore not see whether the LMTO-ASA method captures the hump for the heavy REs or not.

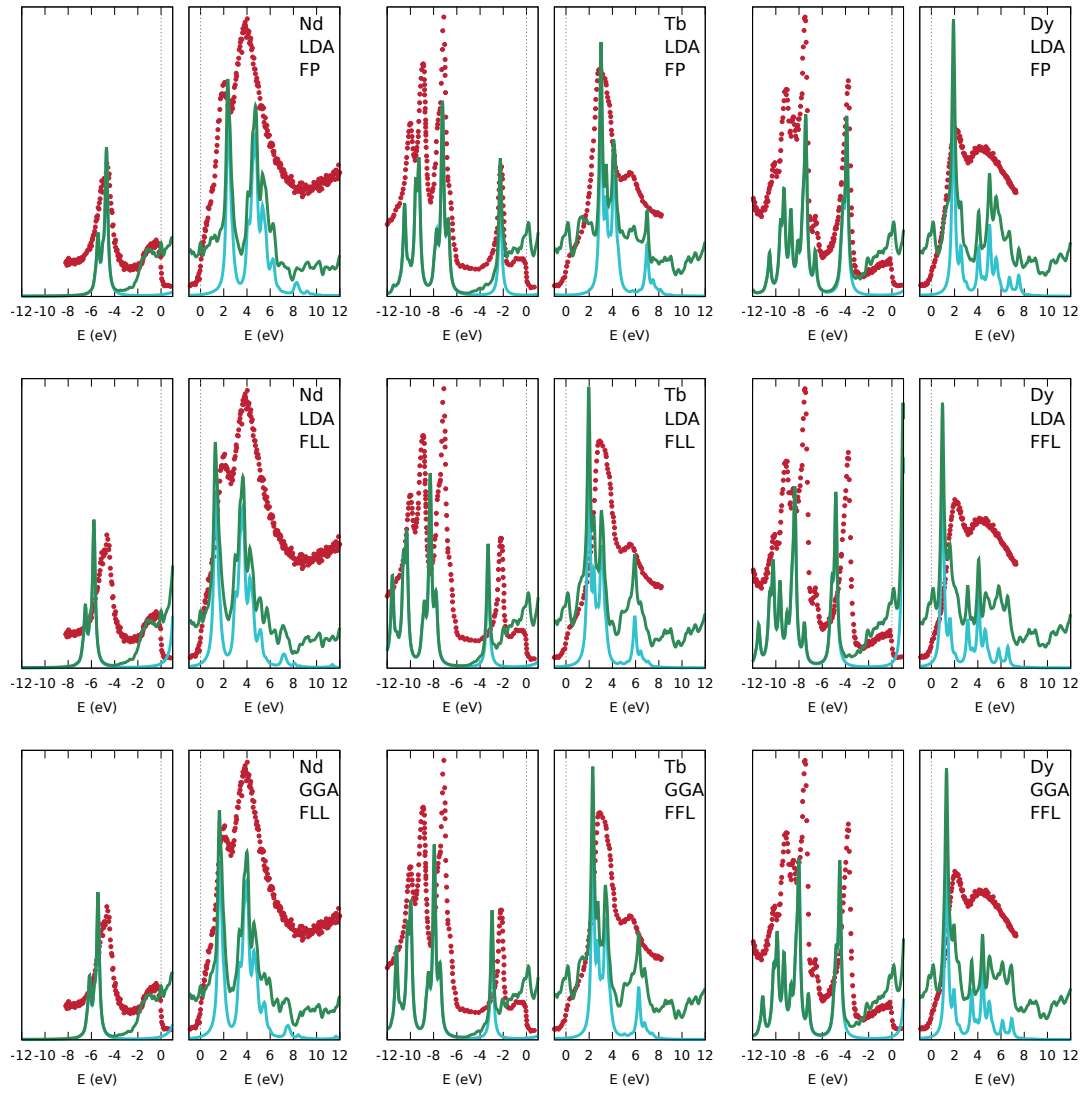


Figure 6.4: Spectra for Nd, Tb and Dy: The first and second row show the difference between the fixed peak (FP) double counting and the fully localized limit (FLL) double counting. The second and third row show the difference between LDA and GGA functionals. The red dots are experimental data from Ref. [26].

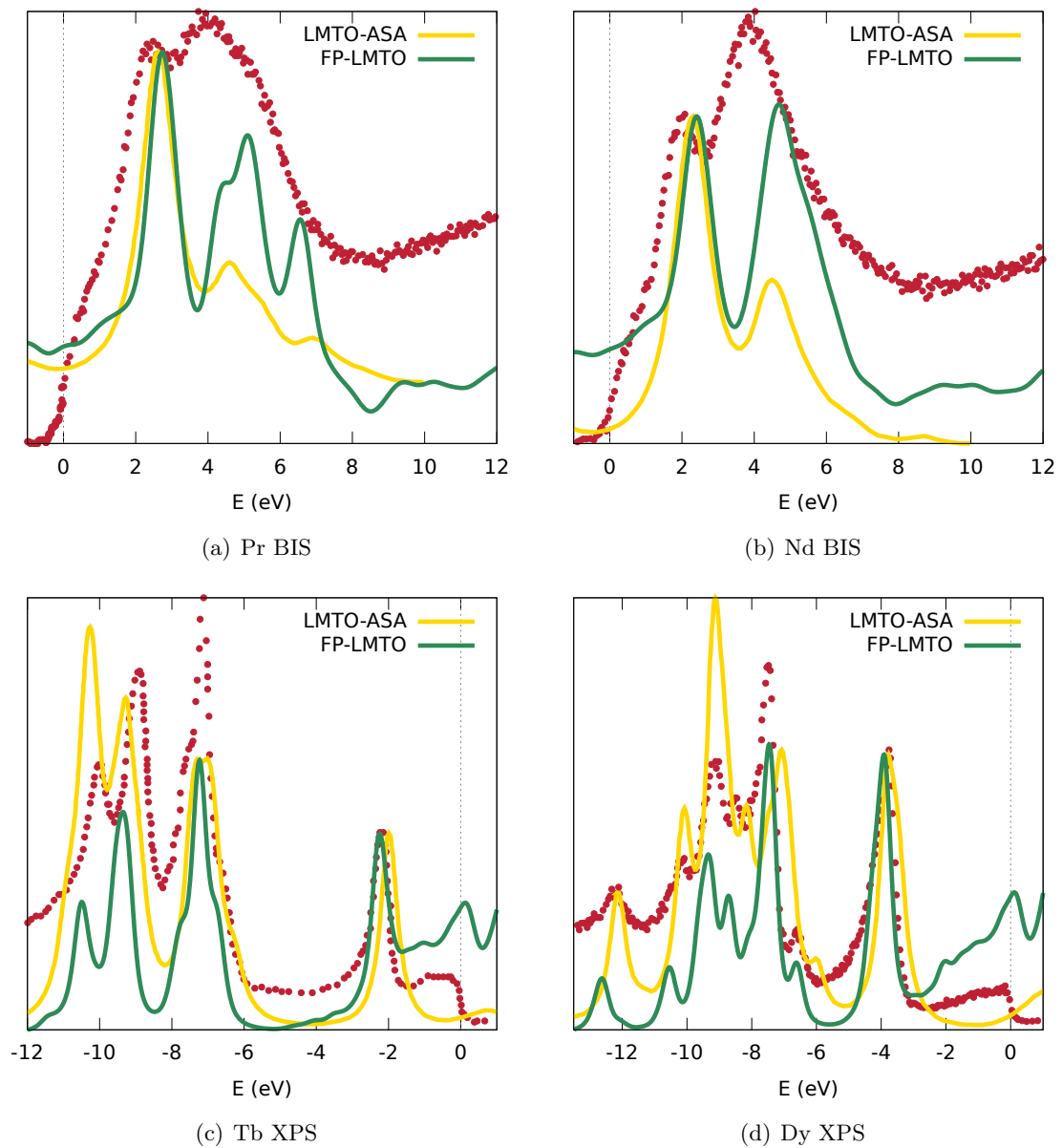


Figure 6.5: BIS spectra for Pr, Nd and XPS spectra for Tb and Dy: Comparison between spectra calculated with FP-LMTO (present study) and LMTO-ASA (S. Lebègue et al. [28, 27]). The FP-LMTO spectra are smeared compared to the spectra displayed in Fig. 6.4 for easy comparison. The red dots are experimental data from Ref. [26].

Chapter 7

Outlook

In this licentiate thesis and in Paper I we show that the FP-LMTO LDA+HIA method reproduces the cohesive properties like equilibrium volume and bulk modulus for the REs. We also find an excellent agreement between theory and experiment for the photoemission and inverse photoemission spectra of the valence band, and we reproduce the spin and orbital moments of these elements. However there are still some open questions and unsolved problems. One of these is the inclusion of crystal field effects. For some of the REs these effects are very important. A good description of the crystal field would be helpful for investigating the magnetic moment, critical temperature and magnetic anisotropy energy of permanent magnets including REs. An other interesting topic to investigate is the contribution of the *[spd]* polarization to the total moment. For this it would be nice to describe the *[spd]* electrons charge self-consistently in spin-polarized simulations. However this is a bit complicated, since it is not so straightforward which double counting scheme to use in the spin polarized case. A small technical improvement that could be done is the evaluation of $\text{Tr}[\hat{\Sigma}_{at}\hat{G}_{at}]$ instead of $\text{Tr}[\hat{\Sigma}_{at}\hat{G}]$ in the Galitskii-Migdal energy. This improves the adequateness of the FLL with atomic occupations double counting scheme, as was explained in Sec. 3.2.5. To really make sure that the HIA is the best way to calculate the lanthanides, it is needed to know if HIA predicts the correct crystal structures. We did some preliminary tests on Nd, which seem to give the correct structures. However, further investigations, including the other REs and under variable pressures, still have to be done.

Appendix A

Finding the multiplets in Nd

In this appendix the multiplets in the $f^3 \rightarrow f^2$ transition in Nd are constructed. This is a sort of recipe how to construct the multiplets, which I have probably learned in my undergraduate studies. Unfortunately I have also forgotten it... For me learning it again was an eye opener and made a lot of things clearer. Therefore I wrote the example of Nd down.

To construct the many body multiplets after the $f^3 \rightarrow f^2$ transition in Nd, one has to write down all the ways in which one can divide two electrons over 7 orbitals or 14 spin orbitals. This can be done in $\frac{14*13}{2} = 91$ ways. In Tab. A.1 I listed all of them in a compact way. I listed them in 5 groups. The first group is special, it contains a spin pair in one orbital, which can be $m_l = -3, -2, -1, 0, 1, 2, 3$. The second group considers two spin up in different orbitals. The first spin up can be in $m_l = -3, -2, -1, 0, 1, 2, 3$ and the second can be in all possible orbitals with m_l bigger than that of the first. The other three groups have the same form, but with one up and one down, with one down and one up and finally with two spin down electrons.

The next step in the multiplet recipe is to construct a table denoting how many states we have for each S_z and L_z , see Tab. A.2. The final step is to obtain the possible S, L multiplets from this table. We notice that the highest possible $L = 6$, since the highest possible $L_z = 6$, for this L we have only $S_z = 0$ and therefor $S = 0$. We can thus highlight the $S = 0, L = 6$ multiplet as is done in Tab. A.3. In the following table (Tab. A.4) we have subtracted the $S = 0, L = 6$ multiplet and highlighted the next biggest multiplet $S = 1, L = 5$. This procedure we follow until nothing is left, displayed in Tab. A.5 till A.9. This procedure gave us the following multiplets: $^1I_6, ^3H_{4,5,6}, ^1G_4, ^1S_0, ^3F_{2,3,4}, ^1D_2$ and $^3P_{0,1,2}$.

Table A.1: All possible ways to divide two electrons in 7 orbitals denoted with $-3 \leq m_l \leq 3$. The states are grouped, such that the red arrow can be also in the position of the red dots. The total S_z and L_z are given in the subsequent columns. Where all possibilities for L_z are listed, depending on where the red arrow is. In the last column the number of states in this group is given. The total number of states is $21 + 21 + 21 + 21 + 7 = 91$ as expected.

-3	-2	-1	0	1	2	3	S_z	L_z	#
$\uparrow\downarrow$	0	-6,-4, -2,0,2,4,6	7
\uparrow	\uparrow	1	-5, -4,-3,-2,-1,0	21
	\uparrow	\uparrow		-3, -2, -1,0,1	
		\uparrow	\uparrow		-1,0,1,2	
			\uparrow	\uparrow		1,2,3	
				\uparrow	\uparrow	...		3,4	
					\uparrow	\uparrow		5	
Same for \uparrow \downarrow							0	-5,-4,-3,-2,-1,0, -3,-2,-1,0,1,-1,0,1,2, 1,2,3,3,4,5	21
Same for \downarrow \uparrow							0	-5,-4,-3,-2,-1,0, -3,-2,-1,0,1,-1,0,1,2, 1,2,3,3,4,5	21
Same for \downarrow \downarrow							-1	-5,-4,-3,-2,-1,0, -3,-2,-1,0,1,-1,0,1,2, 1,2,3,3,4,5	21

Table A.2: Number of states with all possible S_z and L_z .

$S_z \setminus L_z$	-6	-5	-4	-3	-2	-1	0	1	2	3	4	5	6
-1	0	1	1	2	2	3	3	3	2	2	1	1	0
0	1	2	3	4	5	6	7	6	5	4	3	2	1
1	0	1	1	2	2	3	3	3	2	2	1	1	0

Table A.3: $S = 0$ and $L = 6$ multiplet 1I_6 .

$S_z \setminus L_z$	-6	-5	-4	-3	-2	-1	0	1	2	3	4	5	6
-1	0	1	1	2	2	3	3	3	2	2	1	1	0
0	1	2	3	4	5	6	7	6	5	4	3	2	1
1	0	1	1	2	2	3	3	3	2	2	1	1	0

$S_z \setminus L_z$	-6	-5	-4	-3	-2	-1	0	1	2	3	4	5	6
-1	0	1	1	2	2	3	3	3	2	2	1	1	0
0	0	1	2	3	4	5	6	5	4	3	2	1	0
1	0	1	1	2	2	3	3	3	2	2	1	1	0

$S_z \setminus L_z$	-6	-5	-4	-3	-2	-1	0	1	2	3	4	5	6
-1	0	0	0	1	1	2	2	2	1	1	0	0	0
0	0	0	1	2	3	4	5	4	3	2	1	0	0
1	0	0	0	1	1	2	2	2	1	1	0	0	0

$S_z \setminus L_z$	-6	-5	-4	-3	-2	-1	0	1	2	3	4	5	6
-1	0	0	0	1	1	2	2	2	1	1	0	0	0
0	0	0	0	1	2	3	4	3	2	1	0	0	0
1	0	0	0	1	1	2	2	2	1	1	0	0	0

$S_z \setminus L_z$	-6	-5	-4	-3	-2	-1	0	1	2	3	4	5	6
-1	0	0	0	0	0	1	1	1	0	0	0	0	0
0	0	0	0	0	1	2	3	2	1	0	0	0	0
1	0	0	0	0	0	1	1	1	0	0	0	0	0

$S_z \setminus L_z$	-6	-5	-4	-3	-2	-1	0	1	2	3	4	5	6
-1	0	0	0	0	0	1	1	1	0	0	0	0	0
0	0	0	0	0	0	1	2	1	0	0	0	0	0
1	0	0	0	0	0	1	1	1	0	0	0	0	0

$S_z \setminus L_z$	-6	-5	-4	-3	-2	-1	0	1	2	3	4	5	6
-1	0	0	0	0	0	0	0	0	0	0	0	0	0
0	0	0	0	0	0	0	1	0	0	0	0	0	0
1	0	0	0	0	0	0	0	0	0	0	0	0	0

Appendix B

Direct Coulomb and Coulomb exchange

In this appendix the math is done for obtaining Eq. 3.21 from the third term in Eq. 3.7. Note that we will consider only intra-site and intra-shell interactions, which means we can omit the site index and shell index and the tensor can be expressed as

$$U_{m_1, m_2, m_3, m_4} \quad (\text{B.1})$$

where m is the magnetic quantum number belonging to the orbital quantum number l under consideration. Note moreover that the Coulomb repulsion does not touch the spin, therefore $\delta_{\sigma_1, \sigma_3} \delta_{\sigma_2, \sigma_4}$. For real valued wave functions and in the case that $F^2 \gg F4$, only four terms in the U -tensor are not equal to zero. These components correspond to the cases where $m_1 = m_2 \& m_3 = m_4$, $m_1 = m_3 \& m_2 = m_4$, $m_1 = m_4 \& m_2 = m_3$ and $m_1 = m_2 = m_3 = m_4$. We can rewrite the third term of the Hamiltonian in Eq. 3.7 without the sum over \mathbf{R} , where we separate the above mentioned cases into Eq. B.2a, Eq. B.2b, Eq. B.2c and Eq. B.2d respectively.

$$\begin{aligned} \hat{H}_{Coulomb} = & \frac{1}{2} \sum_{\substack{m_1 \sigma, m_2 \sigma' \\ m_3 \sigma, m_4 \sigma'}} U_{m_1, m_2, m_3, m_4} \hat{c}_{m_1 \sigma}^\dagger \hat{c}_{m_2 \sigma'}^\dagger \hat{c}_{m_4 \sigma'} \hat{c}_{m_3 \sigma} = \\ & \frac{1}{2} \sum_{\substack{m, m' \\ m \neq m'}} \sum_{\sigma, \sigma'} U_{m, m, m', m'} \hat{c}_{m \sigma}^\dagger \hat{c}_{m \sigma'}^\dagger \hat{c}_{m' \sigma'} \hat{c}_{m' \sigma} \end{aligned} \quad (\text{B.2a})$$

$$+ \frac{1}{2} \sum_{\substack{m, m' \\ m \neq m'}} \sum_{\sigma, \sigma'} U_{m, m', m, m'} \hat{c}_{m \sigma}^\dagger \hat{c}_{m' \sigma'}^\dagger \hat{c}_{m' \sigma'} \hat{c}_{m \sigma} \quad (\text{B.2b})$$

$$+ \frac{1}{2} \sum_{\substack{m, m' \\ m \neq m'}} \sum_{\sigma, \sigma'} U_{m, m', m', m} \hat{c}_{m \sigma}^\dagger \hat{c}_{m' \sigma'}^\dagger \hat{c}_{m \sigma'} \hat{c}_{m' \sigma} \quad (\text{B.2c})$$

$$+ \frac{1}{2} \sum_m \sum_{\substack{\sigma, \sigma' \\ \sigma \neq \sigma'}} U_{m, m, m, m} \hat{c}_{m \sigma}^\dagger \hat{c}_{m \sigma'}^\dagger \hat{c}_{m \sigma'} \hat{c}_{m \sigma} \quad (\text{B.2d})$$

We will rewrite this equation term by term, by anti commuting the creation and annihilation operators until we obtain number operators (if possible) or until m' is right from m . We skip the factor $1/2$ and the sum for a while and write only the surviving terms. Term B.2a gives zero if $\sigma = \sigma'$. For $\sigma \neq \sigma'$ we obtain:

$$-U_{m, m, m', m'} \hat{c}_{m \sigma}^\dagger \hat{c}_{m \bar{\sigma}}^\dagger \hat{c}_{m' \sigma} \hat{c}_{m' \bar{\sigma}} \quad (\text{B.3})$$

where we wrote $\bar{\sigma}$ to denote the opposite spin of σ . The next term B.2b contributes for both $\sigma = \sigma'$ and $\sigma \neq \sigma'$, it gives respectively:

$$U_{m,m',m,m'} \hat{n}_{m\sigma} \hat{n}_{m'\sigma} \quad (\text{B.4a})$$

$$U_{m,m',m,m'} \hat{n}_{m\sigma} \hat{n}_{m'\bar{\sigma}} \quad (\text{B.4b})$$

where \hat{n} is the number operator. The third term B.2c contributes as well for both $\sigma = \sigma'$ and $\sigma \neq \sigma'$:

$$-U_{m,m',m',m} \hat{n}_{m\sigma} \hat{n}_{m'\sigma} \quad (\text{B.5a})$$

$$-U_{m,m',m',m} \hat{c}_{m\sigma}^\dagger \hat{c}_{m\bar{\sigma}} \hat{c}_{m'\bar{\sigma}}^\dagger \hat{c}_{m'\sigma} \quad (\text{B.5b})$$

Finally the last term B.2d contributes only for $\sigma \neq \sigma'$ as can already be seen in the sum:

$$U_{m,m,m,m} \hat{n}_{m\sigma} \hat{n}_{m\bar{\sigma}} \quad (\text{B.6})$$

Now we will regroup them:

$$\hat{H}_{Coulomb} = \frac{1}{2} \sum_{m,m',\sigma} U_{m,m',m,m'} \hat{n}_{m\sigma} \hat{n}_{m'\bar{\sigma}} \quad (\text{B.7a})$$

$$+ \frac{1}{2} \sum_{\substack{m,m',\sigma \\ m \neq m'}} (U_{m,m',m,m'} - U_{m,m',m',m}) \hat{n}_{m\sigma} \hat{n}_{m'\sigma} \quad (\text{B.7b})$$

$$- \frac{1}{2} \sum_{\substack{m,m',\sigma \\ m \neq m'}} U_{m,m,m',m'} \hat{c}_{m\sigma}^\dagger \hat{c}_{m\bar{\sigma}} \hat{c}_{m'\sigma} \hat{c}_{m'\bar{\sigma}} \quad (\text{B.7c})$$

$$- \frac{1}{2} \sum_{\substack{m,m',\sigma \\ m \neq m'}} U_{m,m',m',m} \hat{c}_{m\sigma}^\dagger \hat{c}_{m\bar{\sigma}} \hat{c}_{m'\bar{\sigma}}^\dagger \hat{c}_{m'\sigma} \quad (\text{B.7d})$$

This regrouping was done as follows: B.4b + B.6 \rightarrow B.7a, B.4a + B.5a \rightarrow B.7b, B.3 \rightarrow B.7c and B.5b \rightarrow B.7d. This can now be written as

$$\hat{H}_{Coulomb} = \frac{1}{2} \sum_{m,m',\sigma} U_{mm'} \hat{n}_{m\sigma} \hat{n}_{m'\bar{\sigma}} \quad (\text{B.8a})$$

$$+ \frac{1}{2} \sum_{\substack{m,m',\sigma \\ m \neq m'}} (U_{mm'} - J_{mm'}) \hat{n}_{m\sigma} \hat{n}_{m'\sigma} \quad (\text{B.8b})$$

$$- \frac{1}{2} \sum_{\substack{m,m',\sigma \\ m \neq m'}} J_{mm'} \left(\hat{c}_{m\sigma}^\dagger \hat{c}_{m\bar{\sigma}} \hat{c}_{m'\sigma} \hat{c}_{m'\bar{\sigma}} + \hat{c}_{m\sigma}^\dagger \hat{c}_{m\bar{\sigma}} \hat{c}_{m'\bar{\sigma}}^\dagger \hat{c}_{m'\sigma} \right) \quad (\text{B.8c})$$

Where the different parts of the U -tensor are replaced by $U_{mm'}$ for the direct Coulomb repulsion and $J_{mm'}$ for the Coulomb exchange

$$U_{mm'} = U_{mm'mm'} \quad (\text{B.9})$$

$$J_{mm'} = U_{mm'm'm} \quad (\text{B.10})$$

Appendix C

Basis notation look-up

In this appendix I briefly list the explanation of all symbols in the basis notation and the different tail energy sets. As an example we will take the following basis:

$$3^{\alpha:1,2,3}(6s^{20}6p^{21})2^{\alpha:1,2}(5d^04f^{-1}) \quad 2^{\alpha:1,2}(5s^{-1}5p^{-1})0(5d^04f^{-1})$$

The **red numbers** denote the number of tails attached to the basis functions in the parentheses to the right of the red number. These basis functions are described by their atomic parentage. Zero tails indicate that the following nl are not explicitly included in the basis.

The **blue Greek letter** indicates the tail energy set used. This tail energy sets are described in the text and listed below:

α	:	$\kappa^2 = \{0.3, -2.3, -1.5\}$ Ry
β	:	$\kappa^2 = \{0.25, -2.3, -1.0, -0.2\}$ Ry
γ	:	$\kappa^2 = \{0.3, -2.3, -0.6\}$ Ry
δ	:	$\kappa^2 = \{-0.1, -0.5, -1.2, -2.3\}$ Ry
ϵ	:	$\kappa^2 = \{-0.1, -0.96, -1.82, -2.68\}$ Ry
ζ	:	$\kappa^2 = \{-0.1, -0.5, -1.2, -2.3, 0.1\}$ Ry, where the energy of the last tail (0.1 Ry) was varied such that the tail energy κ^2 was set to the value of the average kinetic energy in the interstitial.

The **green list of numbers** denote which of the tails in the tail energy set are used.

The **violet quantum numbers nl** denote the atomic parentage of the basis functions inside the muffin tin sphere.

The orange **superscript numbers** encode the linearization energy. Values commonly used in this report are

20	=	linearization energy of the s -function is chosen such that the function is orthonormalized to the function of s with the lowest principal quantum number that is included
21	=	linearization energy of the p -function is chosen such that the function is orthonormalized to the function of p with the lowest principal quantum number that is included
0	=	internal algorithm is used to determine the linearization energy
-1	=	linearization energy is set to the center of the band

Bibliography

- [1] P. Anthony Cox. Fractional parentage methods for ionisation of open shells of d and f electrons. In *Photoelectron Spectrometry*, volume 24 of *Structure and Bonding*, pages 59–81. Springer Berlin Heidelberg, 1975.
- [2] Neil W. Ashcroft and N. David Mermin. *Solid state physics*. Saunders College, Philadelphia, 1976.
- [3] Francis Birch. Finite elastic strain of cubic crystals. *Phys. Rev.*, 71:809–824, Jun 1947.
- [4] Torbjörn Björkman. *Magnetic and Structural Properties of f-electron Systems from First Principles Theory*. PhD thesis, Uppsala University, 2009.
- [5] Felix Bloch. Über die quantenmechanik der elektronen in kristallgittern. *Zeitschrift fr Physik*, 52(7-8):555–600, 1929.
- [6] M. Born and R. Oppenheimer. Zur quantentheorie der molekeln. *Ann. Phys.*, 389(20):457–484, 1927.
- [7] P A Cox, J K Lang, and Y Baer. Study of the 4f and valence band density of states in rare-earth metals. I. theory of the 4f states. *Journal of Physics F: Metal Physics*, 11(1):113, 1981.
- [8] P. H. Dederichs, S. Blügel, R. Zeller, and H. Akai. Ground states of constrained systems: Application to cerium impurities. *Phys. Rev. Lett.*, 53:2512–2515, Dec 1984.
- [9] Anna Delin, Lars Fast, Börje Johansson, Olle Eriksson, and J. M. Wills. Cohesive properties of the lanthanides: Effect of generalized gradient corrections and crystal structure. *Phys. Rev. B*, 58:4345–4351, Aug 1998.
- [10] Igor Di Marco. *Correlation Effects in the Electronic Structure of Transition Metals and Their Compounds*. PhD thesis, Radboud University Nijmegen, Ipskamp Drukkers, Enschede, The Netherlands, 2009.
- [11] F Drymiotis, J Singleton, N Harrison, J C Lashley, A Bangura, C H Mielke, L Balicas, Z Fisk, A Migliori, and J L Smith. Suppression of the structural phase transition in ce 0.8 la 0.1 th 0.1 by large magnetic fields. *Journal of Physics: Condensed Matter*, 17(7):L77, 2005.
- [12] Raymond Frésard and Gabriel Kotliar. Interplay of mott transition and ferromagnetism in the orbitally degenerate hubbard model. *Phys. Rev. B*, 56:12909–12915, Nov 1997.

- [13] Antoine Georges. Strongly correlated electron materials: Dynamical mean-field theory and electronic structure. *AIP Conference Proceedings*, 715(1):3–74, 2004.
- [14] W. A. Grosshans and W. B. Holzapfel. Atomic volumes of rare-earth metals under pressures to 40 GPa and above. *Phys. Rev. B*, 45:5171–5178, Mar 1992.
- [15] K.A. Gschneidner. Physical properties of the rare earth metals. *Bulletin of Alloy Phase Diagrams*, 11(3):216–224, 1990.
- [16] Karl A. jr. Gschneidner and LeRoy Eyring. *Handbook on the physics and chemistry of rare earths. Vol. 10, High energy spectroscopy*. Amsterdam, 1987.
- [17] O. Gunnarsson, J. W. Allen, O. Jepsen, T. Fujiwara, O. K. Andersen, C. G. Olsen, M. B. Maple, J.-S. Kang, L. Z. Liu, J.-H. Park, R. O. Anderson, W. P. Ellis, R. Liu, J. T. Markert, Y. Dalichaouch, Z.-X. Shen, P. A. P. Lindberg, B. O. Wells, D. S. Dessau, A. Borg, I. Lindau, and W. E. Spicer. Polarized resonance photoemission for Nd₂CuO₄. *Phys. Rev. B*, 41:4811–4814, Mar 1990.
- [18] O. Gunnarsson, O. K. Andersen, O. Jepsen, and J. Zaanen. Density-functional calculation of the parameters in the anderson model: Application to Mn in CdTe. *Phys. Rev. B*, 39:1708–1722, Jan 1989.
- [19] P. Hohenberg and W. Kohn. Inhomogeneous electron gas. *Phys. Rev.*, 136:B864–B871, Nov 1964.
- [20] J. Hubbard. Electron correlations in narrow energy bands. *Proceedings of the Royal Society of London A: Mathematical, Physical and Engineering Sciences*, 276(1365):238–257, 1963.
- [21] J. Hubbard. Electron correlations in narrow energy bands. II. the degenerate band case. *Proceedings of the Royal Society of London A: Mathematical, Physical and Engineering Sciences*, 277(1369):237–259, 1964.
- [22] J. Hubbard. Electron correlations in narrow energy bands. III. an improved solution. *Proceedings of the Royal Society of London A: Mathematical, Physical and Engineering Sciences*, 281(1386):401–419, 1964.
- [23] Jens Jensen and Allan R. Mackintosh. *Rare earth magnetism*. Clarendon Press, Oxford, 1991.
- [24] Neil Erich Koch. Crystal structures and electrical resistivities of new YRu₄Sn₆-type rare-earth based compounds. Master’s thesis, University of Johannesburg, South Africa, 2008.
- [25] W. Kohn and L. J. Sham. Self-consistent equations including exchange and correlation effects. *Phys. Rev.*, 140:A1133–A1138, Nov 1965.
- [26] J. K. Lang, Y. Baer, and P. A. Cox. Study of the 4f and valence band density of states in rare-earth metals. II. experiment and results. *Journal of Physics F: Metal Physics*, 11(1):121, 1981.

- [27] S. Lebègue, A. Svane, M. I. Katsnelson, A. I. Lichtenstein, and O. Eriksson. Multiplet effects in the electronic structure of heavy rare-earth metals. *Journal of Physics: Condensed Matter*, 18(27):6329, 2006.
- [28] S. Lebègue, A. Svane, M. I. Katsnelson, A. I. Lichtenstein, and O. Eriksson. Multiplet effects in the electronic structure of light rare-earth metals. *Phys. Rev. B*, 74:045114, Jul 2006.
- [29] Richard M. Martin. *Electronic structure : basic theory and practical methods*. Cambridge University Press, Cambridge, New York, 2004.
- [30] A. K. McMahan, Richard M. Martin, and S. Satpathy. Calculated effective hamiltonian for La_2CuO_4 and solution in the impurity anderson approximation. *Phys. Rev. B*, 38:6650–6666, Oct 1988.
- [31] Walter Metzner and Dieter Vollhardt. Correlated lattice fermions in $d = \infty$ dimensions. *Phys. Rev. Lett.*, 62:324–327, Jan 1989.
- [32] S.K. Mohanta, S.N. Mishra, S.K. Srivastava, and M. Rots. First-principles calculation of the electric field gradient and magnetic hyperfine field in rare-earth metals (Gd to Lu) and dilute alloys with Cd. *Solid State Communications*, 150(37-38):1789 – 1793, 2010.
- [33] M. R. Norman and A. J. Freeman. Model supercell local-density calculations of the $3d$ excitation spectra in NiO. *Phys. Rev. B*, 33:8896–8898, Jun 1986.
- [34] L. V. Pourovskii, B. Amadon, S. Biermann, and A. Georges. Self-consistency over the charge density in dynamical mean-field theory: A linear muffin-tin implementation and some physical implications. *Phys. Rev. B*, 76:235101, Dec 2007.
- [35] Per Söderlind, P. E. A. Turchi, A. Landa, and V. Lordi. Ground-state properties of rare-earth metals: an evaluation of density-functional theory. *Journal of Physics: Condensed Matter*, 26(41):416001, 2014.
- [36] P. Strange, A. Svane, W. M. Temmerman, Z. Szotek, and H. Winter. Understanding the valency of rare earths from first-principles theory. *Nature*, 399:756–758, 1999.
- [37] J.M. Wills, O. Eriksson, M. Alouani, and D.L. Price. Full-potential LMTO total energy and force calculations. In Hugues Dreyss, editor, *Electronic Structure and Physical Properties of Solids*, volume 535 of *Lecture Notes in Physics*, pages 148–167. Springer Berlin Heidelberg, 2000.
- [38] John M. Wills, Mebarek Alouani, Per Andersson, Anna Delin, Olle Eriksson, and Oleksiy Grechnev. The full-potential electronic structure problem and RSPt. In *Full-Potential Electronic Structure Method*, volume 167 of *Springer Series in Solid-State Sciences*, pages 47–73. Springer Berlin Heidelberg, 2010.

